

LEVEL III

AD-
(2)

AFATL-TR-80-107

AD A103964

Prediction of Forces and Moments on Finned Missiles at High Angle of Attack in Transonic Flow

W L Oberkampf

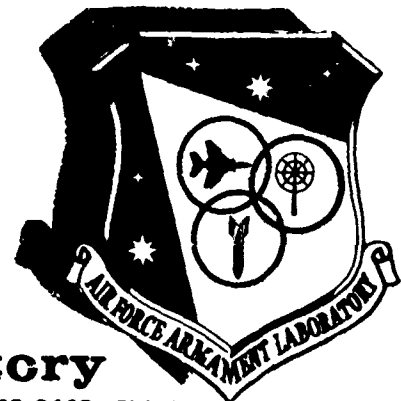
UNIVERSITY OF TEXAS AT AUSTIN
DEPARTMENT OF MECHANICAL ENGINEERING
AUSTIN, TEXAS 78712

OCTOBER 1980

FINAL REPORT FOR PERIOD OCTOBER 1978 - SEPTEMBER 1979

DTIC
ELECTE
AUG 27 1981
A

Approved for public release; distribution unlimited



Air Force Armament Laboratory

AIR FORCE SYSTEMS COMMAND • UNITED STATES AIR FORCE • EGLIN AIR FORCE BASE, FLORIDA

81 8 27 001

DTIC FILE COPY

NOTICE

**Please do not request copies of this report from the Air Force Armament Laboratory.
Additional copies may be obtained from:**

**Defense Technical Information Center
Cameron Station
Alexandria, Virginia 22314**

UNCLASSIFIED

SECURITY CLASSIFICATION OF THIS PAGE (When Data Entered)

REPORT DOCUMENTATION PAGE		READ INSTRUCTIONS BEFORE COMPLETING FORM
1. REPORT NUMBER AFATL-TR-80-107	2. GOVT ACCESSION NO. AD-A103 964	3. RECIPIENT'S CATALOG NUMBER
4. TITLE (and Subtitle) PREDICTION OF FORCES AND MOMENTS ON FINNED MISSILES AT HIGH ANGLE OF ATTACK IN TRANSONIC FLOW		5. TYPE OF REPORT & PERIOD COVERED Final Report October 1978 - September 1979
7. AUTHOR(s) W. L. Oberkampf		6. PERFORMING ORG. REPORT NUMBER
9. PERFORMING ORGANIZATION NAME AND ADDRESS University of Texas at Austin Dept. of Mechanical Engineering Austin, TX 78712		8. CONTRACT OR GRANT NUMBER(s) F08635-77-C-0049
11. CONTROLLING OFFICE NAME AND ADDRESS Air Force Armament Laboratory Armament Division Eglin AFB, Florida 32542		10. PROGRAM ELEMENT, PROJECT, TASK AREA & WORK UNIT NUMBERS Program Element 61102F JON 2307E103
14. MONITORING AGENCY NAME & ADDRESS (if different from Controlling Office)		12. REPORT DATE October 1980
		13. NUMBER OF PAGES 144
		15. SECURITY CLASS. (of this report) Unclassified
		15a. DECLASSIFICATION/DOWNGRADING SCHEDULE
16. DISTRIBUTION STATEMENT (of this Report) Approved for public release; distribution unlimited		
17. DISTRIBUTION STATEMENT (of the abstract entered in Block 20, if different from Report)		
18. SUPPLEMENTARY NOTES Available in DTIC		
19. KEY WORDS (Continue on reverse side if necessary and identify by block number) Missile Aerodynamics Unguided Missiles Guided Missiles Subsonic Missiles Aerodynamic Characteristics of Missiles Transonic Missiles Aerodynamic Interference on Missiles		
20. ABSTRACT (Continue on reverse side if necessary and identify by block number) This report describes a theoretical investigation for the prediction of fin forces and moments on missiles at high angle of attack in subsonic and transonic flow. The body is assumed to be a circular cylinder with cruciform fins (or wings) as attached lifting surfaces. The theory considers a lifting surface of arbitrary planform; the leading edge can have arbitrary sweep back and the trailing edge can be swept back or forward. The missile can have an arbitrary roll (or bank) angle and each fin can have individual control deflection. The angle of attack of the missile is assumed to be such that the body vortex		

DD FORM 1 JAN 73 1473

EDITION OF 1 NOV 65 IS OBSOLETE

UNCLASSIFIED

SECURITY CLASSIFICATION OF THIS PAGE (When Data Entered)

UNCLASSIFIED

SECURITY CLASSIFICATION OF THIS PAGE(When Data Entered)

wake is symmetric. Extensive comparisons are made between predicted results and experimental measurements. Included in the comparisons are: panel normal force, root bending moment, induced roll moment, nonlinear roll damping moment, pitch (or yaw) control forces, and roll control moment. A computer program was written to implement the present method.

Accession For	
NTIS GRA&I	<input checked="checked" type="checkbox"/>
DTIC TAB	<input type="checkbox"/>
Unannounced	<input type="checkbox"/>
Justification	
By	
Distribution/	
Availability Codes	
Dist	Avail and/or Special
A	

UNCLASSIFIED

SECURITY CLASSIFICATION OF THIS PAGE(When Data Entered)

PREFACE

The majority of this work was conducted by the University of Texas at Austin, Austin, Texas, and was sponsored by the Air Force Armament Laboratory (AFATL/DLJ) under Air Force Contract No. F08635-77-C-0049. The work was completed by the author while a Member of the Technical Staff, Sandia National Laboratories, Albuquerque, New Mexico. The contract monitor for AFATL was Dr. Donald C. Daniel (DLJ). The manuscript was submitted for publication on September 24, 1980.

The author would like to thank Dr. Donald C. Daniel, Aerodynamics Research Manager, of the Air Force Armament Laboratory for his comments and suggestions during the investigation. The author also thanks Mr. Randall C. Maydew, Aerodynamics Department Manager, and Mr. Harold R. Vaughn, Aeroballistics Division Supervisor, of Sandia National Laboratories, Albuquerque, New Mexico. Without their generous support, this work would not have been completed.

This report has been reviewed by the Public Affairs Office and is releasable to the National Technical Information Service, (NTIS). At NTIS, it will be available to the general public, including foreign nations.

This technical report has been reviewed and is approved for publication.

FOR THE COMMANDER



BARNES E. HOLDER, JR., Colonel, USAF
Chief, Munitions Division

TABLE OF CONTENTS

Section	Title	Page
I	INTRODUCTION	1
II	AERODYNAMIC ANALYSIS	4
	Body Flow Field	5
	Lifting Theory	11
	Roll Moment	34
	Normal Force and Pitch Moment	37
	Side Force and Yaw Moment	39
	Panel Loads	39
III	RESULTS AND DISCUSSION	42
	Panel Loads	43
	Roll Moments	49
	Control Deflections	55
IV	SUMMARY, CONCLUSIONS AND RECOMMENDATIONS	60
REFERENCES	63

LIST OF FIGURES

Figure	Title	Page
1	Coordinate System and Schematic of Body Vortices	68
2	Cross-Flow Plane Flow Model	69
3	General Planform Fin	70
4	Fin Oriented Coordinates ξ, η	71
5	Normal Force Distribution Over Fin Surface for $\Lambda_{le} = \Lambda_{te} = 60^\circ$	72
6	Normal Force Distribution Over Fin Surface for $\Lambda_{le} = 60^\circ$ and $\Lambda_{te} = 20^\circ$	74
7	Normal Force Distribution Over Fin Surface for $\Lambda_{le} = \Lambda_{te} = 0^\circ$	76
8	Normal Force Distribution Over Fin Surface for $\Lambda_{le} = 60^\circ$ and $\Lambda_{te} = 0^\circ$	78
9	Normal Force Distribution Over Fin Surface for $\Lambda_{le} = 40^\circ$ and $\Lambda_{te} = -40^\circ$	80
10	Surface Normal Vector and Sign Convention for Fin Control Deflection	82
11	Fin Surface Cylindrical Coordinates	83
12	Geometry For Determining Effective Aspect Ratio	84
13	Normal Force Coefficient vs α for Rectangular Planform ($A_e = 1$)	85
14	Normal Force Coefficient vs α for Diamond Planform ($A_e = 1$)	86
15	Normal Force Coefficient vs α for Clipped Delta Planform ($A_e = 1.23$)	87
16	Normal Force Coefficient vs α for Delta Planform ($A_e = 1.46$)	88

LIST OF FIGURES (continued)

Figure	Title	Page
17	Normal Force Coefficient vs α for Rectangular Planform ($A_e = 2$)	89
18	Normal Force Coefficient vs α for Arrow Planform ($A_e = 2$)	90
19	Normal Force Coefficient vs α for Delta Planform ($A_e = 2.31$)	91
20	Normal Force Coefficient vs α for Clipped Arrow Planform ($A_e = 2.61$)	92
21	Normal Force Coefficient vs α for Trapezoidal Planform ($A_e = 3.$)	93
22	Normal Force Coefficient vs α for Delta Planform ($A_e = 4.$)	94
23	Control Interference for Pitch and Roll Control (from Ref. 24)	95
24	Control Interference for Individual Panel Deflection	96
25	Deflection Interference Coefficient vs a/b_o	97
26	Induced Angle of Attack Due to Rolling Speed	98
27	Roll Damping Moment Coefficient vs a/b_o	99
28	Components of the Fin Normal Force	100
29	Sign Convention for Panel Normal Force, Hinge Moment, and Root Bending Moment	101
30	Fin Planforms Used for Comparison of Theory and Experiment	102

LIST OF FIGURES (continued)

Figure	Title	Page
31	Windward Panel Normal Force vs Roll Angle for Configuration A ($M_{\infty} = .8$)	103
32	Windward Panel Normal Force vs Roll Angle for Configuration A ($M_{\infty} = 1.22$)	104
33	Leeward Panel Normal Force vs Roll Angle for Configuration A ($M_{\infty} = .8$)	105
34	Leeward Panel Normal Force vs Roll Angle for Configuration A ($M_{\infty} = 1.22$)	106
35	Windward Fin Root Bending Moment vs Roll Angle for Configuration A ($M_{\infty} = .8$)	107
36	Windward Fin Root Bending Moment vs Roll Angle for Configuration A ($M_{\infty} = 1.22$)	108
37	Leeward Fin Root Bending Moment vs Roll Angle for Configuration A ($M_{\infty} = .8$)	109
38	Leeward Fin Root Bending Moment vs Roll Angle for Configuration A ($M_{\infty} = 1.22$)	110
39	Windward Fin Hinge Moment vs Roll Angle for Configuration A ($M_{\infty} = .8$)	111
40	Windward Fin Hinge Moment vs Roll Angle for Configuration A ($M_{\infty} = 1.22$)	112
41	Leeward Fin Hinge Moment vs Roll Angle for Configuration A ($M_{\infty} = .8$)	113
42	Leeward Fin Hinge Moment vs Roll Angle for Configuration A ($M_{\infty} = 1.22$)	114

LIST OF FIGURES (continued)

Figure	Title	Page
43	Induced Roll Moment vs α_b for Configuration A ($M_\infty = .8$)	115
44	Induced Roll Moment vs α_b for Configuration A ($M_\infty = 1.22$)	116
45	Spanwise Fin Loading for $\alpha_b = 20^\circ$, $\phi = 20^\circ$ Configuration A ($M_\infty = .8$)	117
46	Induced Roll Moment vs α_b for Configuration B	118
47	Induced Roll Moment vs α_b for Configuration D	119
48	Roll Damping Moment vs α_b for Configuration E	120
49	Roll Damping Moment vs α_b for Configuration F	121
50	Steady State Roll Rate vs α_b for Configuration E (4° fin cant)	122
51	Interference Lift Ratio vs a/b_o (from Ref. 24)	123
52	Pitch Control Force vs α_b for Configuration B ($\phi = 0^\circ$, $\delta_1 = \delta_3 = 10^\circ$, $\delta_2 = \delta_4 = 0^\circ$)	124
53	Pitch Control Force vs α_b for Configuration C ($\phi = 0^\circ$, $\delta_1 = \delta_3 = 10^\circ$, $\delta_2 = \delta_4 = 0^\circ$)	125
54	Pitch Control Force vs α_b for Configuration D ($\phi = 0^\circ$, $\delta_1 = \delta_3 = 10^\circ$, $\delta_2 = \delta_4 = 0^\circ$)	126
55	Pitch Control Force vs α_b for Configuration B ($\phi = 45^\circ$, $\delta_1 = \delta_2 = \delta_3 = \delta_4 = 10^\circ$)	127
56	Pitch Control Force vs α_b for Configuration C ($\phi = 45^\circ$, $\delta_1 = \delta_2 = \delta_3 = \delta_4 = 10^\circ$)	128
57	Pitch Control Force vs α_b for Configuration D ($\phi = 45^\circ$, $\delta_1 = \delta_2 = \delta_3 = \delta_4 = 10^\circ$)	129

LIST OF FIGURES (continued)

Figure	Title	Page
58	Roll Control Moment vs α_b for Configuration B ($\phi = 0^\circ$, $\delta_1 = -\delta_3 = 10^\circ$, $\delta_2 = \delta_4 = 0^\circ$)	130
59	Roll Control Moment vs α_b for Configuration C ($\phi = 0^\circ$, $\delta_1 = -\delta_3 = 10^\circ$, $\delta_2 = \delta_4 = 0^\circ$)	131
60	Roll Control Moment vs α_b for Configuration D ($\phi = 0^\circ$, $\delta_1 = -\delta_3 = 10^\circ$, $\delta_2 = \delta_4 = 0^\circ$)	132

LIST OF TABLES

Table	Title	Page
I	Geometry of Missiles Used for Comparison of Theory and Experiment	67

LIST OF SYMBOLS

a	body radius
A_e	aspect ratio of fins based on exposed planform area, Eq. (19c)
A_p	planform aspect ratio of fins based on extension through the body, (b^2/S_{fp})
b	fin span
b_o	fin semi-span
B	root bending moment (Fig. 29)
C_l	roll moment coefficient $(l/q_\infty S_b d)$
C_{l_p}	roll damping moment coefficient derivative $(\partial C_l / \partial p)_{p \rightarrow 0}$
C_m	pitch moment coefficient $(m/q_\infty S_b d)$
C_n	yaw moment coefficient $(n/q_\infty S_b d)$
C_n	local normal force coefficient of fin, Eq. (14)
C_N	local normal force coefficient of fin due to angle of attack, Eq. (33)
C_{N_α}	normal force coefficient derivative of fin $(\partial C_N / \partial \alpha)_{\alpha \rightarrow 0}$
C_b	panel root bending moment coefficient $[B/q_\infty (b_o - a) S_f]$
C_h	panel hinge moment coefficient $(H/q_\infty c_r S_f)$
C_p	panel normal force coefficient $(N/q_\infty S_f)$
c_r	root chord of fin
C_y	side force coefficient $(F_y/q_\infty S_b)$
C_z	normal force coefficient $(F_z/q_\infty S_b)$
d	body diameter
F_x, F_y, F_z	forces in the x, y, z directions, respectively (Fig. 1)
H	panel hinge moment (Fig. 29)

LIST OF SYMBOLS (continued)

$\vec{i}, \vec{j}, \vec{k}$	unit vectors in the x,y,z directions, respectively
I_d	fin deflection interference coefficient, Eq. (39)
I_p	rolling motion interference coefficient, Eq. (44)
k_B	interference lift ratio (Fig. 51)
K_p	potential flow lift coefficient, Eq. (34h)
K_v	vortex flow lift coefficient, Eq. (34i)
L_s	length of the vortex sheet, Eq. (6a)
l, m, n	roll, pitch, and yaw moments, respectively (Fig. 1)
M	Mach number
\vec{n}	Unit normal vector for fin surface
N	normal force
N_v	total number of vortices in cross-flow plane
p	dimensionless roll speed ($\dot{\phi} b_o / U_\infty$)
q	dynamic pressure ($1/2 \rho U^2$)
r_c	radius of vortex core
r, ϕ	polar coordinates in cross-flow plane
r_1, ϕ_1	coordinates of primary body vortex
s	complex position in the cross-flow plane ($y + i z$)
S_b	frontal area of missile body (πa^2)
S_f	exposed planform area of a fin, Eq. (19d)
S_{fp}	planform area of two fins including extension through the body, Eq. (40b)
u, v, w	velocities in the x,y,z directions, respectively (Fig. 1)
U	magnitude of velocity
U_c	freestream cross-flow velocity, $U_\infty \sin \alpha_b$

LIST OF SYMBOLS (continued)

v_c, w_c	cross-flow velocities in the y, z directions, respectively, Eqs. (2)
\vec{V}	flow field velocity ($u \vec{i} + v \vec{j} + w \vec{k}$)
x, y, z	body cartesian coordinates (Fig. 1)
y_v, z_v	location of primary body vortex in cross-flow plane
α	angle of attack
α_l	local angle of attack
α_s	stall angle of attack of the fin, Eq. (35b)
Γ_p	strength of the primary body vortex
Γ_s	strength of the vortex sheet
δ_j	control deflection of the j 'th fin (Fig. 10)
σ	geometric scaling factor for fin, Eq.. (20a)
Λ	sweep angle of fin
ξ, η	fin oriented surface coordinates, Eq.. (18)
ρ	fluid density
ϕ	roll angle (Fig. 10)
$\dot{\phi}$	roll rate (rad./sec)

Subscripts:

b	missile body
e	"effective" value of argument
le	leading edge
te	trailing edge
∞	freestream conditions

Superscripts:

\cdot	derivative with respect to time
\wedge	"effective" value of argument

SECTION I

INTRODUCTION

Aerodynamics of missiles at high angle of attack has become increasingly important for modern design requirements. Examples of this are high maneuverability of air-to-air-missiles and high launch angle of attack. At high angle of attack a body of revolution sheds two symmetric vortices from the leeward side of the body and these grow in strength along the length of the body. The missile's attached lifting surfaces are immersed in this vortex wake flow and, consequently, the surface pressure distributions are significantly changed from the potential flow case. This, in turn, causes nonlinearities in the forces and moments produced by the lifting surfaces. These nonlinearities have been known to cause serious flight stability and controllability problems in missile dynamics.

Attempts at predicting the forces and moments produced by lifting surfaces in a symmetric body vortex wake have met with moderate success. Very early work was done by Mello and Sivier¹ for cruciform fin missiles in supersonic flow. References 2 and 3 were reasonably successful for incompressible and supersonic flow, respectively, but they only considered rectangular fin planforms. The approach taken in Refs. 2 and 3 was to calculate the body flow field using a vortex modeling technique and then use this as input to a lifting theory. The most extensive work on the subject has been achieved by Nielson and his associates (see e.g., Refs 4-7). They have attacked the very difficult problem of a general canard-fin-body configuration in transonic

and supersonic flow with both symmetric and asymmetric body vortices and canard vortices. Their approach is a combination of slender body theory, Deffenbaugh's^{8,9} method for the impulse flow analogy, and data base experimental input for fin (or wing) alone characteristics.

The present investigation is concerned with the prediction of fin forces and moments on missiles at high angle of attack in subsonic and transonic flow. The body is assumed to be a circular cylinder with only cruciform fins (or wings) as attached lifting surfaces. The fins are assumed to be planar and have straight leading, trailing, and tip chord edges. The leading edge can have arbitrary sweep back and the trailing edge can be swept back or forward. The missile can have an arbitrary roll (or bank) angle and each fin can have arbitrary control deflection. The vortices shed from the body are assumed to be symmetrically located with respect to the angle of attack plane and of equal strength but opposite rotational sense. The highest angle of attack of the body for which the body vortices remain symmetric depends on the nose fineness ratio, body fineness ratio, and Mach number; but normally this angle is near 25° . The method of calculating the body flow field will be discussed first then the lifting theory for the prediction of fin forces and moments is developed. The body flow field model and lifting theory use some empirical data, but the user of the method need not provide any additional data. A computer program was written to implement the present method.

Extensive comparisons are made between predicted results and experimental measurements. Included in the comparisons are: panel normal force, root bending moment, induced roll moment, nonlinear roll damping moment, pitch (or yaw) control forces, and roll control forces. The force and moment predictions are compared with experimental data for six different fin geometries; these include delta, clipped delta, and rectangular planforms. Predictions for wing alone normal force characteristics are compared with data for rectangular, delta, clipped delta, diamond, arrow, clipped arrow, and trapezoidal planforms. Extensive discussions are given which explain the underlying aerodynamic causes of fin force and moment nonlinearities and how these are related to fin geometry.

SECTION II

AERODYNAMIC ANALYSIS

The general approach to the aerodynamics of the problem is to calculate the body flow field and then calculate the forces and moments of attached lifting surfaces exposed to this flow field. This approach is clearly based on the assumption that the body flow field is not significantly affected by the flow induced by the lifting surfaces. This assumption implies that the present analysis is not appropriate for missile configurations in which the fin root chord is a large portion of the length of the missile body. The present analysis also assumes that there is only one set of lifting surfaces (wings or fins) and that it is arranged in a cruciform configuration. The present approach could be applied to a two or three fin configuration by making appropriate modifications to the lifting theory.

This present approach naturally divides the analysis into two areas: the body flow field and the prediction of lifting surface forces and moments. The model of the body flow field was developed previously in Refs. 2 and 10. For completeness, however, the model and the associated computational procedure will be described in this report. The prediction of lifting surface forces and moments will be described in two phases. First, the lifting theory for calculating the normal force distribution and the total normal force of the lifting surface in uniform approach flow will be described. Second,

the model of the body flow field and the lifting theory will be combined to yield a method for predicting forces and moments of attached lifting surfaces.

1. BODY FLOW FIELD

The flow field of a circular cylindrical body at high angle of attack is dominated by the presence of body vortices and their associated feeding sheets. Figure 1 shows the coordinate system and a schematic of the body vortex wake flow. These vortices increase in strength as the angle of attack or body length increases. To model this complex separated flow, the flow is divided into the cross-flow components, v_c and w_c , and the axial flow component, $U_\infty \cos \alpha_b$. The local flow velocity can then be expressed as:

$$\vec{V} = U_\infty \cos \alpha_b \vec{i} + v_c \vec{j} + w_c \vec{k} \quad (1)$$

It is assumed that the steady, three-dimensional, body flow field can be divided into a constant axial flow component and the two-dimensional, potential, flow about a circular cylinder with vortices in the wake and their associated image vortices inside the cylinder. Essentially all of the vorticity is located inside the vortex cores of the primary body vortices and the vortex feeding sheets connecting the body boundary layer separation points and the primary body vortices. Figure 2 shows the primary and sheet vortices in the cross-flow plane. Using this model the cross-flow velocity components can be written as

$$v_c = \left[\frac{-2U_c a^2 yz}{(y^2 + z^2)^2} + \frac{\Gamma_p}{2\pi} \sum_{j=1}^4 (-1)^j \frac{z - z_j}{(y - y_j)^2 + (z - z_j)^2} + \frac{2\Gamma_s}{\pi(N_v - 4)} \sum_{j=5}^{N_v} (-1)^j \frac{z - z_j}{(y - y_j)^2 + (z - z_j)^2} \right] [1 - e^{-C}] \quad (2a)$$

$$w_c = \left\{ U_c \left[1 + \frac{a^2(y^2 - z^2)}{(y^2 + z^2)^2} \right] - \frac{\Gamma_p}{2\pi} \sum_{j=1}^4 (-1)^j x \frac{y - y_j}{(y - y_j)^2 + (z - z_j)^2} - \frac{2\Gamma_s}{\pi(N_v - 4)} \sum_{j=5}^{N_v} (-1)^j x \frac{y - y_j}{(y - y_j)^2 + (z - z_j)^2} \right\} [1 - e^{-C}] \quad (2b)$$

where

$$C = 1.254 \left[(y - y_v)^2 + (z - z_v)^2 \right] / r_c^2$$

$$y_v, z_v = \begin{cases} y_1, z_1 & y \geq 0 \\ y_4, z_4 & y < 0 \end{cases}$$

and $U_c = U_\infty \sin \alpha_b$ is the free stream cross-flow velocity, a is the body radius, Γ_p is the strength of a primary body vortex, Γ_s is the strength of a vortex sheet, y_j, z_j is the location of the j 'th vortex, N_v is the total number of vortices in the cross-flow plane, and r_c is the vortex core radius. The dependence of $\Gamma_p, \Gamma_s, y_1, z_1$, and r_c on angle of attack and body length is taken from experimental measurements.

The exponential term in Eqs. (2a) and (2b) was included so as to model the solid-body type rotation in the cores of the primary body vortices. This method of approximating the vortex cores yields a cross-flow velocity field which is continuous, whereas simply imposing a solid body rotation onto a potential flow field does not.

Utilizing the assumption of a symmetric vortex wake, the relationship between the locations of all of the vortices in the cross-flow plane becomes

$$\left. \begin{aligned} y_j &= -y_{j+1} = a^2 y_{j-1} / (y_{j-1}^2 + z_{j-1}^2) \\ z_j &= z_{j+1} = a^2 z_{j-1} / (y_{j-1}^2 + z_{j-1}^2) \end{aligned} \right\} \quad \text{for } j = 2, 6, 10, \dots, N_v - 2 \quad (3a)$$

$$y_j = -y_{j-3} \text{ and } z_j = z_{j-3} \quad \text{for } j = 4, 8, 12, \dots, N_v \quad (3b)$$

With these equations the location of all of the vortices can be related to the location of the vortices external to the body in the positive $y - z$ quadrant, i.e., $j = 1, 5, 9, \dots, N_v - 3$.

The location of the right-hand vortex sheet, $s_s = r_s e^{i\phi}$, is given as

$$s_s = \left[a \cos(\pi \phi / 2 \phi_1) + (r_1 + r_c) \sin^2(\pi \phi / 2 \phi_1) / \left\{ 1 + (r_1 + r_c)(\phi_1 - \phi) / a \right\} \right] e^{i\phi} \quad \phi_{ss} \leq \phi \leq \phi_1 \quad (4)$$

where r_1, ϕ_1 is the radial and angular location, respectively, of primary vortex number 1, and ϕ_{ss} is the angle at which the sheet separates from the body. The vortex sheet location, as given by Eq. (4), yields a slight improvement in comparison with experimental data of Ref. 11 as compared with that used in Refs. 2 and 10. Eq. (4) requires that the vortex sheet terminates at the core radius of the primary vortex, whereas the equation

used in Refs. 2 and 10 terminated the sheet at the center of the primary vortex.

ϕ_{ss} is defined as the angle at which the radial location of the sheet achieves a value of 1.01a. Therefore,

$$\begin{aligned} \cos(\pi \phi_{ss}/2 \phi_1) + (r_1 + r_c) \sin^2(\pi \phi_{ss}/2 \phi_1) / \\ \left[a + (r_1 + r_c)(\phi_1 - \phi_{ss}) \right] = 1.01 \end{aligned} \quad (5)$$

The low strength vortices which represent the vortex sheet are equally spaced in arc length along the sheet. The arc length of the vortex sheet is

$$L_s = \int_{\phi_{ss}}^{\phi_1} \left[r_s^2 + \left(\frac{dr_s}{d\phi} \right)^2 \right]^{1/2} d\phi \quad (6a)$$

where r_s is the magnitude of s_s , from Eq. (4), and

$$\begin{aligned} \frac{dr_s}{d\phi} = -(a \pi/2 \phi_1) \sin(\pi \phi/2 \phi_1) + \\ \left[\left\{ (r_1 + r_c) \pi/\phi_1 \right\} \sin(\pi \phi/2 \phi_1) \cos(\pi \phi/2 \phi_1) \left\{ 1 + \right. \right. \\ \left. \left. (r_1 + r_c)(\phi_1 - \phi)/a \right\} + \left\{ (r_1 + r_c)^2/a \right\} \sin^2(\pi \phi/2 \phi_1) \right] / \\ \left\{ 1 + (r_1 + r_c)(\phi_1 - \phi)/a \right\}^2 \end{aligned} \quad (6b)$$

The first vortex in the sheet, vortex number 5, is located at the point where the sheet leaves the body so that $r_5 = 1.01a$ and $\phi_5 = \phi_{ss}$. The angular position for vortex numbers 5, 9, 13, ..., $N_v - 3$ is found from

$$\left(\frac{j - 5}{N_v - 4} \right) L_s = \int_{\phi_{ss}}^{\phi_j} \left[r_s^2 + \left(\frac{dr_s}{d\phi} \right)^2 \right]^{1/2} d\phi \quad (7)$$

Once the angular position is known from Eq. (7), then from Eq. (4), one obtains the radial location:

$$r_j = a \cos(\pi \phi_j/2 \phi_1) + (r_1 + r_c) \sin^2(\pi \phi_j/2 \phi_1) / \left\{ 1 + (r_1 + r_c)(\phi_1 - \phi_j)/a \right\} \quad (8)$$

The experimental inputs required by the theory will now be discussed. The total strength of all the vorticity, Γ_t , (primary vortex and feeding sheet) in each half-plane of the wake is taken from the experimental data of Grosche¹².

$$\Gamma_t/(\pi d U_\infty) = .35(x/a - 6) \alpha_b^2 \quad \text{for } x/a > 6 \quad (9)$$

This equation represents the data of Grosche for $7^\circ \leq \alpha_b \leq 20^\circ$ and $5 \leq x/d \leq 13$ for incompressible flow. No extensive body vortex wake surveys have been conducted in compressible subsonic flow.

The division of vorticity between the primary vortex and the feeding sheet is taken from a correlation of data given in Ref. 11. This correlation is represented by

$$\frac{\Gamma_p}{\Gamma_t} = 1 - .15(x/a) \alpha_b + .008(x/a)^2 \alpha_b^2 \quad (10)$$

where $\Gamma_t = \Gamma_p + \Gamma_s$. Although the data from Ref. 11 is for supersonic flow, it is a reasonable assumption that the ratio of primary vortex strength to total vorticity is the same in subsonic and supersonic flow.

The location of the primary vortex is taken from the experimental data of Grosche¹², Tinling and Allen¹³, and Fidler, Nielsen and Schwind.¹⁴ The experimental data for the location of the right-hand primary vortex (vortex number 1) in polar coordinates is approximated by

$$\phi_1 = 74^\circ$$

(11)

$$r_1/a = .70 + .06 \sqrt{M_\infty + 1} (x/a + 6) \sqrt{\alpha_b}$$

These equations incorporate the moderate increase in radial location of the vortex center with Mach number measured by Tinling and Allen.

The radius of the vortex core is taken from the data of Ref. 11. A fit of the data for angles of attack of 10° and 15° and body lengths from 7 to 14 calibers is given by

$$r_c/a = .030(x/a) \sqrt{\alpha_b}$$

(12)

The computational procedure for the body flow field model will now be discussed. The order of calculation is as follows:

- (1) α_b and x are set.
- (2) Γ_t is calculated from Eq. (9).
- (3) Γ_p and Γ_s are calculated from Eq. (10).
- (4) ϕ_1 and r_1 are calculated from Eq. (11).
- (5) r_c is calculated from Eq. (12).
- (6) ϕ_{ss} is computed from Eq. (5) by increasing ϕ_{ss} from 0° in increments of $.01\phi_1$ until Eq. (5) is satisfied. Recall that $\phi_{ss} = \phi_5$ and $r_5 = 1.01a$.
- (7) L_s is calculated from Eq. (6) by Simpson's Rule.
- (8) ϕ_j for $j = 9, 13, \dots, N_v - 3$ is calculated from Eq. (7) by increasing ϕ_j from ϕ_{j-4} in increments of $.01\phi_1$ until

the integral equation is satisfied. The integral is evaluated by Simpson's Rule. In the present work N_v is set at 44, that is, 10 vortices in each sheet.

- (9) r_j for $j = 9, 13 \dots N_v - 3$ is calculated from Eq. (8).
- (10) y_j, z_j for $j = 1, 5, 9 \dots N_v - 3$ are calculated from ϕ_j, r_j using the polar to cartesian transformation.
- (11) y_j, z_j for all remaining vortices are calculated from Eq. (3).
- (12) v_c, w_c are calculated from Eq. (2).

2. LIFTING THEORY

Various lifting theories were considered for use with the present flow model for the prediction of forces and moments produced by fins. The criteria by which a lifting theory was chosen was that the theory must be able to consider very nonuniform, rotational, approach flow and it must include fin stall and post-stall characteristics. These criteria quickly limited the possible theories to strip theory. In strip theory it is assumed that the normal force on a chordwise strip of fin can be calculated by using the local dynamic pressure and angle of attack of the strip, independent of adjacent chordwise strips. Significant elements included in the present lifting theory are the following: normal force distribution over the lifting surface depends upon fin aspect ratio and leading and trailing edge sweep, individual control deflection of each fin is allowed, fin-fin interference due to both control deflection and rolling rate is included, normal force depends upon freestream Mach number, and nonuniform approach flow alters the effective leading edge sweep.

a. Local Normal Force

The local normal force on a differential element of the fin surface is written as (see Fig. 3)

$$dN = C_n q dx dr \quad (13)$$

where C_n is the local normal force coefficient and q is the local dynamic pressure, including that due to missile rolling speed. The local normal force coefficient C_n is composed of three separate functions: first, the normal force due to the local angle of attack of the differential element; second, the local chordwise distribution; and third, the local spanwise distribution. Assuming a product form of the function, one has

$$C_n = \sigma C_N(\alpha_l) C(x,r) S(r) \quad (14)$$

where σ is a geometric scaling factor, $C_N(\alpha_l)$ is the local normal force coefficient due to local angle of attack, and $C(x,r)$ and $S(r)$ are the chordwise and spanwise normal force distributions, respectively, for uniform approach flow.

For arbitrary planform fins it greatly simplifies matters if C and S are written in terms of appropriate fin oriented coordinates. To determine the appropriate fin oriented variables, first write the x coordinate of the leading and trailing edges of the fin as

$$x_{le} = x_1 + (x_2 - x_1)(r - a)/(b_o - a) \quad (15)$$

$$x_{te} = x_3 + (x_4 - x_3)(r - a)/(b_o - a)$$

where x_1 , x_2 , x_3 , and x_4 are defined in Fig. 3, and b_o is the semi-span of the fin. x_2 , x_3 , and x_4 can be related to the leading edge sweeps Λ_{le} , the trailing edge sweep Λ_{te} and the root chord of the fin c_r as

$$x_2 = x_1 + (b_o - a) \tan \Lambda_{le} \quad (16)$$

$$x_3 = x_1 + c_r$$

$$x_4 = x_3 + (b_o - a) \tan \Lambda_{te}$$

Substituting these equations into Eqs. (15), one obtains

$$x_{le} = x_1 + (r - a) \tan \Lambda_{le} \quad (17)$$

$$x_{te} = x_1 + c_r + (r - a) \tan \Lambda_{te}$$

Using the boundaries of the fin planform, i.e., x_{le} , x_{te} , a , and b_o , as scaling variables, then a convenient set of fin oriented coordinates are

$$\xi = (x - x_{te})/(x_{le} - x_{te}) \quad (18)$$

$$\eta = (r - a)/(b_o - a)$$

where ξ is the chordwise variable and η is the spanwise variable (Fig 4).

b. Normal Force Distribution

Experimental data¹⁵⁻¹⁹ for the normal force distribution over the surface of a number of fin planforms was studied in order

to arrive at general expressions for $C(\xi)$ and $S(\eta)$. After devising and testing a considerable number of expressions for the chordwise and spanwise distributions, the following equations were adopted

$$C(\xi) = \sqrt{\xi} \exp\left[\xi^2 / \sqrt{\cos \Lambda_{le}}\right] \quad (19a)$$

$$S(\eta) = \left(1 + \eta^{2A_e}\right) \sqrt{1 - \eta^2} \quad (19b)$$

where

$$A_e = 2 (b_o - a)^2 / S_f \quad (19c)$$

$$S_f = \frac{1}{2} (b_o - a)^2 \left[2 c_r / (b_o - a) - \tan \Lambda_{le} + \tan \Lambda_{te} \right] \quad (19d)$$

A_e is the exposed aspect ratio, that is, the aspect ratio of the lifting surface formed by eliminating the body and placing the root chords of two adjacent fins together. S_f is the planform area of a single fin. Eqs. (19a) and (19b) have been shown to give valid results for exposed aspect ratios from .5 to 5, leading edge sweep from 0° to 80° , and trailing edge sweep from -60° to 80° .*

The normal force distribution over the surface of the fin for uniform approach flow is then provided by the product of Eqs. (19a) and (19b). This expression was compared qualitatively with experimental data by means of a three-

*The pressure distributions from Eqs. (19a) and (19b) were qualitatively compared with experimental data of Refs. 15-19.

dimensional computer graphics routine, DISSPLA. This routine provided a means of visualizing the normal force distribution over the surface of the fin. Shown in Figs. 5 through 9 are sets of three-dimensional perspective plots of typical planforms examined. Figure 5 shows a sequence of untapered fins with $\Lambda_{le} = \Lambda_{te} = 60^\circ$ for $A_e = .5, 1, \text{ and } 3$. The view in the perspective plot is from behind and above the fin surface looking upstream, and slightly in-board. The graphics routine uses a rectangular area over which the surface function is defined.* Consequently, the regions which show a surface value of zero are not part of the fin planform. For example, on Fig. 5 the trailing edge of the fin is located at the junction of the nonzero and zero surface values. Another point to note on the perspective plots is a "spike" character at the leading edge of the planform. This characteristic is not inherent in the equations but simply is a result of the mesh size on the surface and the zero value of the surface just ahead of the leading edge.

Figure 6 shows a sequence of fins with $\Lambda_{le} = 60^\circ$, $\Lambda_{te} = 20^\circ$ for $A_e = .5, 1, \text{ and } 2.92$. In Fig. 6 the taper ratio decreases until in Fig. 6c an arrow wing is achieved. Note in this sequence of figures that as the leading edge becomes longer the normal force loading reflects the very high loading near the leading edge due to the increasing strength of the leading edge vortex.

* The units on the span coordinate and the local normal force coordinate in the figures have no physical significance.

Figure 7 shows a rectangular planform for $A_e = .5, 1.,$ and $3.$ For the low aspect ratio planform (Fig. 7a) note the increase in normal force near the tip chord due to the tip vortex increasing in strength along the tip chord. For the high aspect ratio planform (Fig. 7c) it can be seen that the spanwise load distribution nears the classical elliptic loading.

Figure 8 presents the loading for $\Lambda_{le} = 60^\circ, \Lambda_{te} = 0^\circ$ and $A_e = .5, 1.,$ and $2.31.$ Figs. 8a and 8b show clipped deltas and Fig. 8c shows a delta planform. Comparing the distribution for the delta planform with experimental data¹⁸ it is found that the empirical equation models the data except near the leading edge.

Figure 9 shows a trapezoid planform with decreasing taper ratio, $\Lambda_{le} = -\Lambda_{te} = 40^\circ$ and $A_e = .5, 1.,$ and $2.38.$ The planform with $A_e = 2.38$ (Fig. 8c) has a taper ratio of zero and is, therefore, a diamond planform.

The geometric scaling factor in Eq. (14) can now be determined. σ is evaluated by the requirement that the integrated average of the assumed normal force distribution over the surface of the fin must be unity, i.e., the assumed normal force loading must be normalized. Therefore, one may write

$$q_\infty \int_{fin} C_n dA = q_\infty C_N S_f$$

Substituting C_n from Eq.. (14), one has

$$\sigma \int_a^{b_0} \int_{x_{le}}^{x_{te}} C(x,r) S(r) dx dr = S_f$$

Transforming to the fin coordinates ξ, η (Eq. 18) and solving for σ , one obtains

$$\sigma = \frac{S_f}{(b_0 - a) \int_0^1 \int_0^1 \Omega(\eta) C(\xi) S(\eta) d\xi d\eta} \quad (20a)$$

where

$$\Omega(\eta) = c_r - (b_0 - a)(\tan \Lambda_{le} - \tan \Lambda_{te})\eta \quad (20b)$$

and $C(\xi)$ and $S(\eta)$ are given by Eqs. (19).

c. Local Angle of Attack

Referring back to Eq. (14), C_N depends on the local angle of attack of the chordwise strip. The local angle of attack is calculated by utilizing the unit normal vector of the fin surface, \vec{n} , and the total velocity \vec{V} (Fig. 10). The geometric local angle of attack can be shown to be

$$\alpha_l = \sin^{-1} \left[\vec{n} \cdot \vec{V} / (|\vec{n}| |\vec{V}|) \right] \quad (21)$$

The surface normal vector of the fin depends on the roll angle ϕ and the control deflection of each fin δ_j , $j = 1, 2, 3, 4$. Let the sign convention of the control deflection of each fin be as follows: positive control deflection of fins 1 and 3 produces a positive normal force, i.e., a pitch down maneuver, and positive control

deflection of fins 2 and 4 produces a positive side force, i.e., a yaw left maneuver (see Fig. 10). The sign convention for the surface normal vector, however, is such that the vector always points in the counter-clockwise direction. Referring to Fig. 10, the surface normal vector is

$$\vec{n} = \sin(\Delta \delta_j) \vec{i} - \cos(\delta_j) \sin \phi \vec{j} + \cos(\delta_j) \cos \phi \vec{k} \quad (22)$$

where

$$\Delta = \cos \phi / |\cos \phi|$$

Δ simply provides the sign of δ_j which is consistent with the above mentioned sign convention.

The local total velocity, i.e., the velocity of the fluid relative to the chordwise strip, is composed of two types of terms; first, the fluid velocity relative to the fixed coordinate system, and second, the velocity of the fixed coordinate system relative to the spinning chordwise strip. Therefore, using Eq. (1) it can be written

$$\vec{V} = U_{\infty} \cos \alpha_b \vec{i} + (v_c + \dot{\phi} r \sin \phi) \vec{j} + (w_c - \dot{\phi} r \cos \phi) \vec{k} \quad (23)$$

where v_c and w_c are given by Eq. (2) and $\dot{\phi}$ is the roll rate of the missile.

The axial location at which the flow model is evaluated is calculated from the fin planform characteristics. The axial location is chosen to be the average quarter chord

location of the root and tip chords. That is,

$$x_v = (x_1 + .25c_r + x_2 + .25c_t)/2$$

where x_v is the axial location of the vortex model and

c_t is the length of the tip chord. Rewriting this equation, one has

$$x_v = x_1 + (.25c_r + .25c_t + (b_o - a) \tan \Lambda_{fe})/2$$

This axial location is used in Eqs. (9) through (12).

The geometric local angle of attack can now be calculated by substituting Eqs. (22) and (23) into Eq. (21). Interference between fins, however, will alter α_l for control deflection and a rolling missile. These interference effects will be considered in Section II-3, Roll Moment.

d. Effective Aspect Ratio

Now consider an aerodynamic effect which occurs when the lifting surface is attached to the missile body. If the body is at high angle of attack then the angle in the plane of the fin between the approach flow and the fin leading edge can vary significantly, depending on the roll angle of the body. That is, the fin is yawed with respect to the approach flow for various roll angles around the body. This yaw angle results in an effective change in the leading and trailing edge sweep and effective aspect ratio of the fin. A simple example of this is to consider fin 4 at a roll angle of 0° with the body at

angle of attack α_b (see Fig. 10). Then the effective leading edge sweep of fin 4 at $\phi = 0^\circ$ is approximately $\Lambda_{le} - \alpha_b$. If $\Lambda_{le} = 0^\circ$, then the fin at this roll angle would actually be swept forward.

The effective leading edge sweep, $\hat{\Lambda}_{le}$, and effective trailing edge sweep, $\hat{\Lambda}_{te}$, are derived by relating the average flow velocity along the fin to the leading and trailing edge unit vectors, respectively. The most convenient coordinate system to use is cylindrical coordinates with the orthogonal unit vectors located in the plane of the fin (see Fig. 11). Let \bar{v}_c and \bar{w}_c be the average crossflow velocity components along the exposed semispan of the fin at a given roll angle. Then

$$\bar{v}_c = \frac{1}{b_o - a} \int_a^{b_o} v_c(r, \phi) dr$$

$$\bar{w}_c = \frac{1}{b_o - a} \int_a^{b_o} w_c(r, \phi) dr$$

where v_c and w_c are given by Eqs. (2). Rewriting these equations in terms of fin oriented coordinates, one has

$$\bar{v}_c = \int_0^1 v_c(\eta, \phi) d\eta \quad (24a)$$

$$\bar{w}_c = \int_0^1 w_c(\eta, \phi) d\eta \quad (24b)$$

Using the cylindrical coordinate unit vectors \vec{e}_x, \vec{e}_r , shown in Fig. 11, the average velocity along the leading edge is

$$\vec{V} = \bar{u} \vec{e}_x + \bar{v}_r \vec{e}_r$$

where

$$\bar{u} = U_\infty \cos \alpha_b$$

$$\bar{v}_r = \bar{v}_c \cos \phi + \bar{w}_c \sin \phi$$

As the sweep angle is measured from a line perpendicular to the approach velocity, the unit vector perpendicular to the average velocity is

$$\vec{V}_\perp = -\bar{v}_r / \sqrt{\bar{u}^2 + \bar{v}_r^2} \vec{e}_x + \bar{u} / \sqrt{\bar{u}^2 + \bar{v}_r^2} \vec{e}_r \quad (25)$$

The leading edge unit vector is

$$\vec{e}_{le} = \sin \Lambda_{le} \vec{e}_x + \cos \Lambda_{le} \hat{e}_r \quad (26)$$

The effective leading edge sweep angle is the angle between \vec{V}_\perp and \vec{e}_{le} . Using the scalar product, one obtains

$$\hat{\Lambda}_{le} = \cos^{-1}(\vec{V}_\perp \cdot \vec{e}_{le})$$

Substituting in Eqs. (25) and (26),

$$\hat{\Lambda}_{le} = \cos^{-1} \left[(\bar{u} \cos \Lambda_{le} - \bar{v}_r \sin \Lambda_{le}) / \sqrt{\bar{u}^2 + \bar{v}_r^2} \right] \quad (27)$$

This expression presents difficulties in evaluation because the arc cosine function is double valued. This problem can be nicely circumvented by noticing that the argument of the arc cosine function suggests $\hat{\Lambda}_{le}$ might be split into two angles. Let

$$\hat{\Lambda}_{le} = \Lambda_{le} + \epsilon_{le} \quad (28)$$

where ϵ_{le} is the deviation of the effective leading edge sweep from the geometric leading edge sweep. Now Eq. (27) can be written as

$$\cos(\Lambda_{le} + \epsilon_{le}) = \frac{\bar{u}}{\sqrt{\bar{u}^2 + \bar{v}_r^2}} \cos \Lambda_{le} - \frac{\bar{v}_r}{\sqrt{\bar{u}^2 + \bar{v}_r^2}} \sin \Lambda_{le}$$

Using the trigonometric identity for the cosine of a sum, one has

$$\cos \epsilon_{le} \cos \Lambda_{le} - \sin \epsilon_{le} \sin \Lambda_{le} = \frac{\bar{u}}{\sqrt{\bar{u}^2 + \bar{v}_r^2}} \cos \Lambda_{le} - \frac{\bar{v}_r}{\sqrt{\bar{u}^2 + \bar{v}_r^2}} \sin \Lambda_{le}$$

Matching terms one notes that two mathematically equivalent expressions can be written for ϵ_{le} . The one involving the cosine function, however, suffers from the same difficulty mentioned above. Therefore, use

$$\sin \epsilon_{le} = \bar{v}_r / \sqrt{\bar{u}^2 + \bar{v}_r^2}$$

Substituting this into Eq. (28), one finally obtains

$$\hat{\Lambda}_{le} = \Lambda_{le} + \sin^{-1} \left(\bar{v}_r / \sqrt{\bar{u}^2 + \bar{v}_r^2} \right) \quad (29a)$$

Using exactly the same procedure, the effective trailing edge sweeps is

$$\hat{\Lambda}_{te} = \Lambda_{te} + \sin^{-1} \left(\bar{v}_r / \sqrt{\bar{u}^2 + \bar{v}_r^2} \right) \quad (29b)$$

The effective leading and trailing edge sweep due to high angle of attack results in an effective aspect ratio of the fin. This is significant in that the local normal force coefficient due to angle of attack, $C_N (\alpha_f)$, will now reflect effective changes in fin geometry due to apparent yaw of the fin. To derive an expression for \hat{A}_e , begin with the definition of A_e :

$$A_e = 2(b_o - a)^2 / S_f$$

where S_f is the exposed planform area of a fin. Writing this in terms of fin semispan, root chord, and leading and trailing edge sweep, one has

$$A_e = 4 \left[2c_r / (b_o - a) - \tan \Lambda_{le} + \tan \Lambda_{te} \right] \quad (30)$$

Referring to Fig. 12, it can be seen that the exposed fin semispan and root chord also effectively change. It can be shown that

$$\widehat{b_o - a} = (b_o - a) \cos \hat{\Lambda}_{le} / \cos \Lambda_{le} \quad (31a)$$

$$\hat{c}_r = c_r \cos \Lambda_{te} / \cos (\hat{\Lambda}_{le} - \Lambda_{le} + \Lambda_{te}) \quad (31b)$$

Using Eqs. (30) and (31), the effective aspect ratio is written as

$$\hat{A}_e = \frac{4}{\frac{2c_r \cos \Lambda_{le} \cos \Lambda_{te}}{(b_o - a) \cos \hat{\Lambda}_{le} \cos(\hat{\Lambda}_{le} - \Lambda_{le} + \Lambda_{te})} - \tan \hat{\Lambda}_{le} + \tan \hat{\Lambda}_{te}} \quad (32)$$

e. Expression for $C_N(\alpha_\ell)$

The functional dependence of C_N on the local angle of attack is given by an empirical expression based on lifting surfaces in uniform approach flow. Other investigators (see, for example, Ref. 6) have used experimental data for $C_N(\alpha_\ell)$ directly in their analysis. This is rarely an appealing approach because it requires vast amounts of data to construct a data base sufficiently general to address general planforms over a large range of Mach numbers. Also, this is not possible in the present approach because the effective geometry of the fin, discussed earlier, changes with the character of the nonuniform approach flow.

As the local angle of attack on a missile fin can be on the order of 40° to 50° when the angle of attack of the body is 25° , the expression for $C_N(\alpha_\ell)$ must include pre-stall, stall and post-stall characteristics. The pre-stall expression for $C_N(\alpha_\ell)$ is taken from the work of Lecat and Rietschlin.²⁰ Their analysis is based on Polhamus²¹ suction analogy. They have extended the original work of Polhamus on delta wings to include arbitrary planforms

and transonic flow. Their analysis is not repeated here, but simply their equations are given in the present nomenclature.

Their expression for $C_N(\alpha)$ is

$$C_N(\alpha) = K_p \sin \alpha \cos \alpha + K_v \sin^2 \alpha \quad (33)$$

Note that this equation shows C_N continually increasing with α and, as a result, is not appropriate for angles near or greater than the stall angle. Although Lecat and Reitschlin state their method is applicable to subsonic and supersonic flow, the present analysis is considered appropriate for subsonic flow and only supersonic flow with subsonic leading edges.

The calculation procedure for K_p and K_b is as follows:

- (1) Calculate $\widehat{b_o - a}$, \hat{c}_r , and \hat{A}_e from Eqs. (31) and (32)
- (2) Calculate the distance from x_1 to the aftmost point of maximum span, c_r^* .

$$c_r^* = \hat{c}_r + (\widehat{b_o - a}) \tan \hat{\Lambda}_{te} \quad (34a)$$

- (3) Calculate the sweep of the semispan diagonal, γ .

$$\gamma = \tan^{-1} \left[\hat{c}_r / (\widehat{b_o - a}) + \tan \hat{\Lambda}_{te} \right] \quad (34b)$$

- (4) Calculate the ratio of planform area to rectangular reference area, S_f/S_f^* .

$$S_f/S_f^* = \left[\frac{\widehat{b_o - a}}{c_r^*} \right] \quad (34c)$$

- (5) If $M_\infty > 1$, calculate the complement of the Mach angle, γ_M .

$$\gamma_M = \cos^{-1}(1/M_\infty) \quad (34d)$$

- (6) Calculate the planform parameter p^* .

$$p^* = \begin{cases} S_f/S_f^* & \text{for } M_\infty \leq 1 \\ \frac{S_f/S_f^*}{1 - [\tan \gamma_M / (2 \tan \gamma)]} & \text{for } M_\infty > 1 \end{cases} \quad (34e)$$

- (7) Calculate the planform angle ψ .

$$\psi = \begin{cases} \tan^{-1}(2p^* \tan \gamma) & M_\infty \leq 1 \\ \tan^{-1}[2p^* (\tan \gamma - \tan \gamma_M)] & M_\infty > 1 \end{cases} \quad (34f)$$

- (8) Calculate the compressibility factor β .

$$\beta = \begin{cases} \sqrt{1 - M_\infty^2} & \text{for } M_\infty \leq 1 \\ \sqrt{M_\infty^2 - 1} & \text{for } M_\infty > 1 \end{cases} \quad (34g)$$

- (9) Calculate the potential flow lift coefficient, K_p .

$$K_p = \frac{4\pi}{\tan \psi + \sqrt{\tan^2 \psi + (\sin^2 \psi / p^{*2})} + 4\beta^2} \quad (34h)$$

(10) Calculate the vortex flow lift coefficient, K_v .

$$K_v = \left[K_p - (K_p^2 \tan \psi) / 4\pi \right] \sqrt{1 + \tan^2 \psi} \quad (34i)$$

An empirical expression was devised for the normal force coefficient $C_N(\alpha_l)$ based on the expression of Lecat and Rietschlin, Eq. (33). The new expression is more general in the sense that it applies at stall and beyond stall. This expression was constructed after examining and comparing a large number of trial expressions with experimental data^{10,15-23} for a wide variety of planforms. This expression is

$$C_N(\alpha_l) = \begin{cases} \left(K_p \sin \alpha_l \cos \alpha_l + K_v \sin^2 \alpha_l \right) \left[1 - (1-\mu)(\alpha_l/\alpha_s)^3 \right] & 0 \leq \alpha_l \leq \alpha_s \\ f(A_e, \Lambda_{le}) C_N(\alpha_s) + \left[A_e \cos \Lambda_{le} C_N(\alpha_l - \alpha_s) \right] / 10 & \alpha_s < \alpha_l \leq 2\alpha_s \\ f(A_e, \Lambda_{le}) C_N(\alpha_s) + \left[A_e \cos \Lambda_{le} C_N(\alpha_s) \right] / 10 & 2\alpha_s < \alpha_l \end{cases} \quad (35a)$$

where the symbol $\langle \rangle$ is used to denote functional dependence in situations where the standard symbol $()$ would be confusing. Also

$$\mu = .9 - .2 A_e \sin 2\Lambda_{le}$$

$$\alpha_s = 38 \left[1 + .62(A_e - 2)^4 \right] \left[1 + 1.1 (A_e - 1)^{2.5} \cos^2 \Lambda_{le} \right] \times \left\{ 1 + \left[6(A_e - 1)^2 \sin^4 \Lambda_{le} \right] / e^{A_e} \right\} / \left[\cos \Lambda_{le} + 1 \right]^{2(A_e - 1)} \quad (35b)$$

$$f(A_e, \Lambda_{le}) = 1 - .35 \left\{ 1 + \frac{1}{8} e^{A_e} \sin^{\frac{1}{A_e}} \Lambda_{le} \sin \left[(A_e - 2.1) \Lambda_{le} \right] \right\} / \left[1 + .5(A_e - 1)^3 \right] \quad (35c)$$

and K_p and K_v are given by Eqs. (33).

As can be seen, $C_N(\alpha_l)$ is composed of three angle of attack ranges: zero angle up to the stall angle, stall up to twice the stall angle, and angles larger than twice the stall angle. For the first range, angles less than α_s , the expression of Lecat and Reitschlin²⁰, Eq. (33), has been modified for α_l near α_s . Eq. (35a) for $\alpha_l < \alpha_s$ shows that as α_l approaches α_s the normal force coefficient increases more slowly. This characteristic is consistent with experimental measurements. The parameter μ represents the portion of C_N predicted by Lecat and Reitschlin which remains at $\alpha_l = \alpha_s^-$. The expression for α_s , although rather lengthy, gives a good estimate of the stall angle (in degrees) for planforms with aspect ratios from 1 to 5 and leading edge sweep from 0° to 70° . $f(A_e, \Lambda_{le})$ represents the portion of $C_N(\alpha_s)$ existing for $\alpha_l = \alpha_s^+$. Note that μ , α_s and $f(A_e, \Lambda_{le})$ show no dependence on freestream Mach number. This is not necessarily a reflection of the physics, but simply an admission of lack of data.

$C_N(\alpha_l)$ as predicted by Eq. (35) was compared with data for a very wide variety of planform geometries in order to determine its range of applicability. Figures 13 through 22 show typical comparisons of Eq. (35) with experimental data for incompressible flow. The figures are placed in order of increasing aspect ratio from 1 to 4. The leading edge sweep angle varies from 0° to 70° and planform geometries include: rectangular, diamond, clipped delta, delta, arrow, clipped arrow, and trapezoidal. The comparisons are good for all planforms except that for the

aspect ratio 3 trapezoid (Fig. 21) and rectangular planforms of $A_e \geq 3$ (comparisons not shown). For these type planforms, i.e., high aspect ratio with small leading edge sweep, the normal force past stall is significantly over estimated with the present expression.

f. Fin - Fin Interference

Two types of fin - fin interference are included in the present lifting theory. The first type is that due to control deflection of the fins and the second type is due to rolling motion of the missile. When a control deflection is input to a fin the lifting flow field of that fin induces an angle of attack on the adjacent fins. This induced angle of attack causes the adjacent fins to generate forces and moments dependent on the magnitude and direction of the control input. Rolling motion interference occurs for a similar reason except that the angle of attack of a fin is generated by the angular velocity of the fin relative to the oncoming stream. Control deflection interference will be considered first and then rolling motion interference will be analyzed. Results of slender body theory are used to evaluate both types of interference considered here.

Figure 23 (taken from Ref. 24) shows the interference flow fields and pressures induced on adjacent fins for two types of control input: positive pitch control and positive roll control with horizontal fins. For the pitch control it is seen that a negative pressure coefficient

is produced on both sides of the top fin and a positive pressure coefficient is generated on both sides of the bottom fin. For roll control, i.e., differential deflection, a negative pressure is generated on the top right and bottom left sides of the fins and a positive pressure is generated on the top left and bottom right sides of the fin. In the present analysis these induced pressures are included by considering the adjacent fins to be at an effective deflection angle.

Consider the induced pressures on adjacent fins for individual deflection of each fin. Shown in Fig. 24 is the induced pressure and effective deflection force for positive deflection of each fin. If we let I_d be the deflection interference coefficient, then the following equations describe the interference depicted in Fig. 24.

$$\delta_1 > 0 \left\{ \begin{array}{l} \delta_{e2} = I_d \delta_1 \\ \delta_{e3} = 0 \\ \delta_{e4} = -I_d \delta_1 \end{array} \right. \quad \delta_2 > 0 \left\{ \begin{array}{l} \delta_{e1} = I_d \delta_2 \\ \delta_{e3} = -I_d \delta_2 \\ \delta_{e4} = 0 \end{array} \right.$$

(36)

$$\delta_3 > 0 \left\{ \begin{array}{l} \delta_{e1} = 0 \\ \delta_{e2} = -I_d \delta_3 \\ \delta_{e4} = I_d \delta_3 \end{array} \right. \quad \delta_4 > 0 \left\{ \begin{array}{l} \delta_{e1} = -I_d \delta_4 \\ \delta_{e2} = 0 \\ \delta_{e3} = I_d \delta_4 \end{array} \right.$$

Summing all of the effective control deflections given in Eqs. (36) and including the actual control deflection, one obtains

$$\begin{aligned}
 \delta_{e_1} &= \delta_1 + I_d(\delta_2 - \delta_4) \\
 \delta_{e_2} &= \delta_2 + I_d(\delta_1 - \delta_3) \\
 \delta_{e_3} &= \delta_3 + I_d(\delta_4 - \delta_2) \\
 \delta_{e_4} &= \delta_4 + I_d(\delta_3 - \delta_1)
 \end{aligned} \tag{37}$$

I_d is evaluated by using the slender body theory results of Adams and Dugan.²⁵ They derived results for the roll moment coefficient derivative, $C_{l\delta}$, versus a/b_0 for differential deflection of two fins. They further showed results for the roll moment coefficient induced on the vertical fins due to differential deflection of the horizontal fins. Assuming the induced angle of attack of the upwash and downwash of the deflected fin on the undeflected fin is constant along the span, then one can write

$$\frac{\left[C_{l\delta} \right]_{\text{induced}}}{\left[C_{l\delta} \right]_{\text{deflected}}} = \frac{\delta_e}{\delta} \tag{38}$$

This equation can be proven, given the stated assumption, by writing the roll moment of the induced and deflected fin in double integral form. Noting that the ratio shown in Eq. (38) is for differential deflection of two fins, one has

$$I_d = \frac{1}{2} \frac{\left[C_{\ell \delta} \right]_{\text{induced}}}{\left[C_{\ell \delta} \right]_{\text{deflected}}} \quad (39)$$

Figure 25 plots I_d versus a/b_0 using the results of Adams and Dugan for $\left[C_{\ell \delta} \right]_{\text{induced}}$ and $\left[C_{\ell \delta} \right]_{\text{deflected}}$. It should be noted that they use the planform aspect ratio of the fins, A_p . In the present nomenclature

$$A_p = b^2 / S_{fp} \quad (40a)$$

where S_{fp} is the planform area of two fins including their imaginary extension through the body. It can be shown that

$$S_{fp} = 2S_f + a \left[2 c_r + a (\tan \Lambda_{le} - \tan \Lambda_{te}) \right] \quad (40b)$$

I_d , as given in Fig. 25, is used in Eqs. (37) to calculate the effective control deflection of each fin.

Now consider the case of fin - fin interference due to rolling motion. The strategy of this derivation is to determine the interference coefficient by matching the present roll moment formulation for zero angle of attack of the body to that obtained by slender body theory. Assuming $\alpha_b = 0$

and the rolling speed is $\dot{\phi}$, then the differential roll moment can be written (Fig. 26)

$$d\ell = 4 r C_n \frac{1}{2} \rho_\infty \left[U_\infty + (\dot{\phi} r) \right]^2 dx dr$$

Assuming the rolling speed is small compared to U and substituting in C_n from Eq. (14), one has

$$d\ell = 4 q_\infty r \sigma C_N(\alpha_e) C(x, r) S(r) dx dr \quad (41a)$$

where α_e is the effective local angle of attack along the span. Adams and Dugan²⁵ showed that the spanwise loading induced on one fin by the other fins was roughly quadratic along the span. In the present analysis this induced loading will be simply approximated by a linear spanwise function. Therefore,

$$\alpha_e = - \frac{\dot{\phi} r}{U_\infty} + I_p \frac{\dot{\phi} r}{U_\infty} \quad (41b)$$

where I_p is the rolling motion interference coefficient. The first term in Eq. (41b) is the local angle of attack due to rolling speed and the second term is the reduction in local angle of attack due to fin - fin interference.

Integrating over the surface of the fin, Eq. (41a) becomes

$$\ell = 4 \sigma q_\infty \int_a^{b_0} \int_{x_{le}}^{x_{te}} r C_N(\alpha_e) C(x, r) S(r) dr dx \quad (42)$$

Assuming α_e is small and using Eq. (41b), Eq. (42) can be written

$$\ell = -4 \sigma q_{\infty} C_{N_{\alpha}} (1 - I_p) \frac{\dot{\phi}}{U_{\infty}} \int_a^{b_0} \int_{x_{le}}^{x_{te}} r^2 C(x, r) S(r) dx dr$$

Transforming coordinates (x, r) to fin coordinates (ξ, η) and non-dimensionalizing with respect to $q_{\infty} S_b d$, one obtains

$$C_{\ell} = -\frac{2}{\pi} \sigma C_{N_{\alpha}} \frac{(b_0 - a)}{a^3 b_0} (1 - I_p) \frac{\dot{\phi} b_0}{U_{\infty}} \int_0^1 \int_0^1 \mathcal{R}^2(\eta) \Omega(\eta) C(\xi) S(\eta) d\xi d\eta \quad (43a)$$

where

$$\mathcal{R}(\eta) = a + (b_0 - a) \eta \quad (43b)$$

Taking the partial derivative of Eq. (43) with respect to p , where $p = \dot{\phi} b_0 / U_{\infty}$, and solving for I_p , one finally obtains

$$I_p = 1 + \frac{C_{\ell p}}{\frac{2}{\pi} \sigma \frac{(b_0 - a)}{a^3 b_0} C_{N_{\alpha}} \int_0^1 \int_0^1 \mathcal{R}^2(\eta) \Omega(\eta) C(\xi) S(\eta) d\xi d\eta} \quad (44)$$

$C_{\ell p}$ is computed from the results of Adams and Dugan (see Fig. 27). $C_{N_{\alpha}}$ is obtained by numerically differencing Eq. (35) for $\alpha_{\ell} \rightarrow 0$.

3. ROLL MOMENT

The above described body flow field and lifting theory will now be applied to the prediction of the roll moment produced by cruciform fins. If one desired, the present analysis could be applied in a straightforward manner to two or three fin configurations. Consider the missile at angle of attack

α_b , roll angle ϕ , and roll rate $\dot{\phi}$. The roll moment produced by a differential surface element on each of the four fins is

$$d\ell = q_\infty r \sum_{j=1}^4 C_{Nj} (U_j/U_\infty)^2 dx dr$$

where j refers to the j 'th fin and U_j is the magnitude of the velocity on the j 'th fin. Substituting C_N from Eq. (14) and integrating over the fin surfaces, one has

$$\ell = \sigma q_\infty \int_a^{b_o} \int_{x_{le}}^{x_{te}} r C(x, r) S(r) \sum_{j=1}^4 C_{Nj} (U_j/U_\infty)^2 dx dr$$

Transforming to fin coordinates (ξ, η) and nondimensionalizing by $q_\infty S_b d$, one obtains the roll moment coefficient

$$C_\ell = \frac{\sigma(b_o - a)}{2\pi a^3} \int_0^1 \int_0^1 \mathcal{R}(\eta) \Omega(\eta) C(\xi) S(\eta) \sum_{j=1}^4 C_{Nj} (U_j/U_\infty)^2 d\xi d\eta \quad (45)$$

where $\mathcal{R}(\eta)$ is given by Eq. (43b), $\Omega(\eta)$ is given by Eq. (20b), $C(\xi)$ is given by Eq. (19a), and $S(\eta)$ is given by Eq. (19b).

U_j is found by taking the magnitude of the local velocity given in Eq. (23):

$$U_j = \sqrt{U_\infty^2 \cos^2 \alpha_b + \left(v_{c_j} + \dot{\phi} r \sin \phi\right)^2 + \left(w_{c_j} - \dot{\phi} r \cos \phi\right)^2} \quad (46)$$

Note that if ϕ appears without the subscript j , as in the above equation, then the angle ϕ is measured from the y axis for the particular fin under consideration.

C_{N_j} depends upon the local effective angle of attack α_{ej} . To determine this angle the effective surface normal vector must be found taking into account control deflection and rolling motion interference. Using \vec{n} , from Eq. (22), the effective fin deflection angle δ_{ej} , from Eq. (37), and noting that the rolling motion interference affects the \vec{i} component of the normal vector, one can write*

$$\vec{n}_{ej} = \left[\sin(\Delta \delta_{ej}) + I_p \dot{\phi} r / U_\infty \right] \vec{i} - \cos(\delta_{ej}) \sin \phi \vec{j} + \cos(\delta_{ej}) \cos \phi \vec{k}$$

Substituting \vec{n}_e and \vec{V} into the equation for α_j , Eq. (21), one obtains the local effective angle of attack.

$$\begin{aligned} \alpha_{ej} = \sin^{-1} & \left[\left\{ U_\infty \cos \alpha_b \left[\sin(\Delta \delta_{ej}) + I_p \dot{\phi} r / U_\infty \right] \right. \right. \\ & - \left(v_{cj} + \dot{\phi} r \sin \phi \right) \cos(\delta_{ej}) \sin \phi \\ & \left. \left. + \left(w_{cj} - \dot{\phi} r \cos \phi \right) \cos(\delta_{ej}) \cos \phi \right\} / \left(|\vec{n}_{ej}| U_j \right) \right] \end{aligned} \quad (47)$$

where

$$|\vec{n}_{ej}| = 1 + 2 \sin(\Delta \delta_{ej}) I_p \dot{\phi} r / U_\infty + (I_p \dot{\phi} r / U_\infty)^2$$

*Ref. 10 accounted for rolling motion interference by way of \vec{j} and \vec{k} components of the velocity. That approach is not considered correct because it also changes the magnitude of the velocity. In fin - fin interference the magnitude of the approach velocity to the fin is not changed, but only the angle which it approaches the fin.

4. NORMAL FORCE AND PITCH MOMENT

The equations for the normal force and pitch moment produced by the fins will now be considered. The differential fin force in the z direction produced by the four fins is (see Fig. 28)*

$$\begin{aligned} dF_z = & dN_1 \cos \delta_1 \cos \phi_1 - dN_2 \cos \delta_2 \sin \phi_2 \\ & - dN_3 \cos \delta_3 \cos \phi_3 + dN_4 \cos \delta_4 \sin \phi_4 \end{aligned}$$

Writing the right side of this equation as a summation and substituting dN_j from Eq. (13), one obtains

$$dF_z = q_\infty \sum_{j=1}^4 C_{Nj} \left(U_j / U_\infty \right)^2 \cos \delta_j \cos \phi \, dx \, dr$$

Substituting in C_N from Eq. (14) and integrating over the surface of each fin, one has

$$F_z = \sigma q_\infty \int_a^b \int_{x_{le}}^{x_{te}} C(x, r) S(r) \sum_{j=1}^4 C_{Nj} \left(U_j / U_\infty \right)^2 \cos \delta_j \cos \phi \, dx \, dr$$

Transforming to fin coordinates (ξ, η) and nondimensionalizing by $q_\infty S_b$, one obtains the normal force coefficient due to the fins:

$$C_z = \frac{\sigma(b_o - a)}{\pi a^2} \int_0^1 \int_0^1 \Omega(\eta) C(\xi) S(\eta) \sum_{j=1}^4 C_{Nj} \left(U_j / U_\infty \right)^2 \cos \delta_j \cos \phi \, d\xi \, d\eta \quad (48)$$

*Note that the sign of dN_j is determined by its angular relationship to the surface normal vector, that is, positive dN_j is in the counter-clockwise sense.

The pitch moment produced by the fins is composed of two types of terms; the first term is due to the normal force just derived and the second term is due to the $\sin \delta_j$ component of the normal force on the fins (Fig. 28). The second term produces a pure moment, i.e., a couple, on the missile body and is usually much smaller in magnitude than the first term. The differential pitch moment due to both terms from all four fins is

$$\begin{aligned} dm = & -x dN_1 \cos \delta_1 \cos \phi_1 + r dN_1 \sin(\Delta \delta_1) \sin \phi_1 \\ & + x dN_2 \cos \delta_2 \sin \phi_2 + r dN_2 \sin(\Delta \delta_2) \cos \phi_2 \\ & + x dN_3 \cos \delta_3 \cos \phi_3 - r dN_3 \sin(\Delta \delta_3) \sin \phi_3 \\ & - x dN_4 \cos \delta_4 \sin \phi_4 - r dN_4 \sin(\Delta \delta_4) \cos \phi_4 \end{aligned}$$

Writing the right side of this equation as a summation and substituting dN_j from Eq. (13), one obtains

$$dm = -q_\infty \sum_{j=1}^4 C_{n_j} \left(U_j / U_\infty \right)^2 \left[x \cos \delta_j \cos \phi - r \sin(\Delta \delta_j) \sin \phi \right] dx dr$$

Substituting in C_n from Eq. (14) and integrating over the surface of each fin, one has

$$\begin{aligned} M = & -\sigma q_\infty \int_a^{b_0} \int_{x_{le}}^{x_{te}} C(x, r) S(r) \sum_{j=1}^4 C_{N_j} \left(U_j / U_\infty \right)^2 \left[x \cos \delta_j \cos \phi \right. \\ & \left. - r \sin(\Delta \delta_j) \sin \phi \right] dx dr \end{aligned}$$

Transforming to fin coordinates (ξ, η) and nondimensionalizing by $q_\infty S_b d$, one obtains the pitch moment coefficient due to the fins:

$$c_m = \frac{-\sigma(b_o - a)}{2 \pi a^3} \int_0^1 \int_0^1 \Omega(\eta) c(\xi) s(\eta) \sum_{j=1}^4 c_{N_j} (U_j/U_\infty)^2 \left[\mathcal{A}(\xi, \eta) \cdot \right. \quad (49)$$

$$\left. \cos \delta_j \cos \phi - \mathcal{R}(\eta) \sin(\Delta \delta_j) \sin \phi \right] d\xi d\eta$$

where

$$\mathcal{A}(\xi, \eta) = x_1 + c_r + (b_o - a) \tan \Lambda_{te} \eta - \Omega(\eta) \xi \quad (49b)$$

5. SIDE FORCE AND YAW MOMENT

The derivation of the side force and yaw moment is very similar to that of the normal force and pitch moment and, consequently, will not be given. The side force coefficient and the yaw moment coefficient are given by:

$$c_y = \frac{-\sigma(b_o - a)}{\pi a^2} \int_0^1 \int_0^1 \Omega(\eta) c(\xi) s(\eta) \sum_{j=1}^4 c_{N_j} (U_j/U_\infty)^2 \cos \delta_j \sin \phi d\xi d\eta \quad (50)$$

and

$$c_n = \frac{-\sigma(b_o - a)}{2 \pi a^3} \int_0^1 \int_0^1 \Omega(\eta) \sum_{j=1}^4 c_{N_j} (U_j/U_\infty)^2 \left[\mathcal{A}(\xi, \eta) \cdot \right. \quad (51)$$

$$\left. \cos \delta_j \sin \phi + \mathcal{R}(\eta) \sin(\Delta \delta_j) \cos \phi \right] d\xi d\eta$$

6. PANEL LOADS

The panel loads on the fin surfaces are essentially the same forces and moments derived previously (Sections II-3, II-4, and II-5), except that they are oriented in a fin coordinate system. Figure 29 shows the coordinate system and sign convention for the panel normal force N , the panel hinge

moment H , and the panel root bending moment B . The calculation of panel loads is useful for two reasons. First, they provide the most physically meaningful force and moments with which to compare theoretical predictions and experiment because they do not contain the geometry components of the roll angle and the fin deflection angle. Second, they directly provide the loads needed by the structural designer and the actuator torques needed by the guidance and control designer.

As the derivation of the panel loads is very similar to the previous derivations, the derivation will only be sketched very briefly. Using Eq. (13), the normal force on a fin panel due to a differential surface element is

$$dN = q_{\infty} C_n (U/U_{\infty})^2 dx dr$$

Proceeding as before, one obtains the panel normal force coefficient, $N/q_{\infty} S_f$;

$$C_p = \frac{\sigma(b_o - a)}{S_f} \int_0^1 \int_0^1 \Omega(\eta) C(\xi) S(\eta) C_N (U/U_{\infty})^2 d\xi d\eta \quad (52)$$

Recall that positive normal force points in the direction of the counterclockwise rotational sense.

The panel hinge moment due to a differential surface element is

$$dH = -q_{\infty} (x - x_h) C_n (U/U_{\infty})^2 dx dr$$

where x_h is the axial location of the reference line for the hinge moment. Proceeding as before, one obtains the panel hinge moment coefficient, $H/q_{\infty} C_r S_f$;

$$C_h = \frac{-\sigma(b_o - a)}{c_r S_f} \int_0^1 \int_0^1 [\mathcal{A}(\xi, \eta) - x_h] \Omega(\eta) C(\xi) S(\eta) C_N (U/U_\infty)^2 d\xi d\eta \quad (53)$$

The panel root bending moment due to a differential surface element is

$$dB = q_\infty (r-a) C_n (U/U_\infty)^2 dx dr$$

Proceeding as before, one obtains the panel root bending moment coefficient, $B/q_\infty(b_o - a)S_f$;

$$C_b = \frac{\sigma(b_o - a)}{S_f} \int_0^1 \int_0^1 \eta \Omega(\eta) C(\xi) S(\eta) C_N (U/U_\infty)^2 d\xi d\eta \quad (54)$$

SECTION III

RESULTS AND DISCUSSION

The results computed and presented in this investigation were dictated solely by the requirement to validate and determine the bounds of the present theory. Consequently, no results will be given without experimental measurements. The theory is evaluated by comparing predictions and measurements for six different fin planforms. The detailed geometry and reference are given in Table 1 and the planforms are shown Fig. 30. It can be seen that the aspect ratios range from 1.0 to 2.0 and the leading edge sweep angles range from 0° to 67.4° .

The results and comparison with experiment will be discussed in three sections: panel loads, roll moments, and control forces and moments. The panel loads to be presented are panel normal force, panel bending moment, and panel hinge moment. Normal force, pitch moment, side force, and yaw moment predictions could have been compared with experimental measurements but it is felt that the individual panel loads permit more physical insight into the aerodynamic generation of the forces and moments. Roll moment characteristics presented are the induced roll moment, roll damping moment, and steady state roll rate. These roll characteristics are of great importance in dynamic flight stability of finned missiles. Control deflection forces and moments to be presented are pitch (or yaw) control and roll control for various control deflections and roll angles.

1. PANEL LOADS

a. Panel Normal Force

The panel normal force on the windward fin, fin 4, as a function of roll angle for $\alpha_b = 20^\circ$ for configuration A at $M_\infty = .8$ is shown in Fig. 31.* Also shown in Fig. 31 is the prediction of Nielsen, Hemsch and Smith.⁷ As fin 4 sweeps from $\phi = 0^\circ$ to 90° it moves on the windward side of the body from the angle of attack plane to the x - y plane. As can be seen by comparing the present result with experiment, the present method predicts very accurately the load-up of the fin. Above $\phi = 60^\circ$ the present method predicts an increasing normal force, whereas experiment shows a slight drop in normal force. Examining the computer output for spanwise angle of attack and loading it is seen that as ϕ increases from zero the loading increases due to increase in local angle of attack across the span. At $\phi = 40^\circ$ the body upwash near the fin root has increased to the extent that the root chord stalls. As the roll angle increases further the stall location moves outboard, but the inboard sections begin to add lift as they progress further into post stall. Noting the experimental trend for $\phi > 40^\circ$ and the rise in normal force near $\phi = 80^\circ$ suggests the following explanation of the actual fin loading. The root chord stall is washed outboard due to the spanwise velocity component of the leading edge vortex. This, in turn, decreases the loading

*All panel loads calculated and compared with experimental data are for missile configuration A.

along the span such that the total loading decreases. But as the roll angle increases further and the spanwise location of stall moves outboard, the portion of unstalled span which could be affected steadily decreases. At $\phi = 90^\circ$ it is seen from the present computer results that stall occurs at the very tip of the fin, that is, the entire fin is in post-stall. Once this occurs the fin loading will then begin to increase again as the angle of attack increases. This hypothesis could be tested quantitatively by examining experimental spanwise pressure distributions on a fin. Qualitatively it could be tested by comparing predictions of the present method with experimental data for unswept fins and noting that this phenomenon probably would not occur for unswept geometries.

The panel normal force on the windward fin versus roll angle for $\alpha_b = 20^\circ$ at $M_\infty = 1.22$ is shown in Fig. 32. Good agreement between the present method and experiment is demonstrated in the figure. The trend in panel normal force for $\phi < 50^\circ$ is the same for supersonic flow as for the previous subsonic case. For $\phi > 50^\circ$, however, the experimental data shows that stall is delayed to a higher roll angle, i.e., angle of attack, as compared to $M_\infty = .8$. Figure 32 shows the experimental data still dropping at $\phi = 90^\circ$ which implies, from the previous discussion, that the stall angle of attack has not reached the trip chord. As the present method does not have any dependence of stall angle of attack on Mach number, Eq. (35), this characteristic is not demonstrated by theory.

The panel normal force on the leeward fin versus roll angle for $\alpha_b = 20^\circ$ at $M_\infty = .8$ is given in Fig. 33. Very good comparison between theory and experiment is demonstrated except near $\phi = 0^\circ$. As fin 1 rolls from $\phi = 0^\circ$ it begins to unload not only due to closer proximity to the angle of attack plane, but also immersion in the body vortex. The inboard portion of the fin unloads much more rapidly than the outboard portion because it is strongly influenced by the vortex feeding sheet. As the fin nears the center of the body vortex it produces essentially no net normal force. The portion inboard of the vortex produces negative force, i.e., in the negative roll moment direction, and the outboard portion produces an almost balancing positive force. This balance is highly dependent on the relation between the radial vortex location and the fin semispan. For example, if the fin had a smaller semispan then the zero load roll angle would be less than that shown in Fig. 33.

Figure 34 shows the same type of comparison as Fig. 33, except for $M_\infty = 1.22$. The agreement between theory and experiment is not as good as in the previous comparisons. Note that the experimental roll angle for zero cross-over loading decreased from $\phi = 75^\circ$ for $M_\infty = .8$ to $\phi = 60^\circ$ for $M_\infty = 1.22$. This could be caused by either, or both, the body vortex becoming stronger or the radial location of the vortex increasing. Recalling that the radial location of the vortex increases with Mach number, Eq. (11), one could infer

that vortex strength increases significantly with Mach number. This has been suggested by Nielsen in Ref. 26.

b. Panel Bending Moment

Figures 35 and 36 show the panel bending moment for the windward fin versus roll angle for $\alpha_b = 20^\circ$ at $M_\infty = .8$ and 1.22, respectively. Generally good agreement is demonstrated between theory and experiment. Good agreement between theory and experiment on the bending moment requires that both the magnitude of the total normal force, C_{p_4} , and spanwise pressure distribution be correct. Recall that the theory for panel normal force is in essentially perfect agreement with experiment (Figs. 31 and 32) for $\phi < 40^\circ$. Figures 35 and 36, however, show that the theory slightly underpredicts the bending moment for the same roll angle range. This implies that there is slightly more loading outboard and slightly less loading inboard than predicted by the present method. If bending moment data for other planforms indicated the same trend, then the spanwise normal force distribution, $S(\eta)$ given by Eq. (19b), could be modified slightly.

The root bending moment for the leeward fin versus roll angle for $\alpha_b = 20^\circ$ at $M_\infty = .8$ and 1.22 is shown in Figs. 37 and 38, respectively. Excellent agreement between theory and experiment is demonstrated for the subsonic case and fair agreement is shown for the supersonic case. It is interesting to note that for $M_\infty = .8$ near $\phi = 80^\circ$ the panel normal force is negative (Fig. 33) while the bending moment remains near zero (Fig. 37). The reason for this is that the reverse flow under

the vortex is strong enough to generate a net negative panel force, but the bending moment produced by the outboard positive normal force overcomes the negative bending moment produced by the inboard sections.

c. Panel Hinge Moment

The panel hinge moment for the windward fin versus roll angle for $\alpha_b = 20^\circ$ at $M_\infty = .8$ and 1.22 is shown in Figs. 39 and 40, respectively. The agreement between theory and experiment appears to be poor, particularly for $M_\infty = 1.22$. One must be cautioned, however, as to the sensitivity of the hinge moment to the location of the hinge line. A better indication of accuracy of the present method is obtained by a sample comparison of the theoretical and experimental axial location of the center of pressure of the fin. Using the hinge line, x_h , as the moment reference, one can write

$$x_{cp} C_p q_\infty S_f = H$$

Solving for the location of the center of pressure nondimensionalized by the root chord, one has

$$x_{cp}/c_r = c_h/c_p \quad (55)$$

Applying this equation to both the experimental and theoretical data at $\phi = 90^\circ$ for fin 4, one has

for $M_\infty = .8$	$\left(\frac{x_{cp}}{c_r}\right)_{\text{exp}} = .113$	$\left(\frac{x_{cp}}{c_r}\right)_{\text{theory}} = .023$
for $M_\infty = 1.22$	$\left(\frac{x_{cp}}{c_r}\right)_{\text{exp}} = .129$	$\left(\frac{x_{cp}}{c_r}\right)_{\text{theory}} = .024$

As can be seen by this calculation the experimental center of pressure is slightly farther aft of the hinge line than predicted by the theory. Taking the difference between each pair of ratios one sees that for the worst agreement between theory and experiment in Figs. 39 and 40, the predicted axial center of pressure is in error only 9.0% and 10.5% of the root chord for $M_\infty = .8$ and 1.22, respectively.

A second point should be made from the axial center of pressure calculation just presented. Note that the experimental data shows that the center of pressure moves slightly reward as the Mach number changes from subsonic to supersonic. This follows the usual trend of lifting surfaces in transonic flow. The predicted center of pressure, however, stays essentially constant with Mach number. The reason for this is that the assumed normal force distribution for uniform approach flow, Eqs. (19), do not depend upon Mach number. A slight improvement to the present theory would be to insert Mach number dependence in the chordwise distribution function, $C(\xi)$.

Figures 41 and 42 give the hinge moment for the leeward fin versus roll angle for $\alpha_b = 20^\circ$ at $M_\infty = .8$ and 1.22, respectively. Better agreement between theory and experiment is shown for the leeward fin than for the windward fin. This might be somewhat surprising because of the complexity of predicting fin loading for such a nonuniform approach flow. The reason, however, is that for $\phi > 50^\circ$ the panel normal force is small for the leeward fin so that the hinge moment is also small.

2. ROLL MOMENTS

a. Induced Roll Moment

Figures 43 and 44 show the induced roll moment versus angle of attack of the body for missile configuration A for $\phi = 20^\circ$ at $M_\infty = .8$ and $M_\infty = 1.22$, respectively. Also shown in the figures is the prediction of Nielsen, Hemsch and Smith.⁷ Fairly good agreement is observed between the present method and experiment for $M_\infty = .8$, but for $M_\infty = 1.22$ the agreement is poor. It should be noted that the induced roll moment is one of the most difficult nonlinear moments to predict as it is composed of the sum and difference of the first moment of four spanwise pressure distributions. The physical explanation of the slightly negative then rapidly increasing positive trend of the induced roll moment with angle of attack is very difficult to delineate because of the many complex aerodynamic phenomena embedded in the present theory. From numerical experiments with the theory, however, certain important elements can be identified. These are: radial location of the body vortex, size of the vortex core, and local stall and post-stall along the span of the fin.

To understand the trends plotted in Figs. 43 and 44 one must examine the spanwise loading of all the fins. Figure 45 shows the spanwise loading for each fin for $M_\infty = .8$. The loading at a given spanwise location shown in Fig. 45 is the integrated value over the local chord. The loading caused by the primary body vortex is clearly seen on fin 2. The spanwise location of the stall angle of attack can be

recognized as a slight drop in the normal force along fin 3. The loading on fins 1, 3, and 4 increases steadily as the root chord is approached due to body upwash and the increasing length of the chord. On fin 1 the loading drops sharply near the root chord because it passes inside the vortex feeding sheet. The roll moment produced by each fin loading shown is: fin 1, 0.794, fin 2, -0.031, fin 3, -0.751, and fin 4, 0.313. It can be seen that the roll moments produced by fin 1 and fin 3 roughly balance. Fin 2 and fin 4, however, do not balance because the reverse flow loading between the primary body vortex and the root chord on fin 2 drop (in magnitude) the roll moment on fin 2 to roughly zero. This results in a large net positive roll moment from fin 4. By similar reasoning, the small negative induced roll moment for small angles of attack is due to the increased outboard loading on fin 2 when the vortex is near the body surface.

Figure 46 gives the induced roll moment versus angle of attack for configuration B for $\phi = 22.5^\circ$ and $M_\infty = .7$. Theory and experiment are in very good agreement for the rectangular fin planform. Comparing the induced roll moment coefficient for the clipped delta and rectangular planform (Figs. 43 and 46) for $\alpha_b = 20^\circ$ it is seen that* $C_l = .325$ and $.186$, respectively. Recalling the previous explanation given concerning the origin of the large positive induced roll moment, one could ask why C_l for the shorter span rectangular planform is

* This comparison ignores the fact that the roll angle and Mach number are not exactly the same.

not larger than that for the clipped delta. The reason for the question would be that the reverse flow loading on fin 2 for the short span fin should produce a relatively larger positive roll moment than the clipped delta. The reasoning is correct; the paradox, however, is created by the nondimensionalization used in the present analysis and in almost all other analyses. The roll moment coefficient is based on the body cross-sectional area, not on the fin planform area. If one converts the two previous coefficients to coefficients based on fin planform area, one has $[C_l]_{S_f} = .347$ and $.487$, respectively. Now it is clear that the short span rectangular planform is much more efficient at producing an induced roll moment than the longer span clipped delta.

The induced roll moment versus angle of attack for configuration D for $\phi = 22.5^\circ$ and $M_\infty = .7$ and 1.2 is shown in Fig. 47. The theory reproduces the experimental data fairly well, but the change in induced roll moment with Mach number is not predicted accurately for this planform geometry. The reason is probably the effect of Mach number on the spanwise and chordwise pressure distribution $S(\eta)$ and $C(\xi)$, as mentioned earlier. Concerning the magnitude of the induced roll moment coefficient, a direct comparison can be made between the rectangular planform (Fig. 46) and the delta planform (Fig. 47) because they both have the same missile body and planform area. The delta planform produces a slightly smaller induced roll moment because

of the greatly different spanwise loading and stall angle of attack (compare, for example, Figs. 17 and 19).

b. Roll Damping Moment

Figure 48 shows the roll damping moment versus angle of attack for configuration E for $M_\infty = .22$. For angles of attack up to 12° here is excellent agreement between theory and experiment, but above that the theory agrees well with one set of experimental data and not the other. The only comment that can be made is that the experimental technique is greatly different between the two investigators. Clare³¹ used a roll oscillation technique and Regan²⁹ used the standard rolling speed decay method.

A comment should be made concerning the present numerical method of calculating derivatives such as C_{l_p} . As the missile fins rotate through a 90° roll cycle, while at nonzero angle of attack of the body, the forces and moments continually change. Therefore, one method of computing rolling motion derivatives is to numerically difference the average value of the force or moment coefficient over a roll cycle. That is

$$C_{l_p} = \frac{2}{\pi} \left[\int_0^{\pi/2} C_l \bigg|_{p=\Delta p} d\phi - \int_0^{\pi/2} C_l \bigg|_{p=0} d\phi \right] / \Delta p \quad (56)$$

where C_l represents any force or moment coefficient. This computation of C_{l_p} is appropriate for large values of rolling speed. The method described by Eq. (56) is one used in the present analysis. It should be mentioned, however, that

another method could be used. This method computes the difference between two values of the coefficient at different rolling speeds, but at the same roll angle. That is,

$$C_{i_p} \bigg|_{\phi=\phi_1} = \left[C_{i_p} \bigg|_{\phi=\phi_1, p=\Delta p} - C_{i_p} \bigg|_{\phi=\phi_1, p=0} \right] / \Delta p \quad (57)$$

This method should be used for very low rolling speeds, such as roll oscillations about a roll trim angle. This method would yield, for example, the roll angle variation of the roll damping moment while a missile is oscillating in roll lock-in.

Figure 49 gives the roll damping moment versus angle of attack for configuration F for $M_\infty = .6$ and 1.3. Although the slight drop in C_{l_p} near $\alpha_b = 17^\circ$ is not predicted, the agreement between theory and experiment is generally good over the angle of attack range. Comparing Figs. 48 and 49, it is seen that the trend of C_{l_p} with α_b is very different between the two planforms. One might suspect, based on the earlier discussion of induced roll moment, that this different character would be due primarily to the difference in semi-span between the two configurations. The roll damping moment for several fin planforms and semispans was computed in order to identify the dominant parameter causing the rapid decrease in C_{l_p} for α_b near 20° . It was found to be the stall angle of attack of the planform, and not fin span. For example, consider the case of holding the planform and span constant, say a rectangular planform of a given span, and varying the aspect ratio

so that the stall angle of attack varies. One finds that as the aspect ratio decreases (and the stall angle of attack increases) the drop in $C_{\ell p}$ at large angle of attack disappears.

c. Steady State Rolling Speed

The steady state roll rate of a missile whose fins are canted is calculated in a manner similar to $C_{\ell p}$. The steady state roll rate is defined as the rolling speed at which the roll driving moment balances with the roll damping moment. Therefore, the nondimensional steady state roll rate, p_{ss} , is the roll rate such that

$$\int_0^{\frac{\pi}{2}} [C_{\ell}]_{p=p_{ss}} d\phi = 0$$

Only one comparison of theory and experiment is made for steady state rolling speed because of the lack of data for other planforms. Figure 50 shows the steady state rolling speed vs angle of attack for configuration E for a fin cant of 4° (differential fin deflection) and $M_\infty = .23$. The theory slightly overpredicts p_{ss} for angles of attack less than 12° , but for $\alpha_b > 12^\circ$ the theory agrees perfectly with one set of data and underpredicts p_{ss} for the other set. The reason the theory predicts roll slowdown is rather difficult to determine. From numerical experiments with the present method it was found that roll slowdown was predicted for each of the planforms shown in Fig. 30. One qualitative comment that can be made, however, is that even though the roll damping moment decreases

at large angle of attack (Fig. 48), the roll driving moment, i.e., fin cant, decreases at a faster rate on every planform investigated.

3. CONTROL DEFLECTIONS

a. Pitch (or Yaw) Control

Pitch control force coefficient is defined to be the normal force coefficient of the entire missile configuration (body plus fins) with the fins deflected minus the normal force coefficient of the entire missile without the fins deflected. That is,

$$\Delta C_z = \left[C_{z_{B+f}} \right]_{\delta_j \neq 0} - \left[C_{z_{B+f}} \right]_{\delta_j = 0}$$

Using slender body theory notation, one can write

$$\Delta C_z = \left[C_{z_{B(f)}} \right]_{\delta_j \neq 0} + \left[C_{z_{f(B)}} \right]_{\delta_j \neq 0} - \left[C_{z_{B(f)}} \right]_{\delta_j = 0} - \left[C_{z_{f(B)}} \right]_{\delta_j = 0} \quad (55)$$

The second and fourth terms are computed in the present analysis, but the first and third are not. The first term can be segregated into two terms

$$\left[C_{z_{B(f)}} \right]_{\delta_j \neq 0} = \left[C_{z_{B(f)}} \right]_{\delta_j = 0} + C_{z_{B<\delta_j>}} \quad (56)$$

where the second term on the right side of the equation is the normal force coefficient of the body due to control deflection of the fins. Substituting Eq. (56) into Eq. (55), one has

$$\Delta C_z = C_{z_{B<\delta_j>}} + \left[C_{z_{f(B)}} \right]_{\delta_j \neq 0} - \left[C_{z_{f(B)}} \right]_{\delta_j = 0} \quad (57)$$

A simple result of slender body theory is used to estimate $C_{z_{B<\delta_j>}}$. Using the definition of the interference lift ratio, k_B , (see Ref. 24, pp. 213-218), one has

$$C_{z_{B<\delta_j>}} = k_B \left[C_{z_{f(B)}} \right]_{\delta_j \neq 0}$$

Substituting this into Eq. (57), one has

$$\Delta C_z = \left[1 + k_B \right] \left[C_{z_{f(B)}} \right]_{\delta_j \neq 0} - \left[C_{z_{f(B)}} \right]_{\delta_j = 0} \quad (58)$$

k_B calculated from slender body theory is derived assuming that the angle of attack of the body is zero. One could use Eq. (58) to calculate ΔC_z for any angle of attack and neglect the inconsistency between this and the derivation of k_B . The present analysis, however, chooses the approach of segregating the $\alpha_b = 0$ fin deflection interference and then using this constant value for nonzero α_b . Rewriting Eq. (58) according to this approach, we have

$$\Delta C_z = \left[C_{z_{f(B)}} \right]_{\delta_j \neq 0} - \left[C_{z_{f(B)}} \right]_{\delta_j = 0} + k_B \left[C_{z_{f(B)}} \right]_{\substack{\delta_j \neq 0 \\ \alpha_b = 0}} \quad (59)$$

Eq. (59) was used in the present analysis for computing pitch control forces with fin-body interference. k_B is a simple function of a/b_0 and is plotted in Fig. 51.

Figures 52, 53, and 54 show the pitch control force versus angle of attack for $M_\infty = .7$ and 1.2 for fin configurations B, C, and D, respectively. The control force shown in these figures is for $\phi = 0^\circ$ and the horizontal panels deflected 10° , that is, $\delta_1 = \delta_3 = 10^\circ$ and $\delta_2 = \delta_4 = 0^\circ$. The agreement between theory and experiment is generally fair for the three fin planforms and the angle of attack range. It can be seen from these three figures that the control force for $\alpha_b = 0^\circ$ for the three planforms is almost identical. Although the leading edge sweep angles are 0° , 38.7° , and 67.4° , respectively, all three planforms have the same aspect ratio; 1.67 . The trend with angle of attack is significantly different for the three planforms. For $\Lambda_{le} = 0^\circ$ (Fig. 52) the control force drops-off sharply with angle of attack; to the extent that for $15^\circ < \alpha_b < 20^\circ$ a positive control input produces a negative control force. Note that this phenomenon is not caused by the body vortex wake, but is caused by the interaction of the nonlinear normal force curve, i.e., fin stall, and body upwash. For $\Lambda_{le} = 38.7^\circ$ (Fig. 53), ΔC_z is nearly constant for low α_b and then drops-off with angle of attack. The experimental data for $M_\infty = .7$ shows a region of control force reversal near $\alpha_b = 17^\circ$. For $\Lambda_{le} = 67.4^\circ$ (Fig. 54), ΔC_z is almost constant out to $\alpha_b = 14^\circ$ and then shows a slight decrease with angle of attack. Also note the insensitivity of ΔC_z with Mach number. This is due to the low Mach number normal to the leading edge of the planform.

Figures 55, 56, and 57 show the pitch control force versus angle of attack for all panels deflected 10° ($\phi = 45^\circ$) for fin planforms B, C, and D, respectively. The agreement between theory

and experiment is generally fair for the three planforms over the angle of attack range. Similar trends of ΔC_z vs angle of attack are seen in Figs. 55, 56, and 57 as compared to Figs. 52, 53, and 54, respectively. For $\phi = 45^\circ$ and $\delta_j = 10^\circ$, however, no control reversals are seen over the angle of attack range. Also, the delta planform (Fig. 57) shows that the control effectiveness increases slightly with angle of attack up to $\alpha_b = 12^\circ$ for both Mach numbers.

b. Roll Control

Figures 58, 59, and 60 show the roll control moment versus angle of attack for $M_\infty = .7$ and 1.2 for fin configurations B, C, and D, respectively. These roll control moments are for $\phi = 0^\circ$ and $\delta_1 = -\delta_3 = 10^\circ$ and $\delta_2 = \delta_4 = 0^\circ$. The theory generally predicts larger roll control moments than experiment, but the theoretical trends with angle of attack are valid. For the rectangular and clipped delta planform (Figs. 58 and 59) a large region of roll control reversal occurs for $\alpha_b > 15^\circ$. This region is fairly well predicted by the present analysis. For the delta planform (Fig. 60) the theory substantially overpredicts the roll control moment up to $\alpha_b = 20^\circ$ and then a control reversal is predicted. The overprediction near $\alpha_b = 0^\circ$ could be due to an inaccurate spanwise loading or it could be due to a physical characteristic of control deflection not included in the present theory, that is, root chord gap. When a fin panel is deflected for control, a spanwise gap is created at the root chord of the fin. The gap size increases as the fin deflection and root chord length increases. For configuration D the root chord length is 100% longer and 50% longer, respectively, than configurations

B and C. This characteristic would decrease the predicted value of the roll control moment if it were included in the theory.

SECTION IV

SUMMARY, CONCLUSIONS, AND RECOMMENDATIONS

A method is described for predicting the forces and moments produced by fins attached to a missile. The body is assumed to be a circular cylinder with cruciform fins (or wings) as attached lifting surfaces. The method is applicable to speeds up through transonic flow as long as the fin leading edge is subsonic. The missile can have an arbitrary roll (or bank) angle and each fin can have arbitrary control deflection. The vortices shed from the body are assumed to be symmetric as they influence the loading on the fins.

Extensive comparisons are made between predicted results and experimental measurements. Included in the comparisons are: panel normal force, root bending moment, hinge moment, induced roll moment, roll damping moment, pitch control forces, and roll control moment. The force and moment predictions are compared with experimental data for six different fin geometries. Good agreement between predictions and experiment is obtained for panel forces and moments and roll moments for all of the fin planforms. Generally fair agreement is obtained for fin control forces and moments.

The following conclusions and recommendations are drawn from the present investigation.

1. The spanwise and chordwise pressure distributions are of sufficient accuracy to be used as an aid in estimating root bending and hinge moment structural

loads. The hinge moment predictions can also be used as a design aid in sizing control deflection actuators.

2. Evidence was found to suggest that stall near the root chord on highly swept fins washes outboard and, consequently, decreases the outboard loading on the fin. Although this element is not in the present theory, one might conceive of a method of approximating this phenomenon in the analysis.
3. Certain comparisons between theory and experiment suggest that the stall angle of attack increases with Mach number. If sufficient data could be gathered on this trend, it should be added to the analysis.
4. The results of the present method could be enhanced by improving the empirical data for the body flow field model or by using a more accurate body flow field model. An improved flow model should contain more compressibility effects.
5. In general, short span fins produce larger nonlinear forces and moments, such as induced side force and induced roll moment, than larger span fins. This typically occurs even though the exposed fin area is smaller.
6. The present method could be improved by requiring the basic chordwise and spanwise pressure distributions to be dependent on freestream Mach number. This should be done after sufficient pressure distribution data on wing along planforms was available for various Mach numbers.
7. The nonlinear decrease in roll damping moment for large angles of attack was found to be due to the stall angle of attack

of the fin. The stall angle is primarily determined by the aspect ratio and leading edge sweep.

8. The present method should be coupled to a body force and moment predictive method so that complete missile force and moment predictions are available.
9. The rapid decrease in pitch control force at large angles of attack is predicted by the method.
10. Predicted roll control reversal at large angles of attack generally agrees with experimental data.
11. The present method should prove to be a valuable tool for missile designers because of its ability to address general fin planforms.

REFERENCES

1. Mello, J. F. and Sivier, K. R., "Supersonic Induced Rolling-Moment Characteristics of Cruciform Wing Body Configuration at High Angles of Attack," Aerospace Engineering, Vol. 20, No. 7, July 1961, pp. 20-21, 44-51.
2. Oberkampf, W. L. and Nicolaides, J. D., "Aerodynamics of Finned Missiles at High Angle of Attack," AIAA Journal, Vol 9, No. 12, Dec. 1971, pp. 2378-2384.
3. Oberkampf, W. L., "Prediction of Roll Moments on Finned Bodies in Supersonic Flow," J. of Spacecraft and Rockets, Vol. 12, No. 1, Jan. 1975, pp. 17-21.
4. Dillenius, M. F. E. and Nielsen, J. N., "Prediction of Aerodynamics of Missiles at High Angles of Attack in Supersonic Flow," NEAR TR 99, Oct. 1975.
5. Mendenhall, M. R. and Nielsen, J. N. "Effect of Symmetrical Vortex Shedding on the Longitudinal Aerodynamic Characteristics of Wing-Body-Tail Combinations," NEAR TR 69, NASA-CR-2473, Jan. 1975.
6. Spangler, S. B. and Mendenhall, M. R., "Further Studies of Aerodynamic Loads at Spin Entry," NEAR TR 141, July 1977.
7. Nielsen, J. N., Hemsch, M. J., and Smith, C. A., "A Preliminary Method for Calculating the Aerodynamic Characteristics of Cruciform Missiles to High Angles of Attack Including Effects of Roll Angle and Control Deflections," NEAR TR 152, Nov. 1977.
8. Marshall, F. J. and Deffenbaugh, F. D., "Separated Flow Over a Body of Revolution," J. of Aircraft, Vol. 12, No. 2, Feb. 1975, pp. 78-85.

9. Deffenbaugh, F. D. and Koerner, W. G., "Asymmetric Vortex Wake Development on Missiles at High Angles of Attack," J. Spacecraft, Vol. 12 No. 3, March 1977, pp. 155-162.
10. Oberkampf, W. L., "Aerodynamics of Finned Missiles at High Angle of Attack," Ph.D. dissertation, Aug. 1970, Univ. of Notre Dame, Notre Dame, Ind.
11. Oberkampf, W. L., and Bartel, T. J. "Supersonic Flow Measurements in the Body Vortex Wake of an Ogive Nose Cylinder," AFATL-TR-78-127, Air Force Armament Lab., Nov. 1978.
12. Grosche, F. R., "Wind Tunnel Investigation of the Vortex System Near and Inclined Body of Revolution With and Without Wings," AGARD-CP-71-71, Aerodynamic Interference, Jan. 1971.
13. Tinling, B. E. and Allen, C. Q., "An Investigation of the Normal Force and Vortex Wake Characteristics of an Ogive Nose Cylinder," NASA-TN-D-1297, Apr. 1962.
14. Fidler, J. E., Nielsen, J. N., and Schwind, R. G., "An Investigation of Slender-Body Wake Vortices," AIAA 15th Aerospace Sciences Meeting, Paper No. 77-7, Jan. 1977.
15. Winter, H., "Flow Phenomena on Plates and Airfoils of Short Span," Verein Deutscher Ingenieure, Special Issue (Aviation) 1936 (English translation, NACA-TM-798, July, 1936.)
16. Bartlett, G. E. and Vidal, R. J., "Experimental Investigation of Influence of Edge Shape on the Aerodynamic Characteristics of Low Aspect Ratio Wings at Low Speeds," Journal of the Aeronautical Sciences, Vol. 22, No. 8, Aug. 1955, pp. 517-533.

17. Marsden, D. J. Simpson, R. W., and Rainbird, W. J., "An Investigation Into the Flow Over Delta Wings at Low Speeds With Leading Edge Separation," College of Aeronautics, Cranfield, Rept. No. 114, Feb. 1958.
18. Hummel D., "Zur Umstromung Scharfkantiger Schlander Deltaflugel bei Grossen Anstellwinkeln," Z. Flugwiss, Vol. 15, No. 10, 1967.
19. Wickens, R. H., "The Vortex Wake and Aerodynamic Load Distribution of Slender Rectangular Wings," Canadian Aeronautics and Space J., Vol. 13, June 1967, pp. 247-260.
20. Lecat, R. and Rietschlin, J., "Goniometric Aerodynamics: A Different Perspective: Description-Application, AIAA Atmospheric Flight Mechanics Conference, Paper No. 79-1650, Aug. 1979.
21. Polhamus, E. C., "A Concept of the Vortex Lift of Sharp-Edge Delta Wings Based on a Leading Edge Suction Analogy," NASA TN-D-3767, Dec. 1966.
22. Wentz, W. H. and Kohlman, D. L., "Wind Tunnel Investigations of Vortex Breakdown on Slender Sharp-Edged Wings," NASA-CR-98737, 1968.
23. Johnson, J. L., "Low-Speed Measurements of Static Stability, Damping in Yaw, and Damping in Roll of a Delta, A Swept, and an Unswept Wing for Angles of Attack from 0° to 90° ," NACA-RM-L56B01, April 1956.
24. Nielsen, J. N., Missile Aerodynamics, McGraw-Hill, 1960.

25. Adams, G. J., and Dugan, D. W., "Theoretical Damping in Roll and Rolling Moment Due to Differential Wing Incidence for Slender Cruciform Wings and Wing-Body Combinations," NACA Report 1088, Sept. 1950.
26. Nielsen, J. N., "Nonlinearities in Missile Aerodynamics," AIAA 16th Aerospace Sciences Meeting, AIAA Paper No. 78-20, Jan. 1978.
27. Allen, C. Q., Schwind, R. G., and Malcolm, G. N., "Canard-Body-Tail Missile Test at Angles of Attack to 50° in the Ames 11-Foot Transonic Wind Tunnel," NASA-TM-78441, Sept. 1978.
28. Frantz, G. E., "Control Surface Interaction Study: Wind Tunnel Test Data Analysis Report," North American Aviation Rept. No. NA66H-139, Feb. 1966.
29. Regan, F. J., "Roll Damping Moment Measurements for the Basic Finner at Subsonic and Supersonic Speeds," Rept. 6652, March 1964, Naval Ordnance Lab., White Oak, Md.
30. Jenke, L. M., "Experimental Roll-Damping Magnus, and Static-Stability Characteristics of Two Slender Missile Configurations at High Angles of Attack (0 to 90 deg) and Mach Numbers 0.2 through 2.5," AEDC-TR-58, July 1976.
31. Clare, T. A., "Non-Linear Resonance Instability in the Flight Dynamics of Missiles," Ph.D. Dissertation, Univ. of Notre Dame, Notre Dame, Ind., June, 1970.
32. Hensch, M. J. and Nielsen, J. N., "Test Report for Canard Missile Tests in Ames 6- by 6-Foot Supersonic Wind Tunnel," NEAR TR 72, August 1974.
33. Startzell, D. E. and De Meritte, F. J., "Effect of Fin Cant and Nose Shapes on Free Spin of Basic Spinner," NAVORD Rept. 6025, 1958.

TABLE 1. GEOMETRY OF MISSILES USED FOR COMPARISON OF THEORY

Configuration	AND EXPERIMENT						
	b_0/a	c_r/a	x_1/a	Λ_{te}	Λ_{te}	x_h/a	A_e
A	2.4	2.8	17.2	45°	0°	18.4	1.33
B	2	1.2	18.1	0°	0°	--	1.67
C	2	1.6	17.7	38.7°	0°	--	1.67
D	2	2.4	16.9	67.4°	0°	--	1.67
E	3	2	18.0	0°	0°	--	2.00
F	2	2.66	17.34	53.1°	0°	--	1.00
							Reference
							27
							28
							28
							28
							10,29
							30

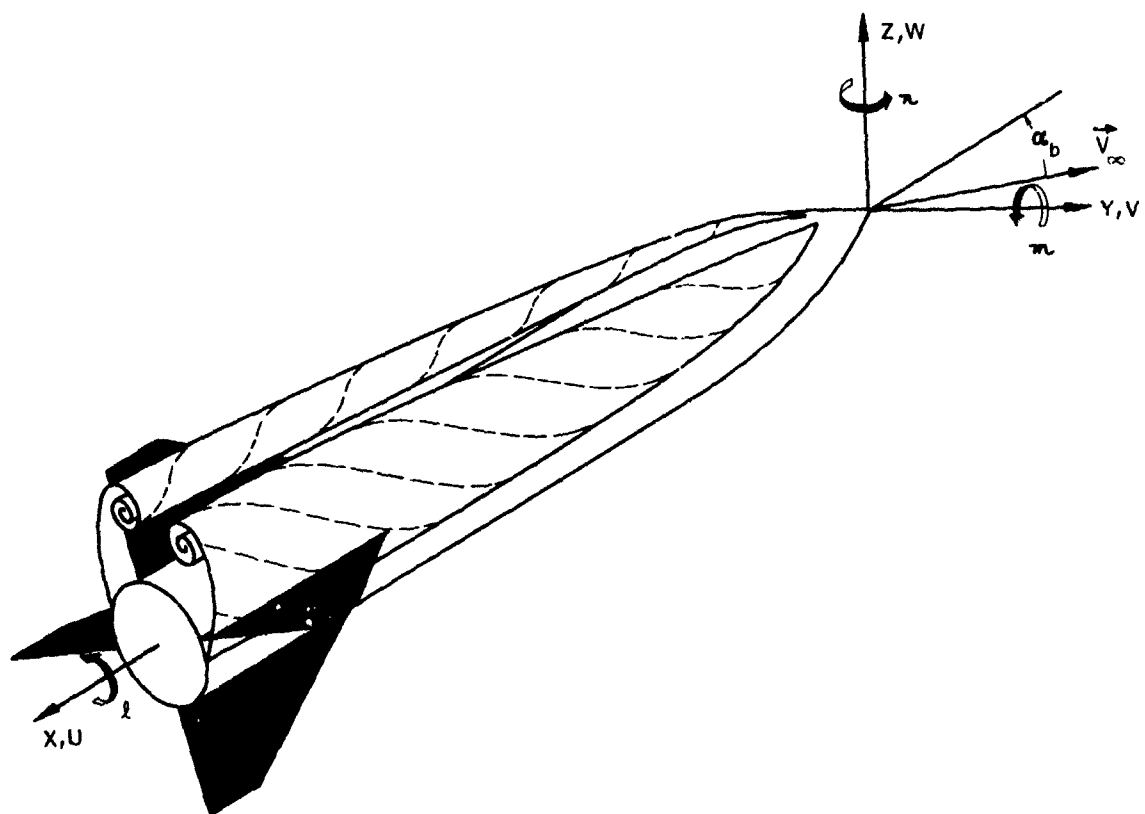


Figure 1. Coordinate System and Schematic of Body Vortices

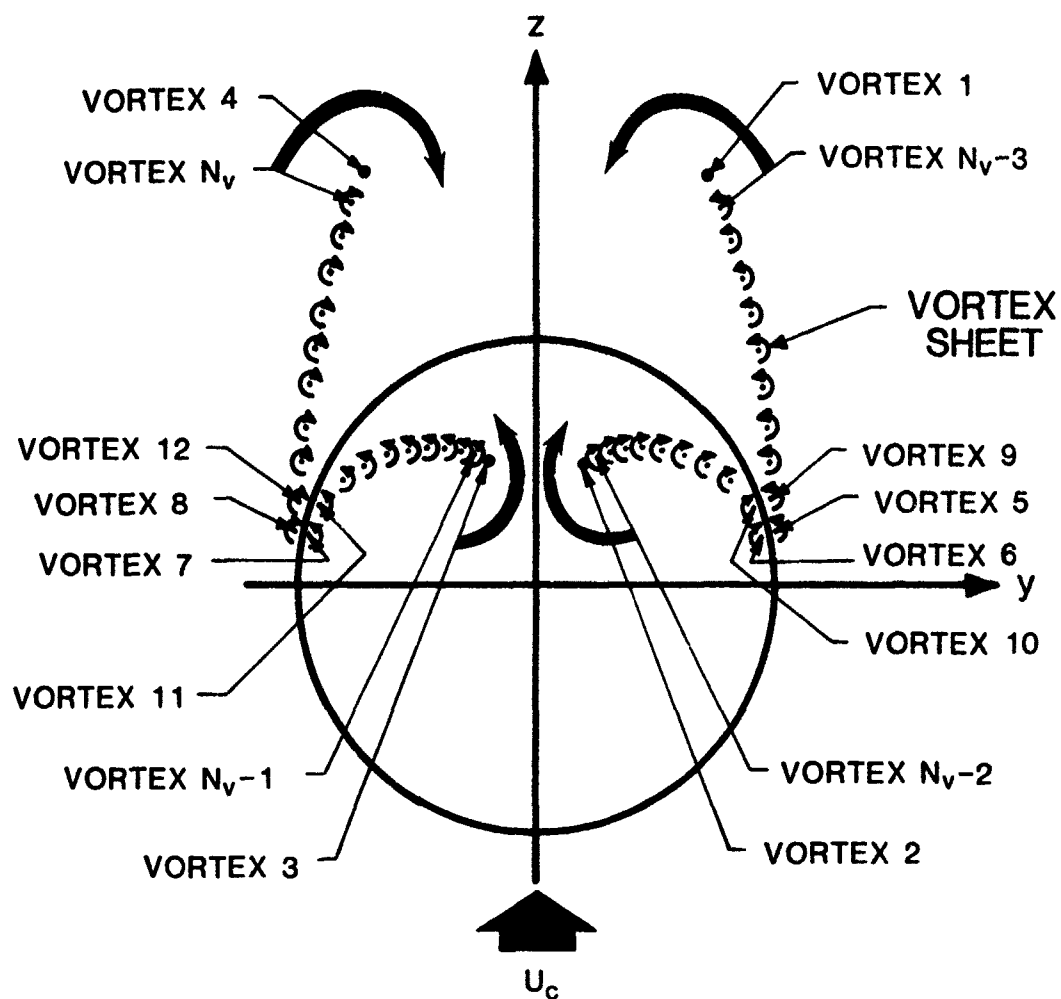


Figure 2. Cross-Flow Plane Flow Model

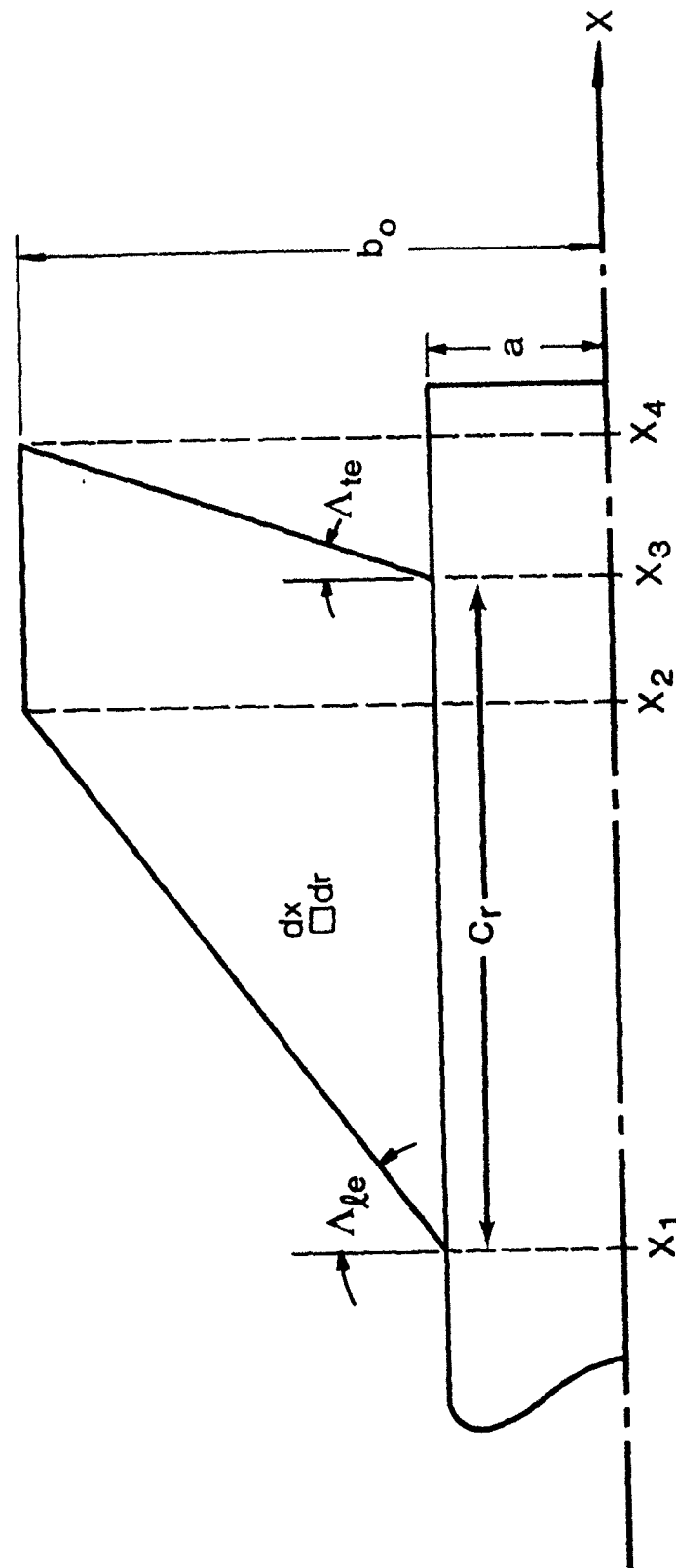


Figure 3. General Planform Fin

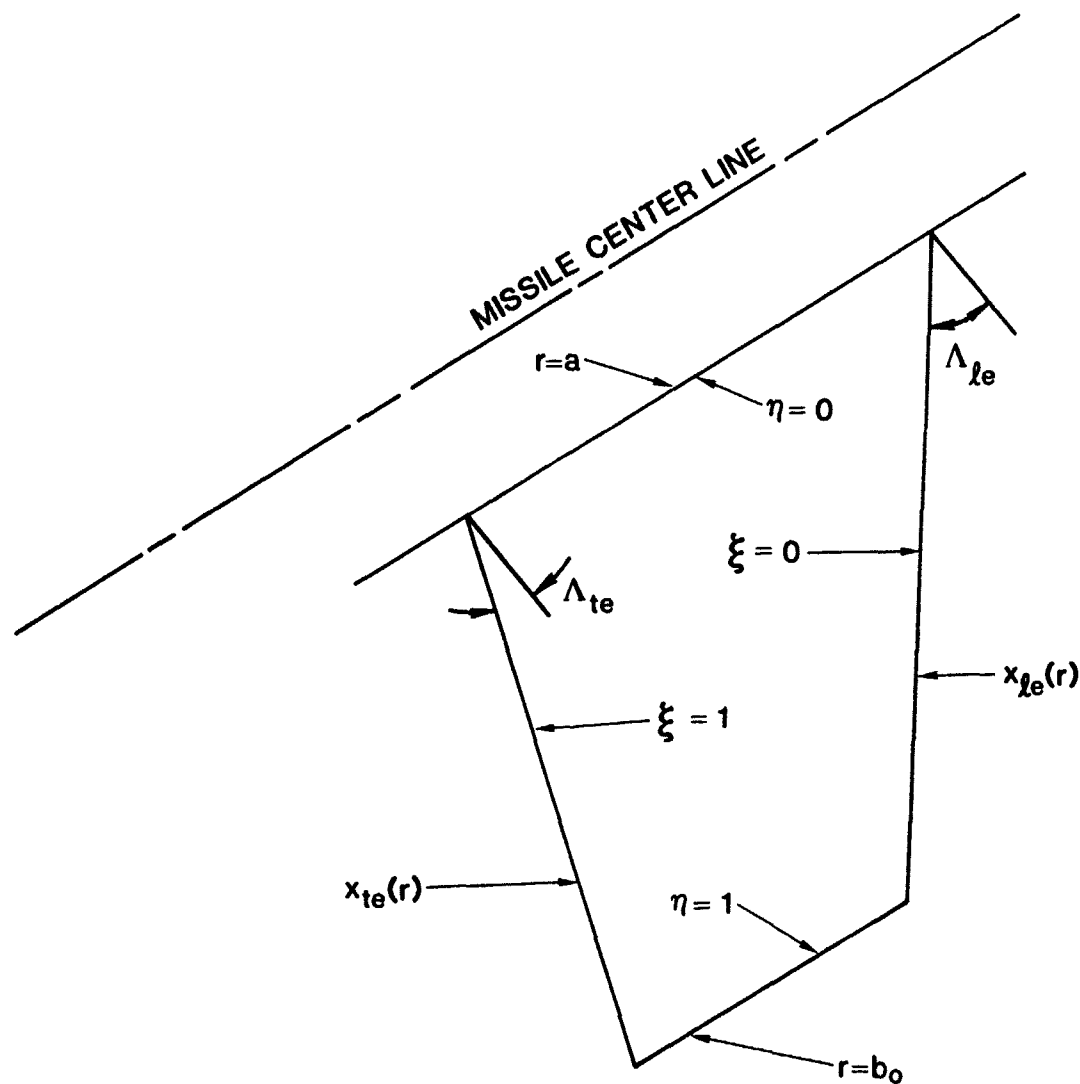
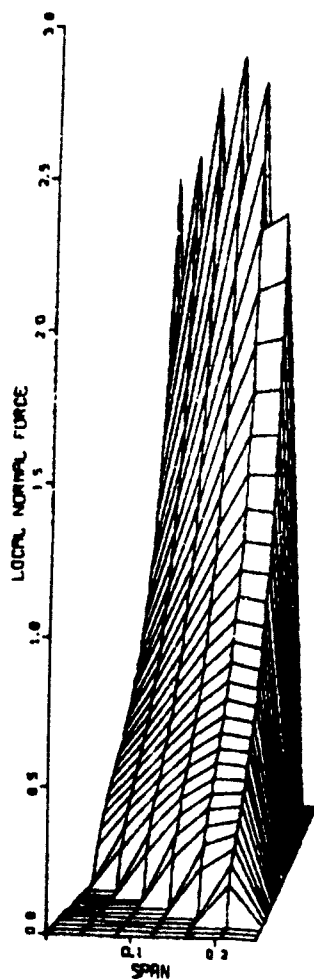
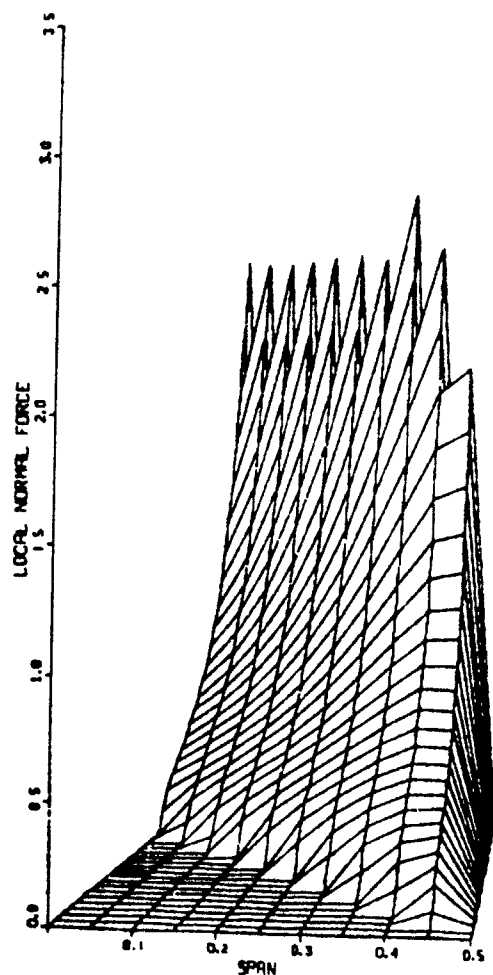


Figure 4. Fin Oriented Coordinates ξ, η

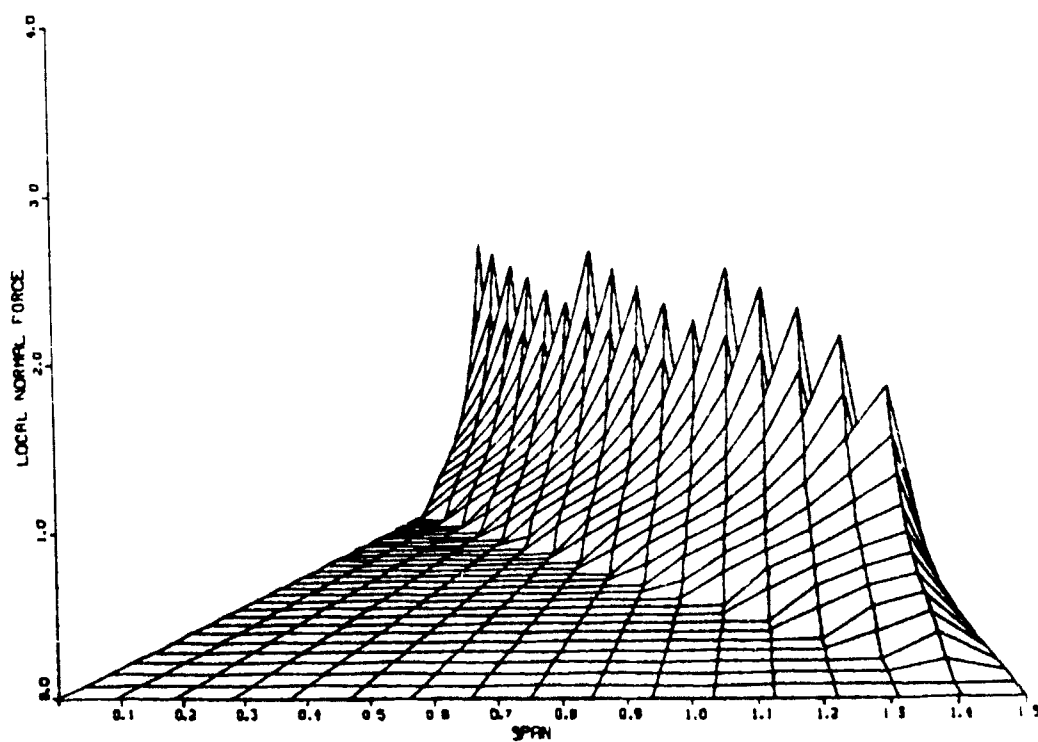


a) $A_e = .5$



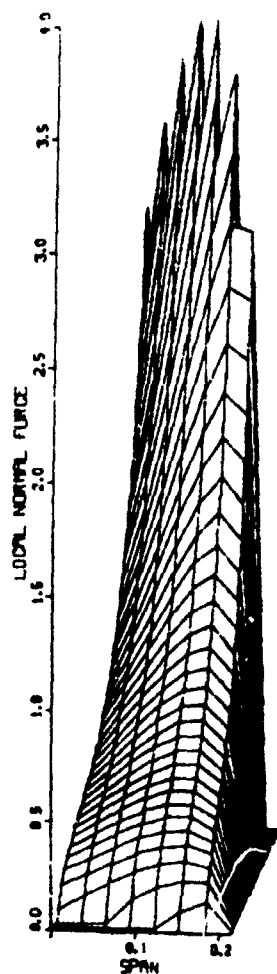
b) $A_e = 1.$

Figure 5. Normal Force Distribution Over Fin Surface
for $\Lambda_{le} = \Lambda_{te} = 60^\circ$

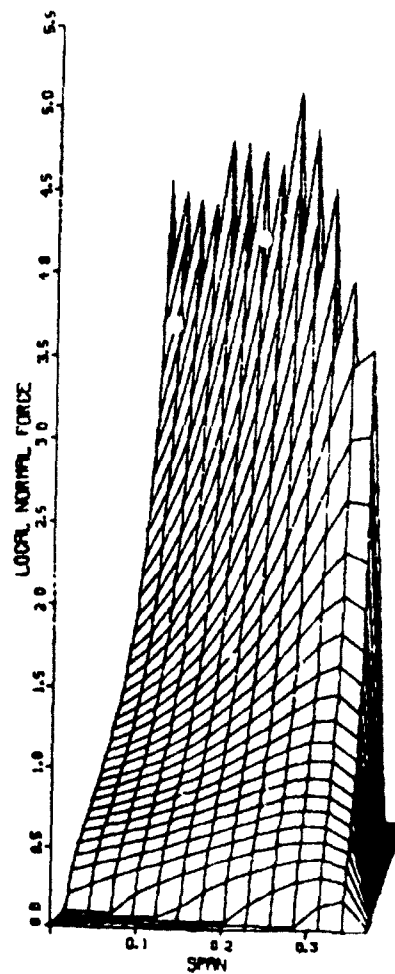


c) $A_e = 3.$

Figure 5. Normal Force Distribution Over Fin Surface
for $\Lambda_{fe} = \Lambda_{te} = 60^\circ$ (concluded)

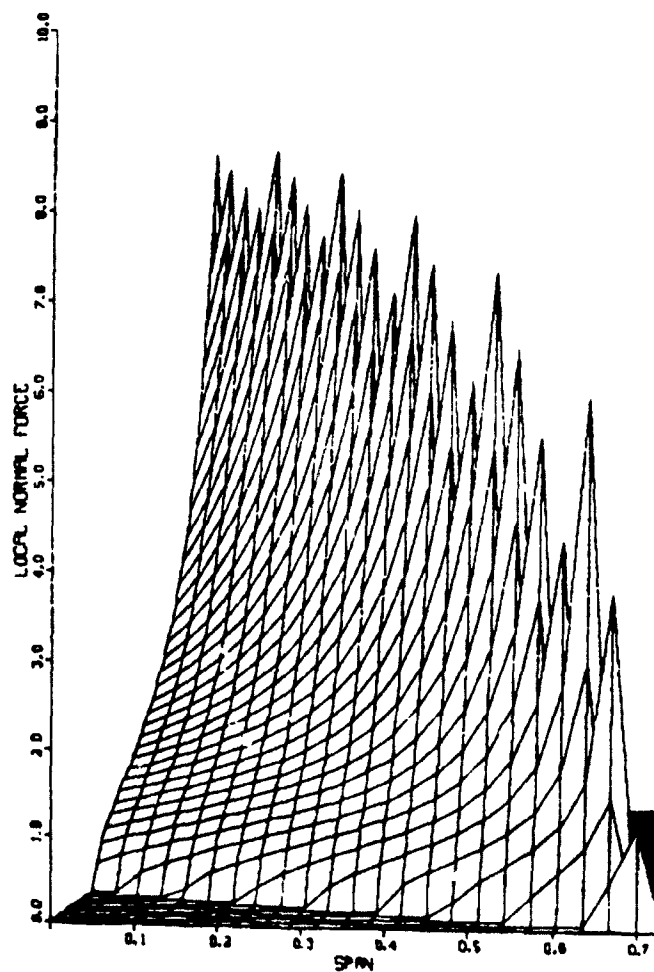


a) $A_e = .5$



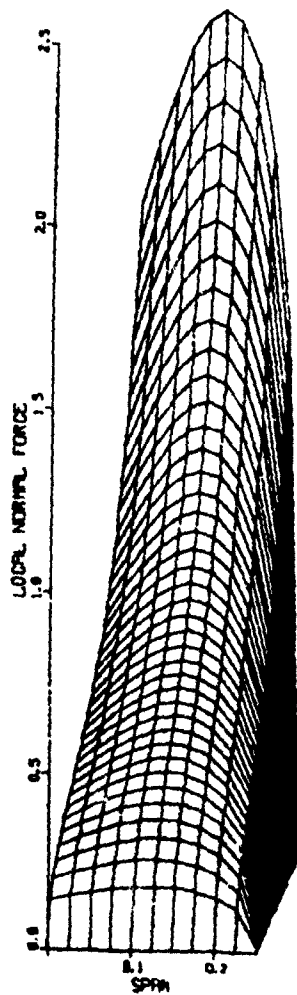
b) $A_e = 1.$

Figure 6. Normal Force Distribution Over Fin Surface
for $\Lambda_{fe} = 60^\circ$ and $\Lambda_{te} = 20^\circ$

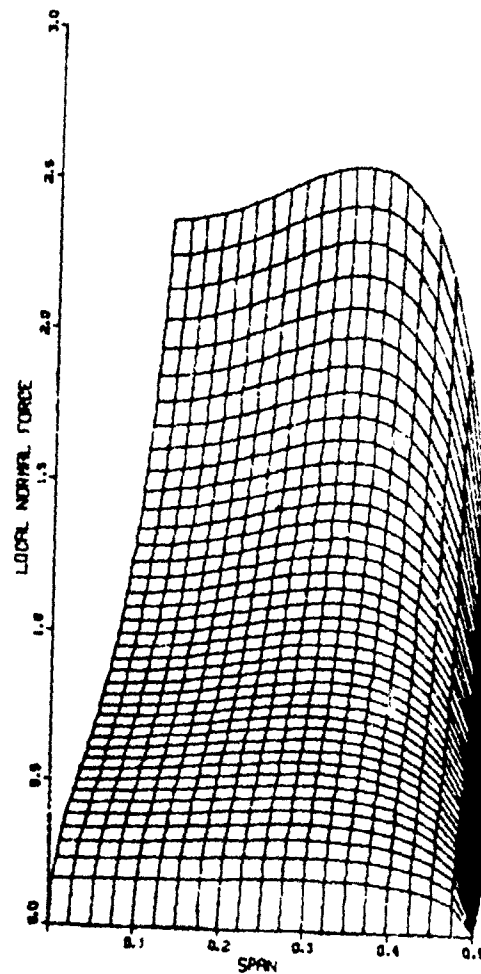


c) $A_e = 2.92$

Figure 6. Normal Force Distribution Over Fin Surface
for $\Lambda_{le} = 60^\circ$ and $\Lambda_{te} = 20^\circ$ (concluded)

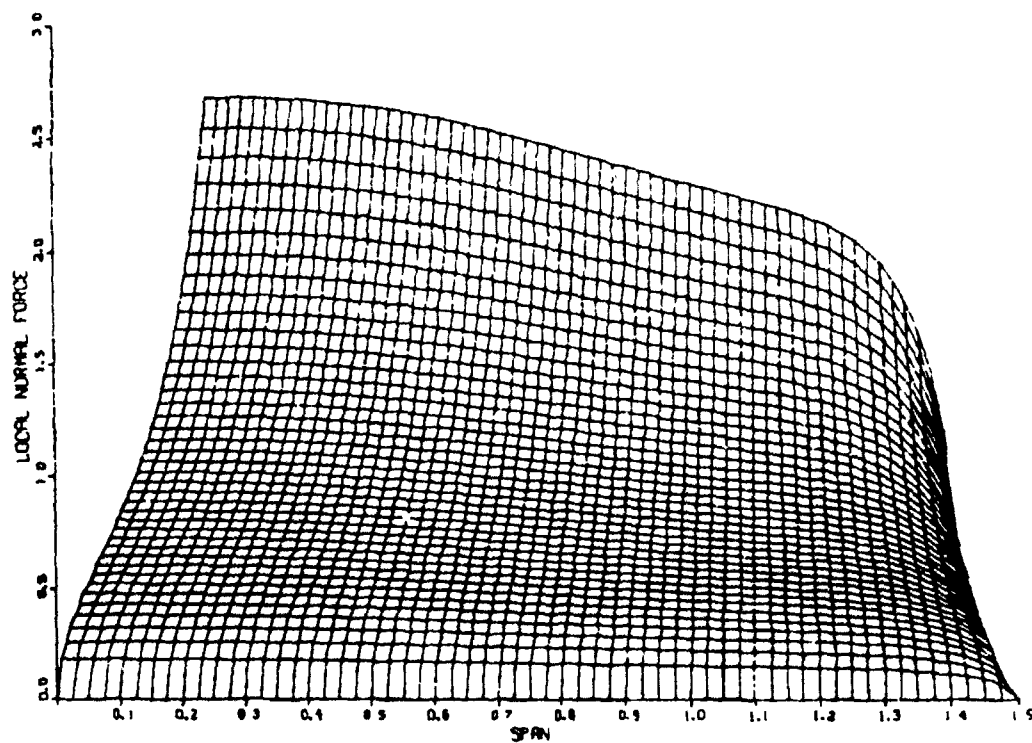


a) $A_e = .5$



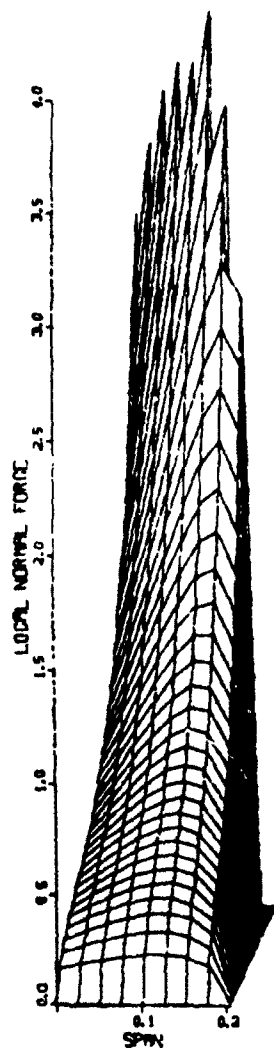
b) $A_e = 1$

Figure 7. Normal Force Distribution Over Fin Surface
for $\Lambda_{le} = \Lambda_{te} = 0^\circ$

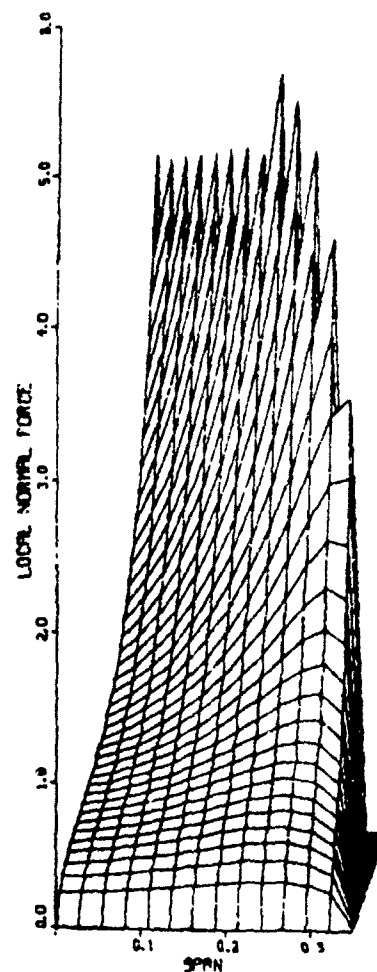


c) $A_e = 3.$

Figure 7. Normal Force Distribution Over Fin Surface
for $\Lambda_{le} = \Lambda_{te} = 0^\circ$ (concluded)

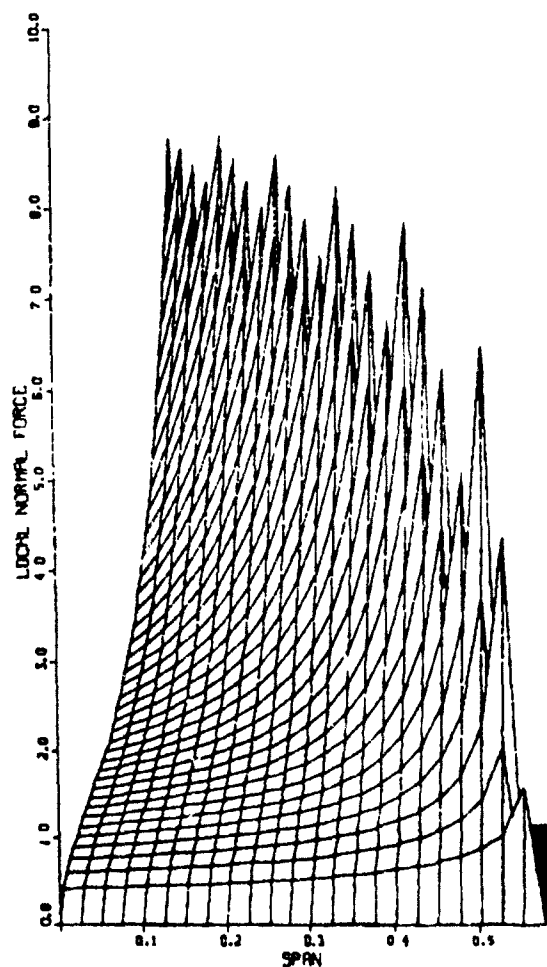


a) $A_e = .5$



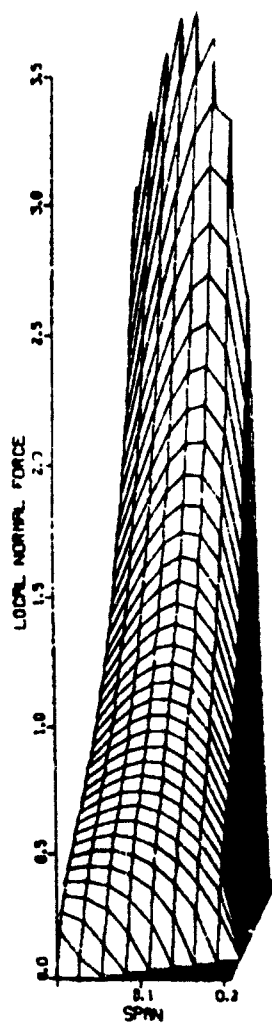
b) $A_e = 1.$

Figure 8. Normal Force Distribution Over Fin Surface
for $\Lambda_{le} = 60^\circ$ and $\Lambda_{te} = 0^\circ$

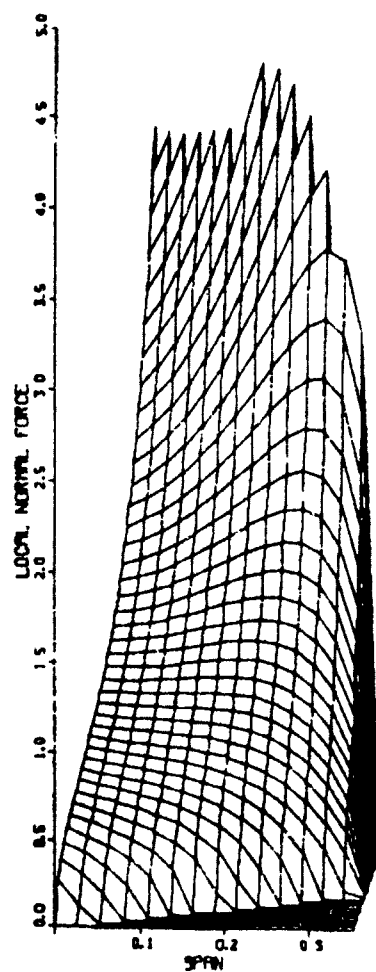


c) $A_e = 2.31$

Figure 8. Normal Force Distribution Over Fin Surface
for $\Lambda_{fe} = 60^\circ$ and $\Lambda_{te} = 0^\circ$ (concluded)

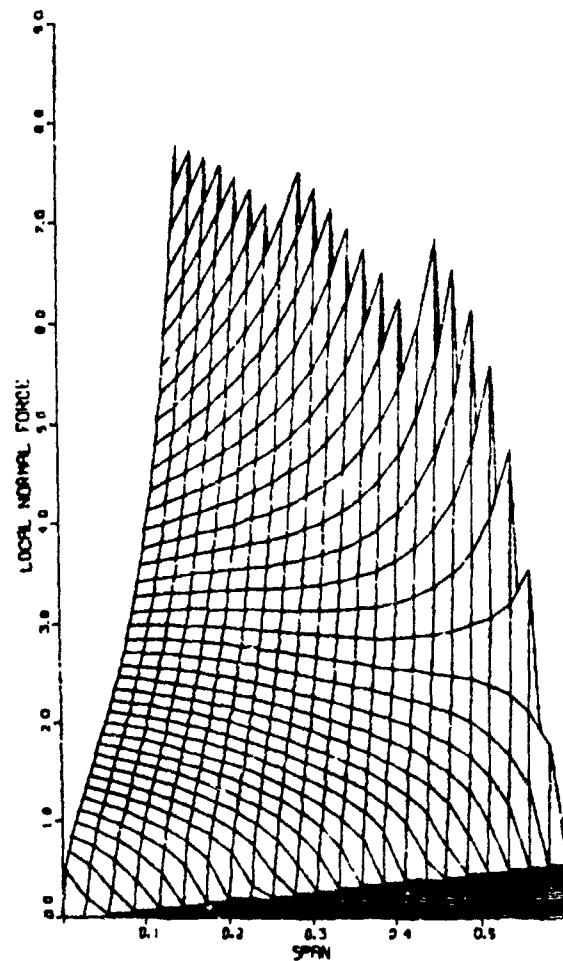


a) $A_e = .5$



b) $A_e = 1.$

Figure 9. Normal Force Distribution Over Fin Surface
for $\Lambda_{fe} = 40^\circ$ and $\Lambda_{te} = -40^\circ$



c) $A_e = 2.38$

Figure 9. Normal Force Distribution Over Fin Surface
for $\Lambda_{le} = 40^\circ$ and $\Lambda_{te} = -40^\circ$ (concluded)

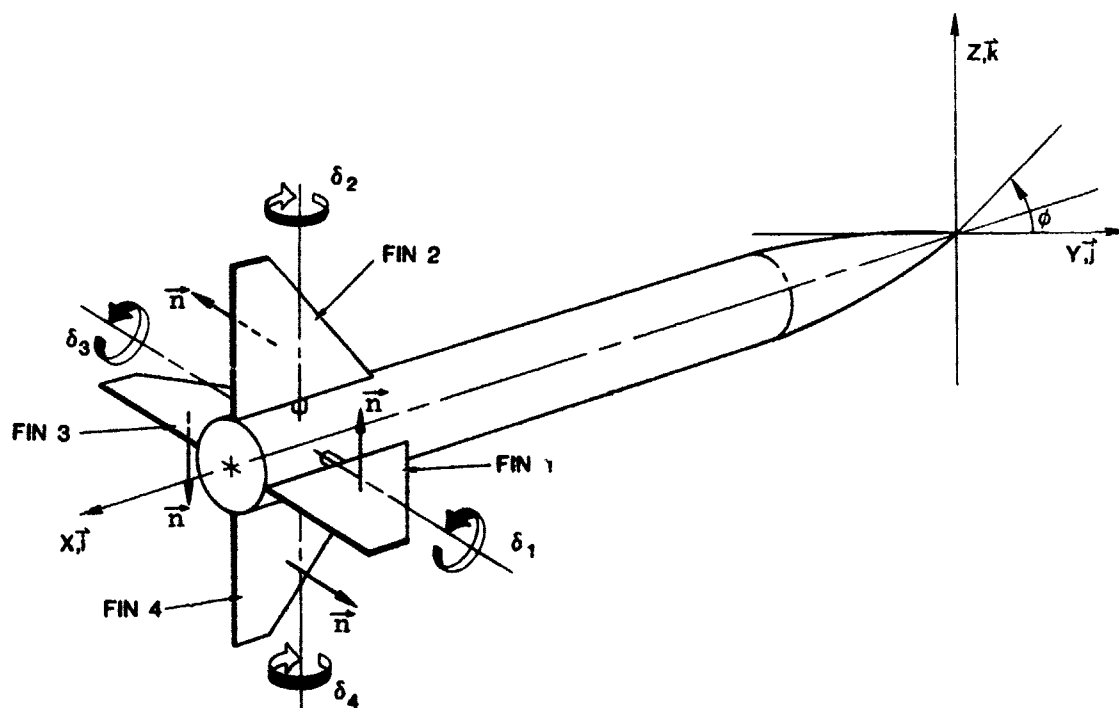


Figure 10. Surface Normal Vector and Sign Convention for Fin Control Deflection

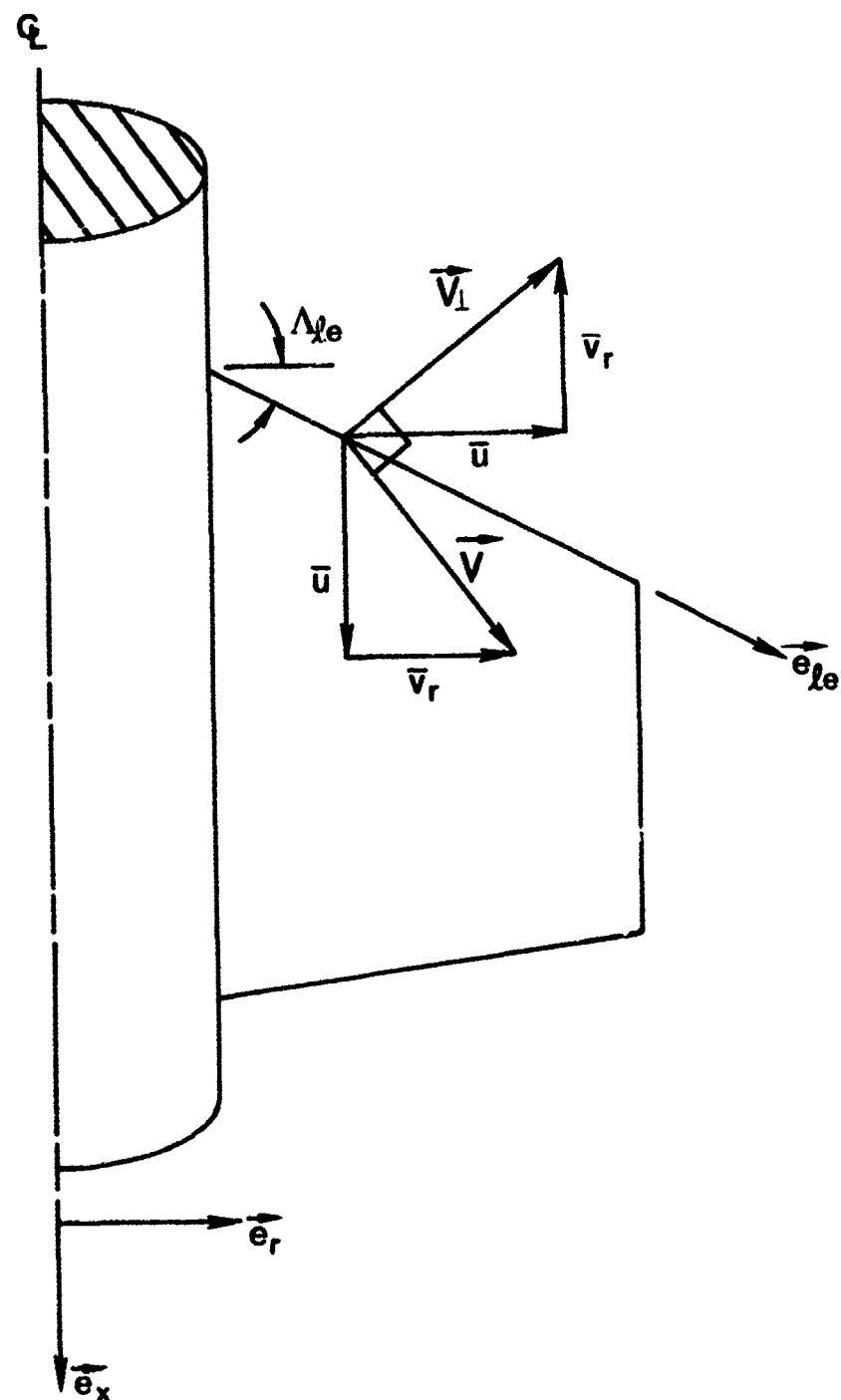


Figure 11. Fin Surface Cylindrical Coordinates

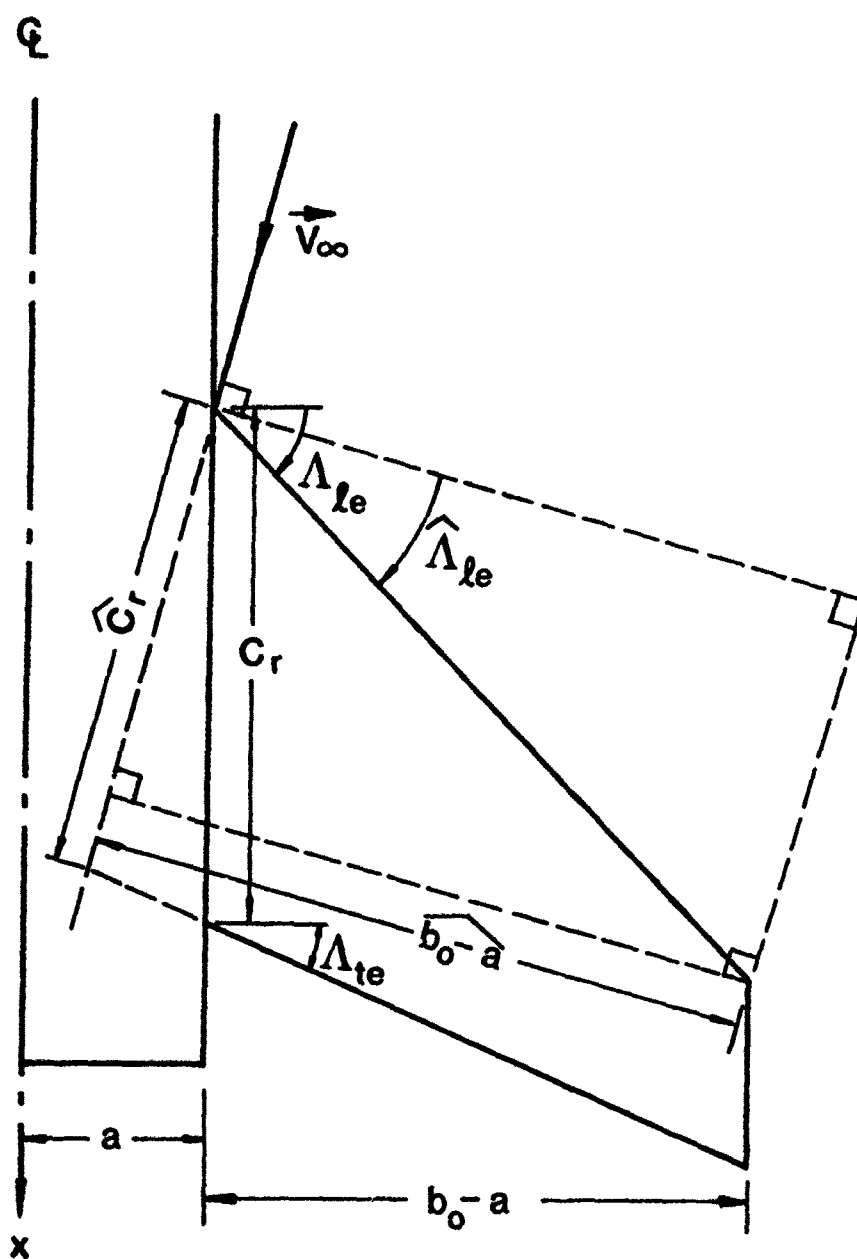


Figure 12. Geometry For Determining Effective Aspect Ratio

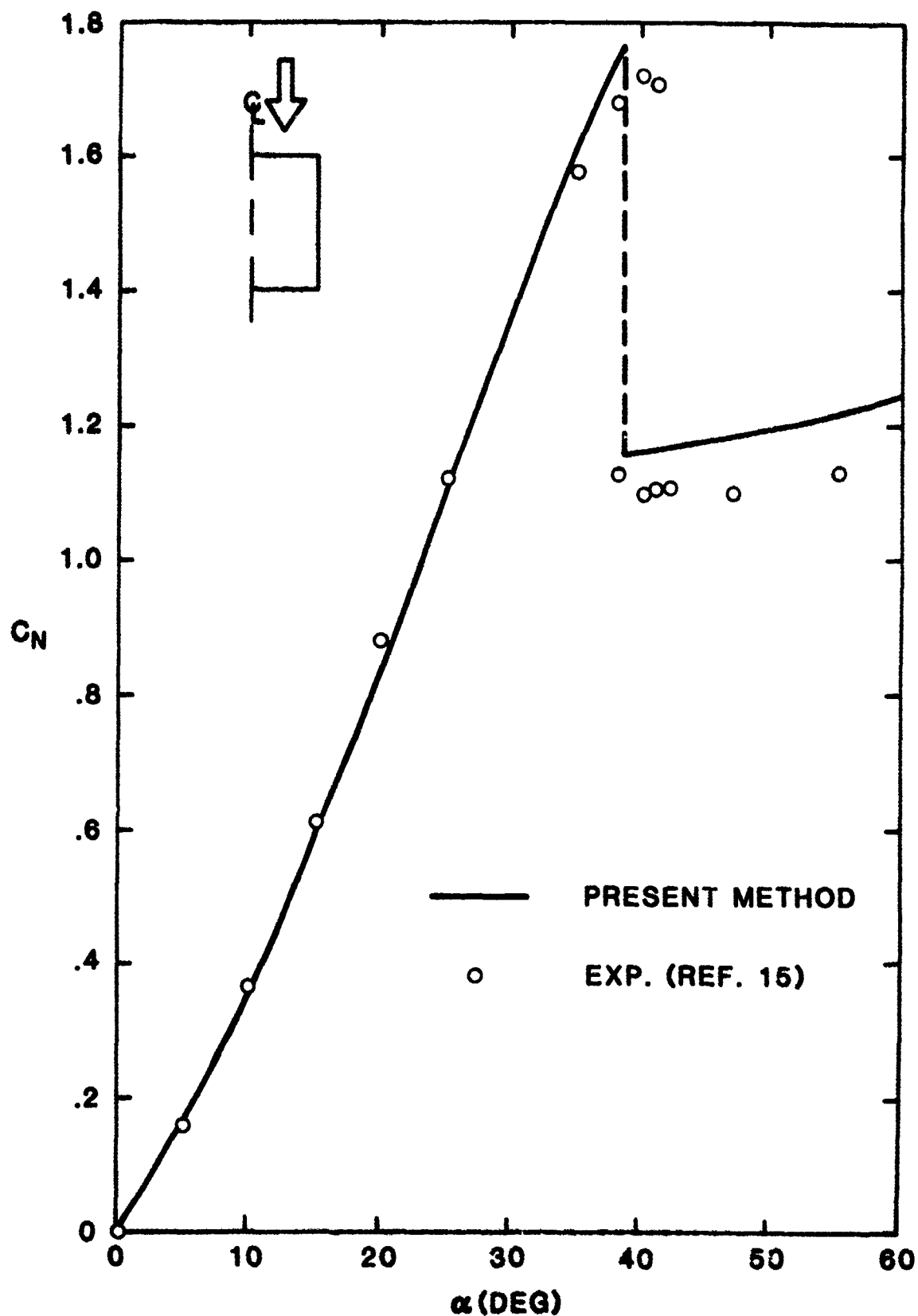


Figure 13. Normal Force Coefficient vs α for Rectangular Planform ($A_e = 1$)

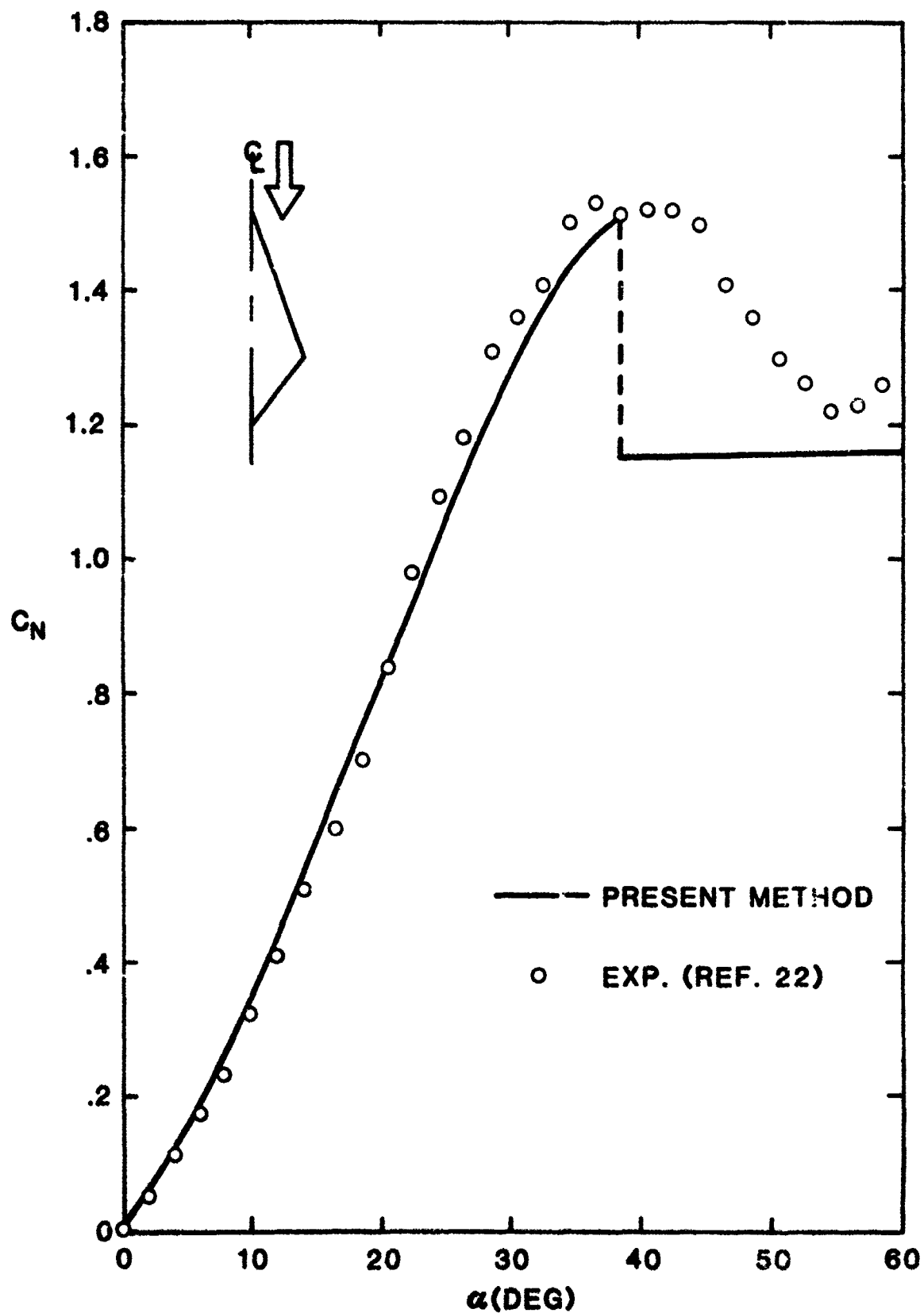


Figure 14. Normal Force Coefficient vs α for Diamond Planform ($A_e = 1$)

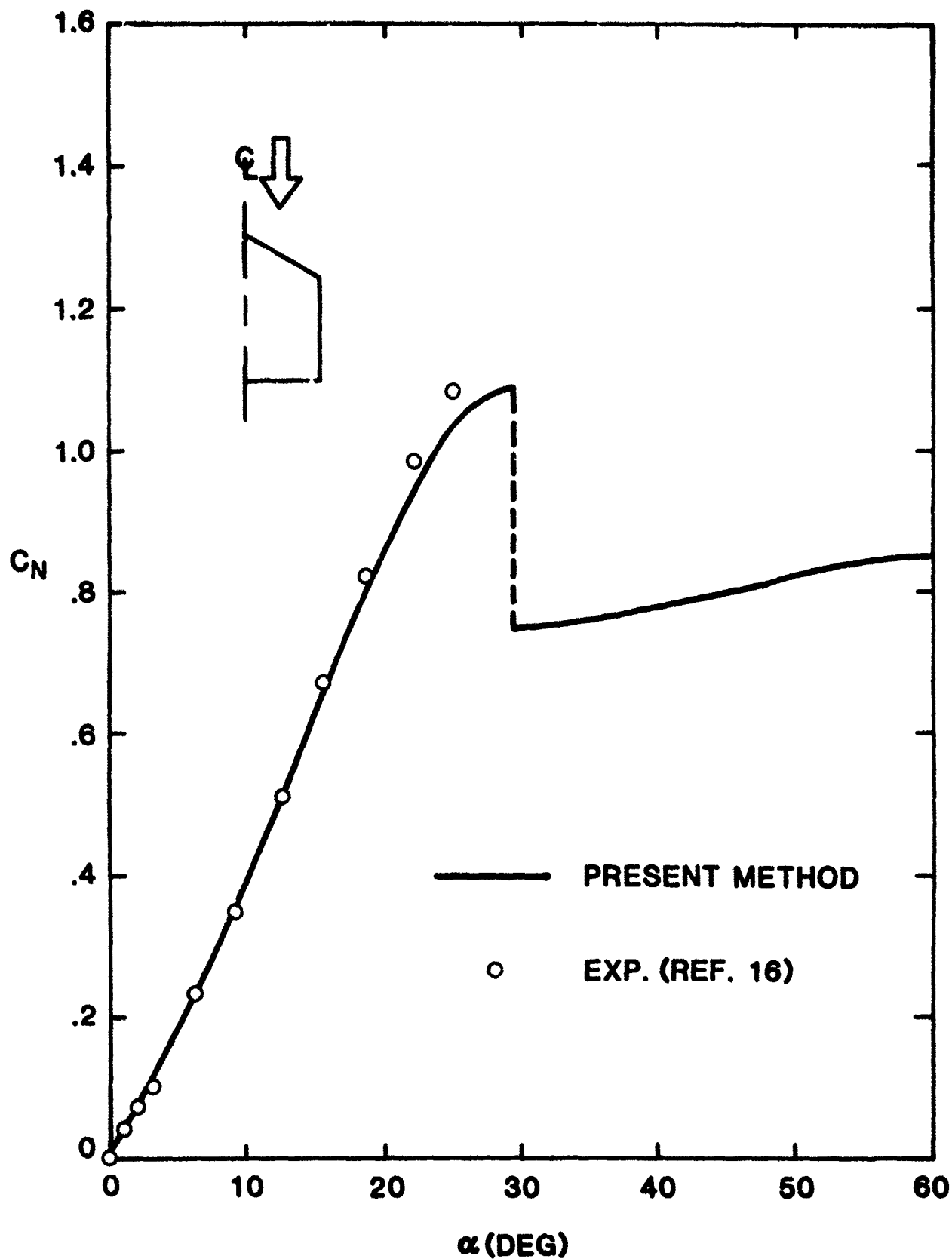


Figure 15. Normal Force Coefficient vs α for Clipped Delta Planform ($A_e = 1.23$)

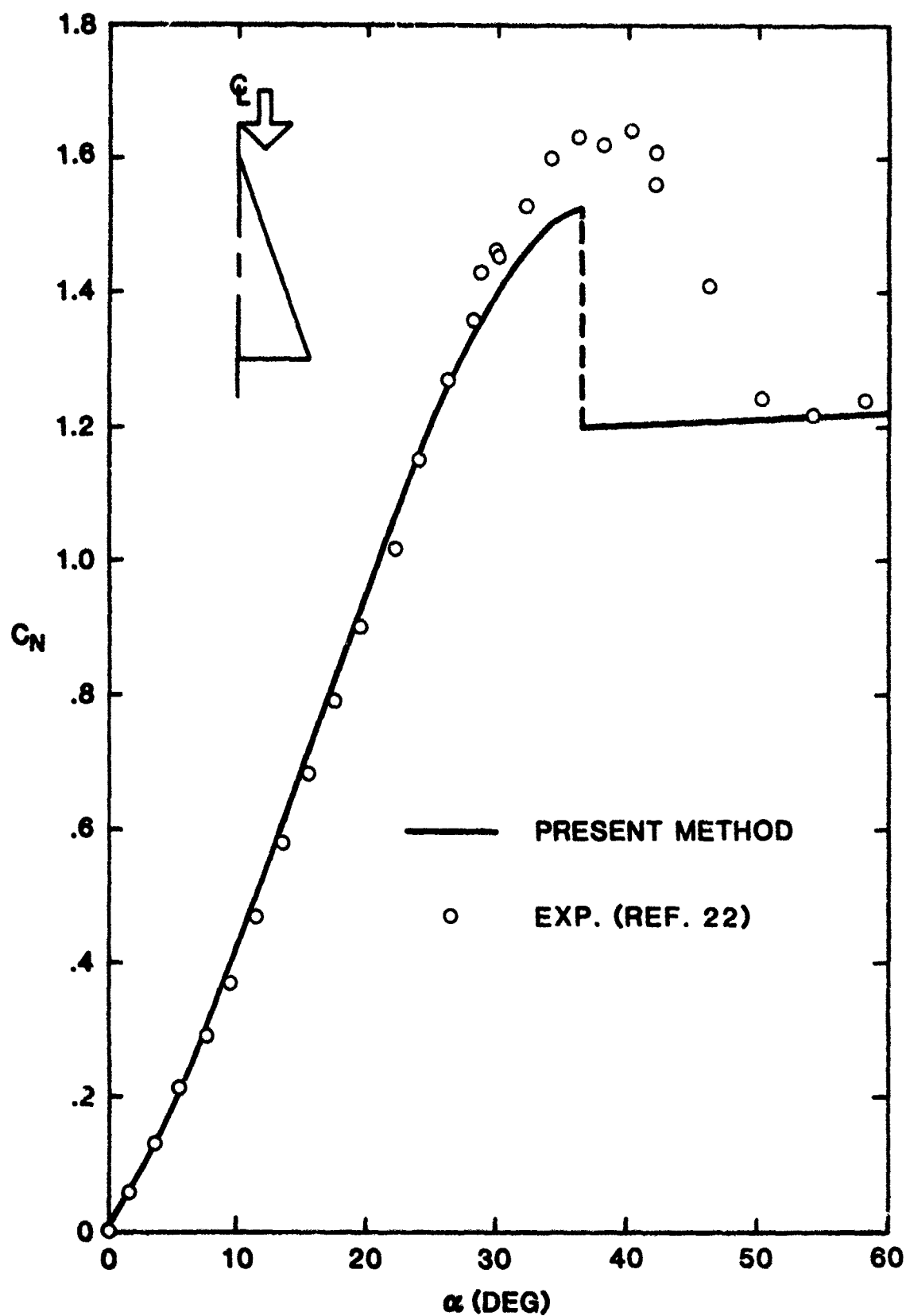


Figure 16. Normal Force Coefficient vs α for Delta Planform ($A_c = 1.46$)

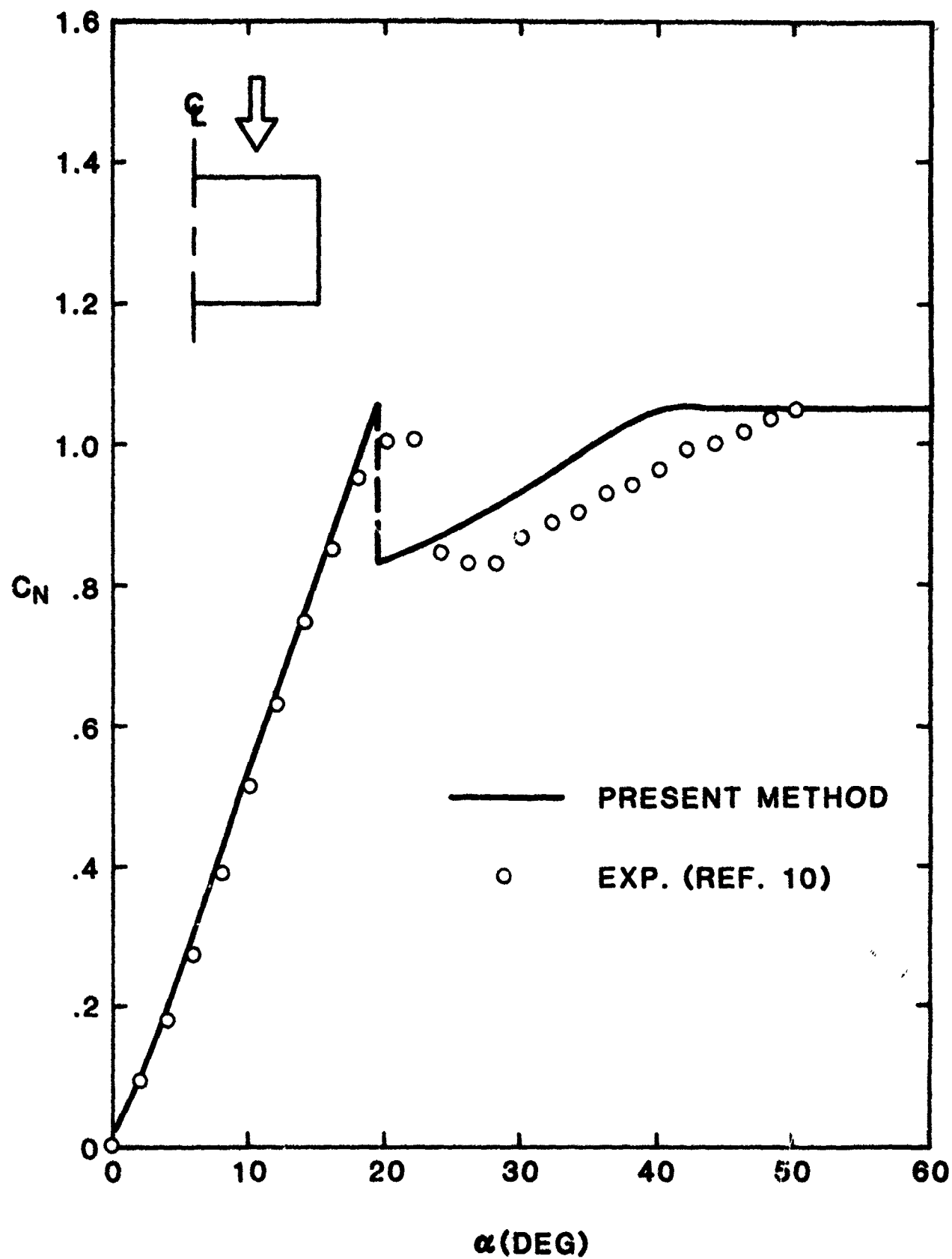


Figure 17. Normal Force Coefficient vs α for Rectangular Planform ($A_e = 2$)

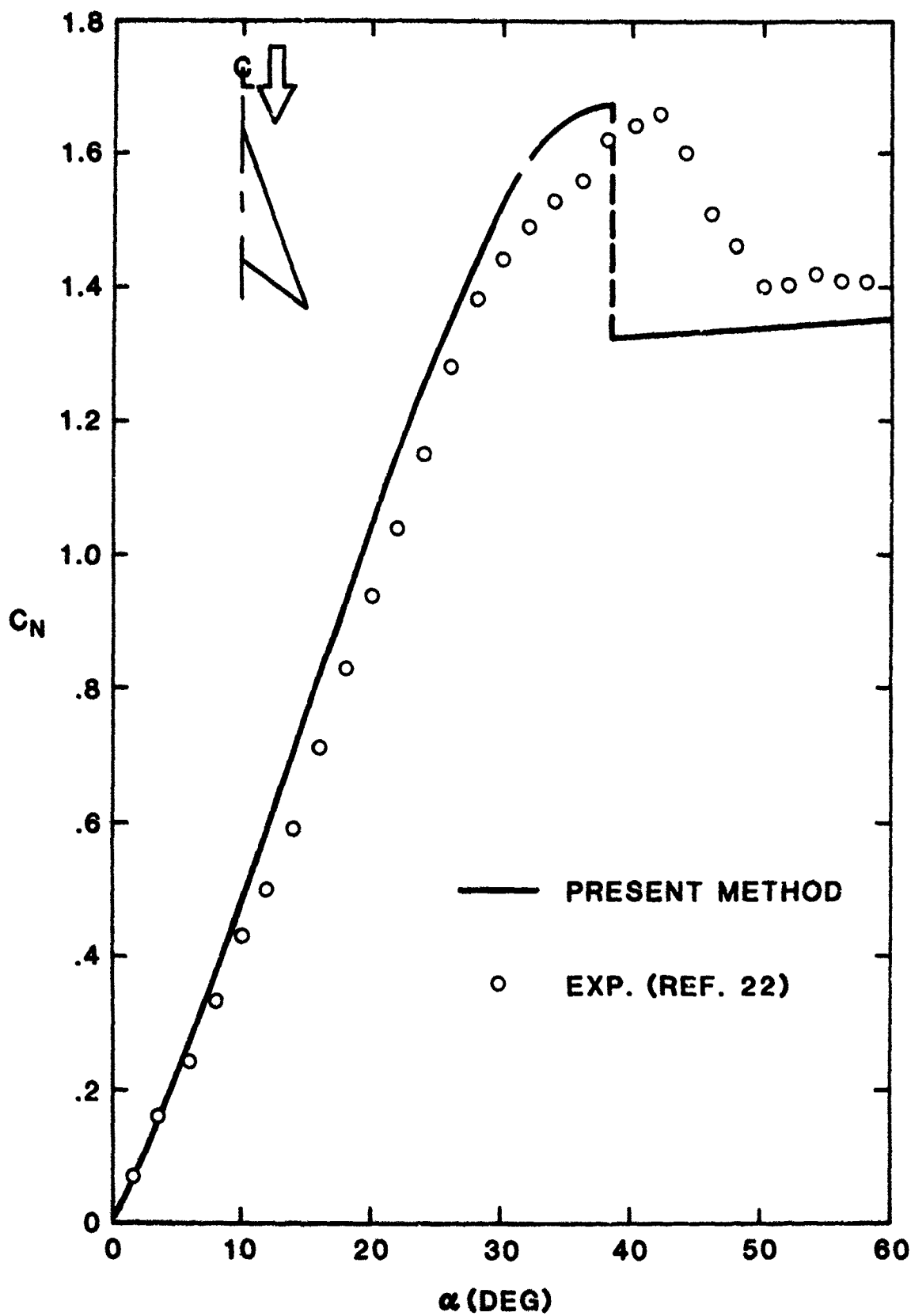


Figure 18. Normal Force Coefficient vs α for Arrow Planform ($A_e = 2$)

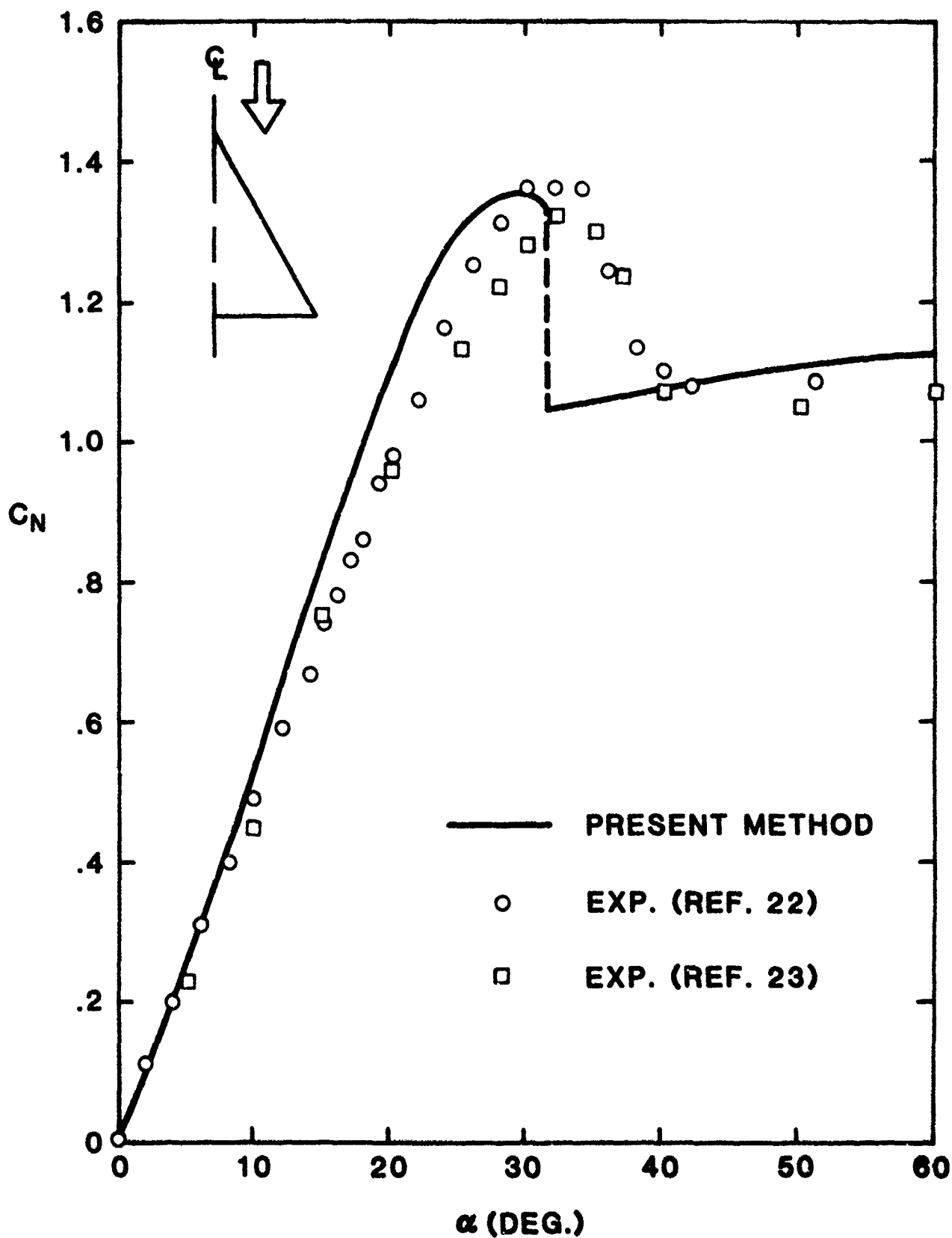


Figure 19. Normal Force Coefficient vs α for Delta Planform ($A_e = 2.31$)

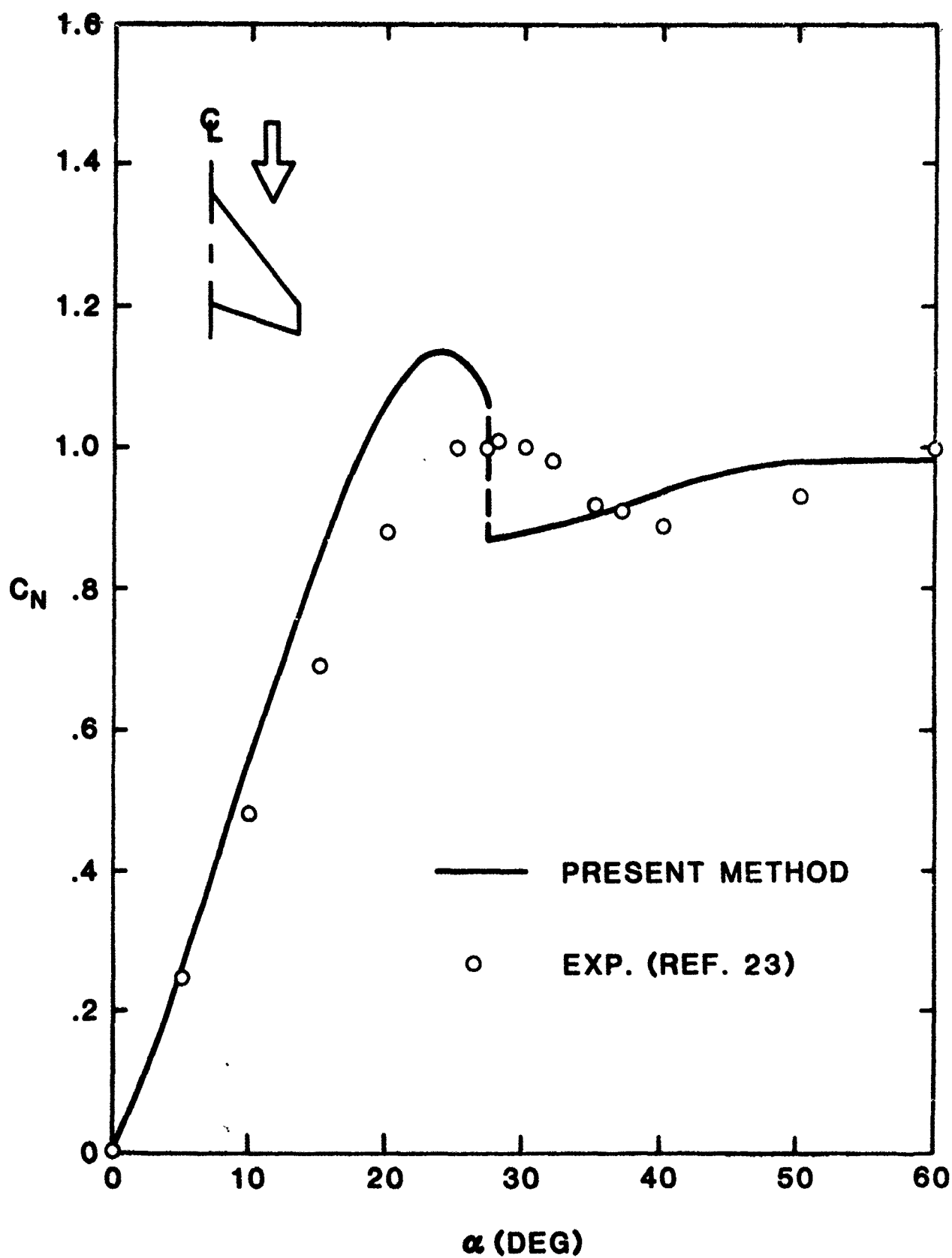


Figure 20. Normal Force Coefficient vs α for Clipped Arrow Planform ($A_e = 2.61$)

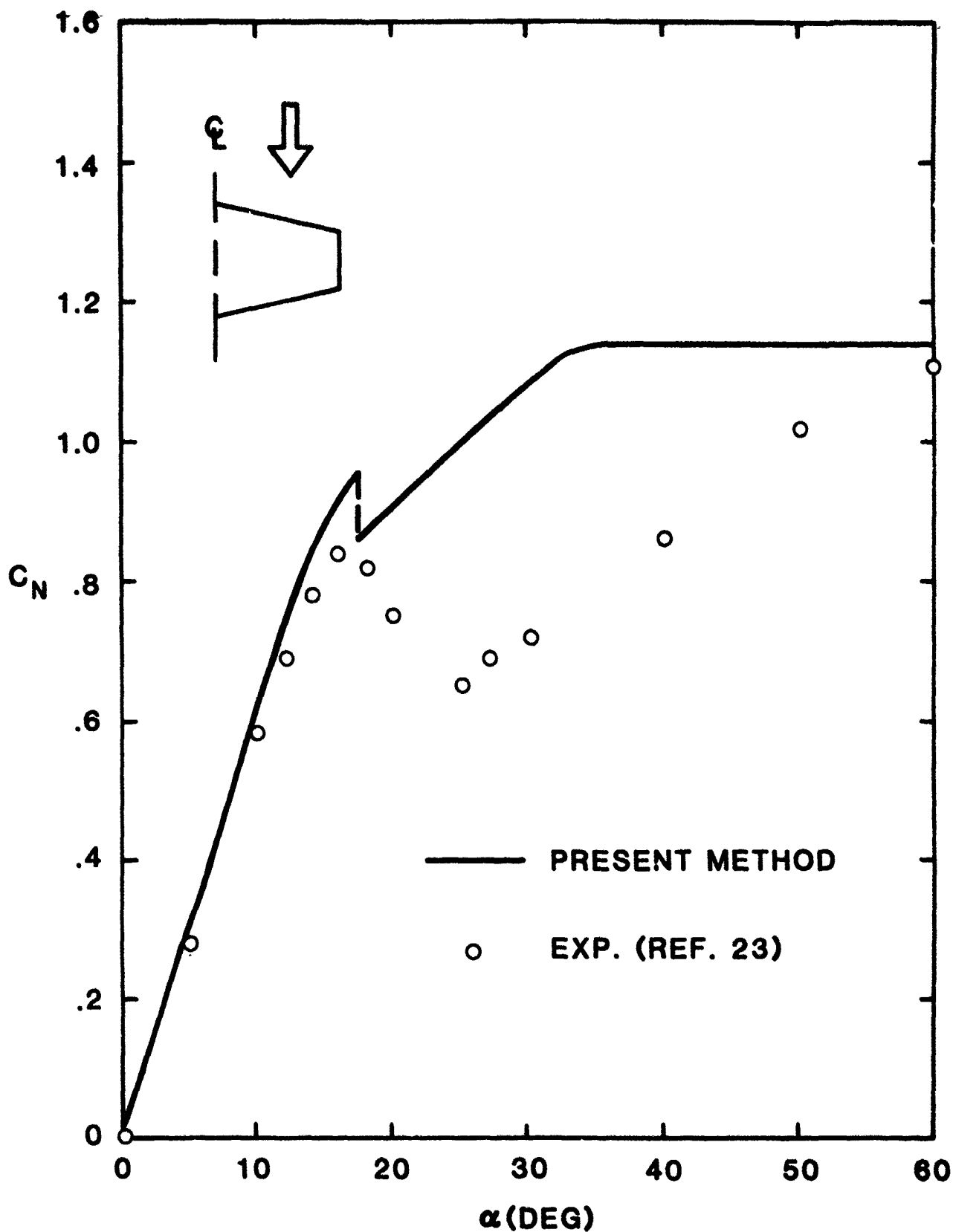


Figure 21. Normal Force Coefficient vs α for Trapezoidal Planform ($A_e = 3.$)

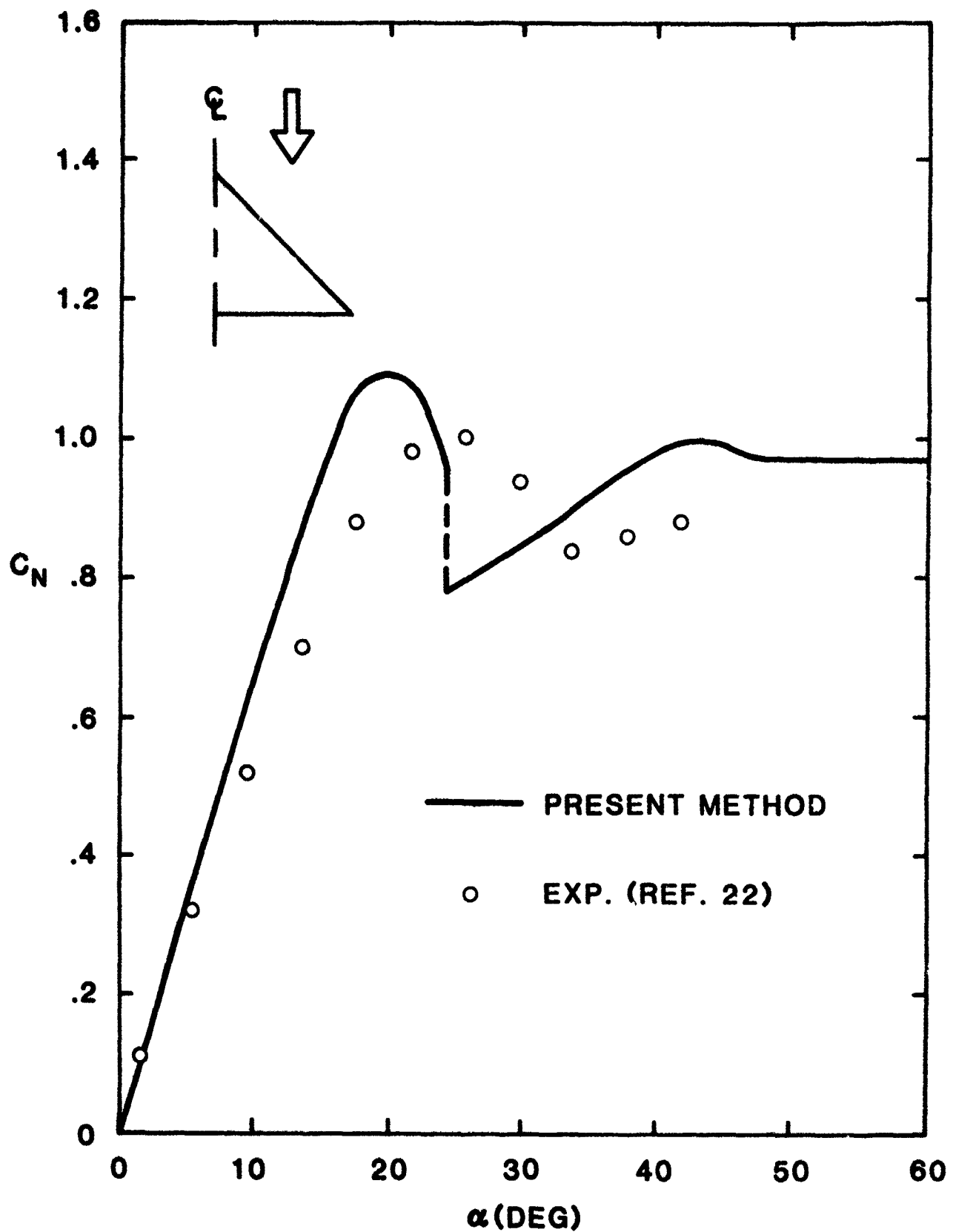
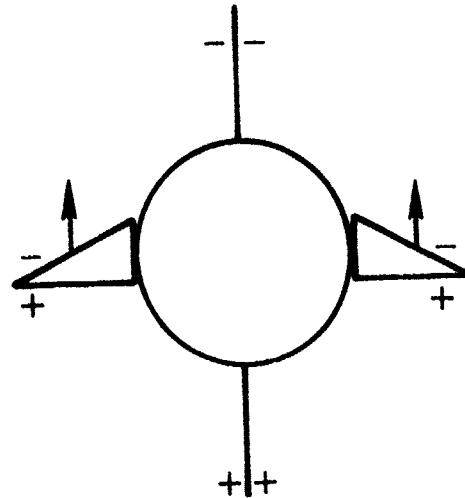
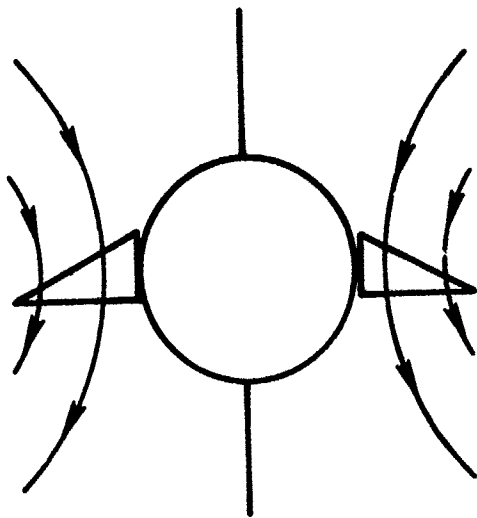


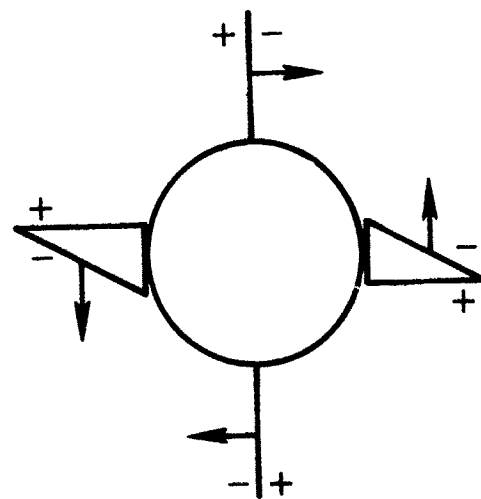
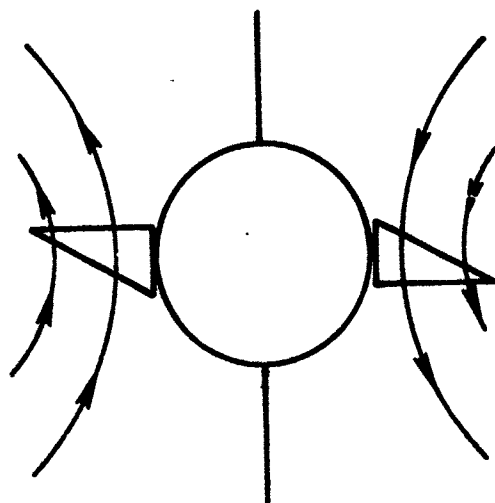
Figure 22. Normal Force Coefficient vs α for Delta Planform ($A_e = 4.$)

Induced Flow Field

Induced Pressure Field

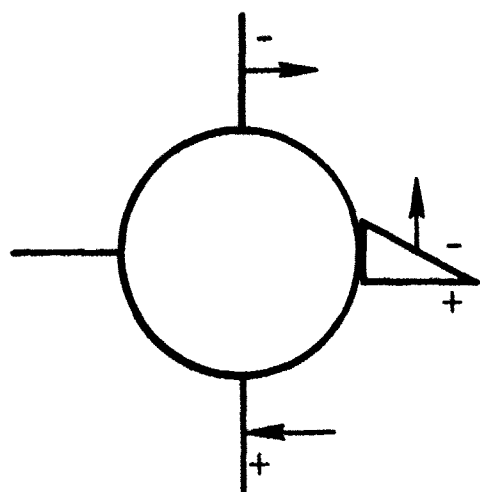


a) Pitch Control

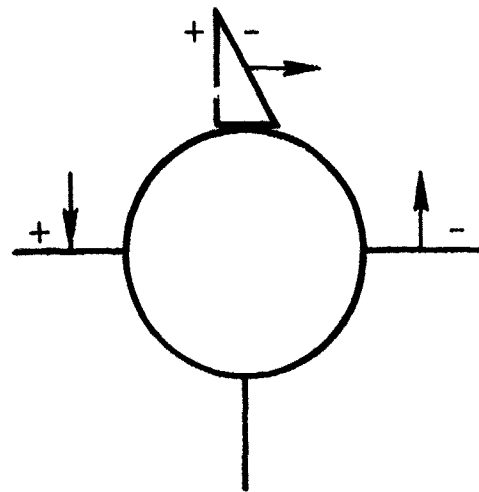


b) Roll Control

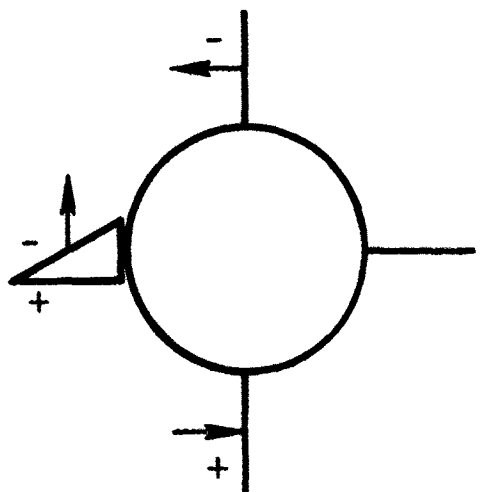
Figure 23. Control Interference for Pitch and Roll Control
(from Ref. 24)



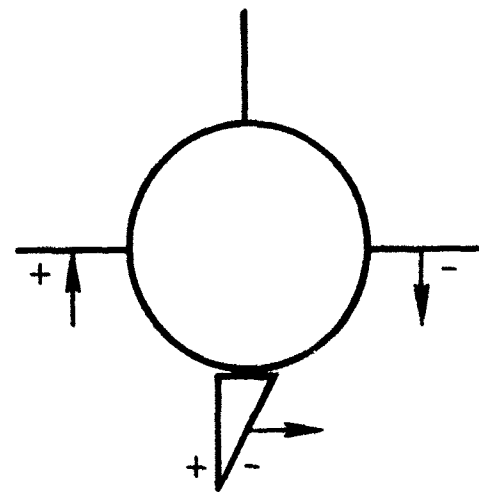
a) Panel 1 Deflection



b) Panel 2 Deflection



c) Panel 3 Deflection



d) Panel 4 Deflection

Figure 24. Control Interference for Individual Panel Deflection

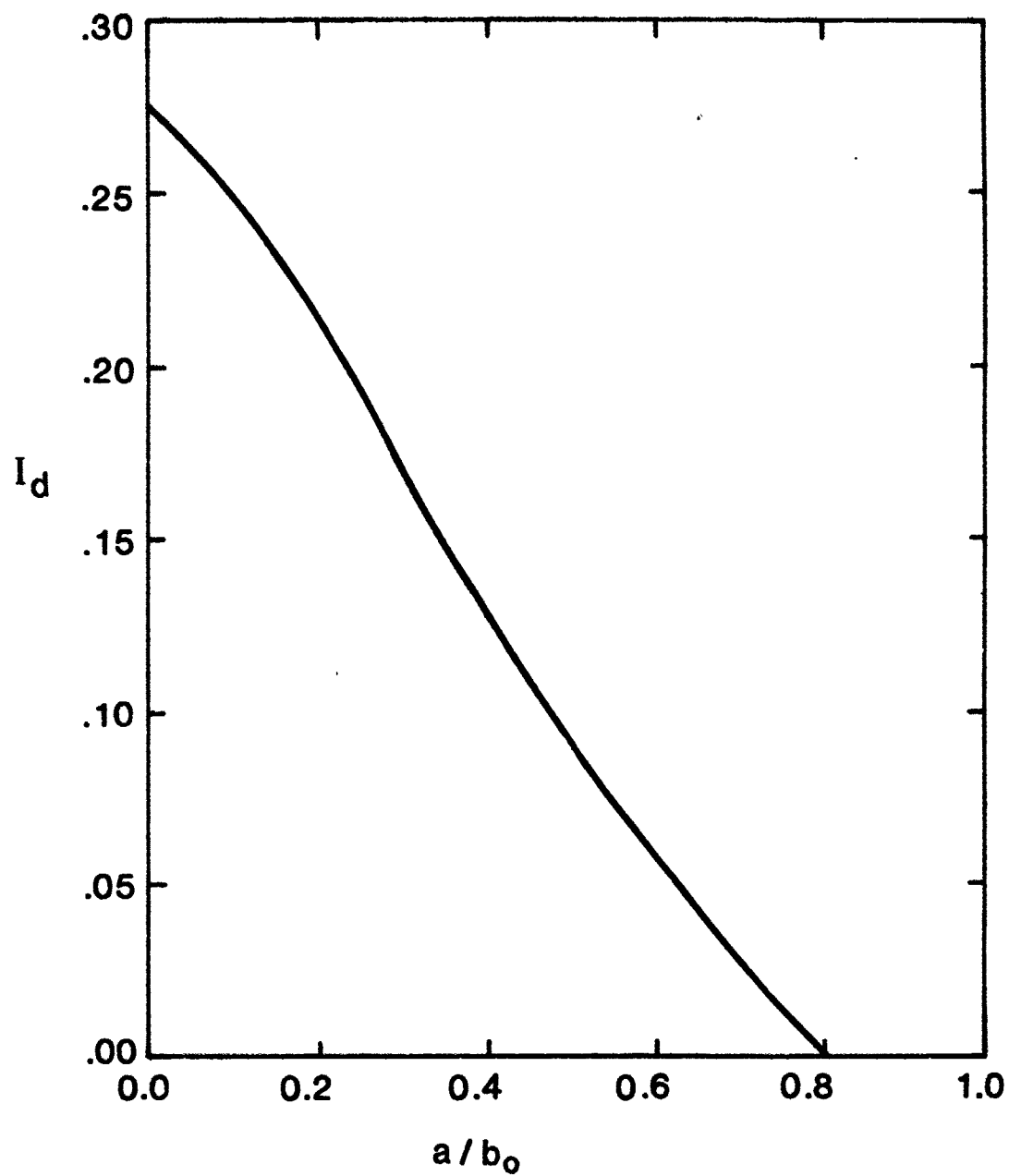


Figure 25. Deflection Interference Coefficient vs a/b_0

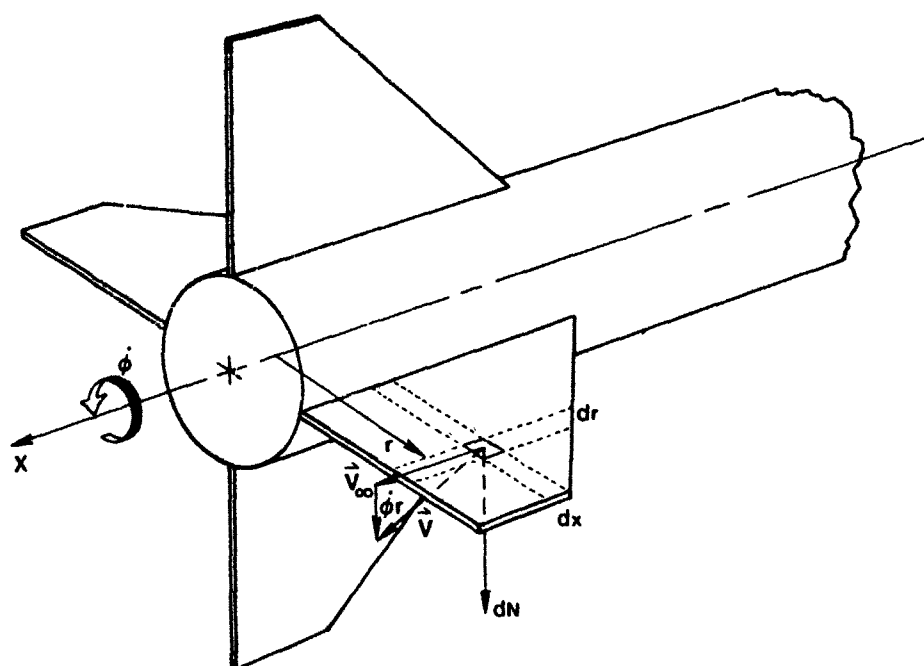


Figure 26. Induced Angle of Attack Due to Rolling Speed

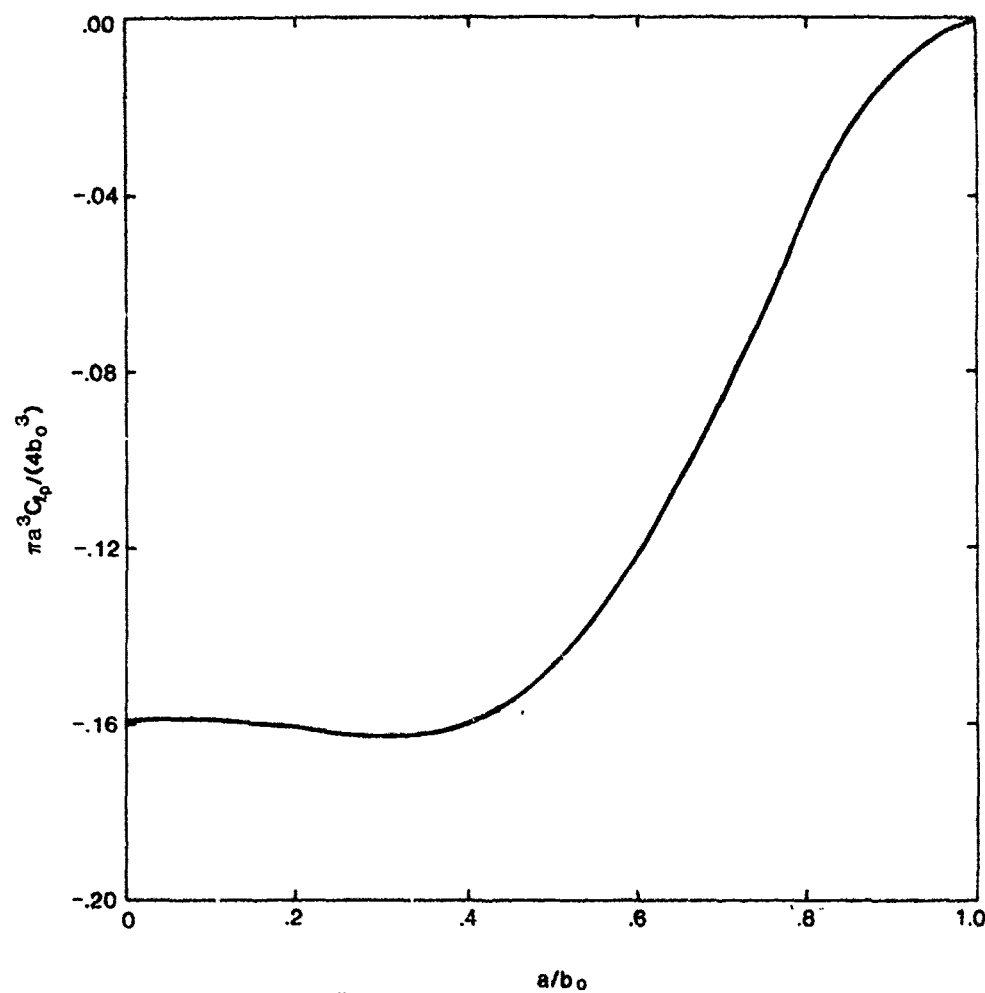


Figure 27. Roll Damping Moment Coefficient vs a/b_0

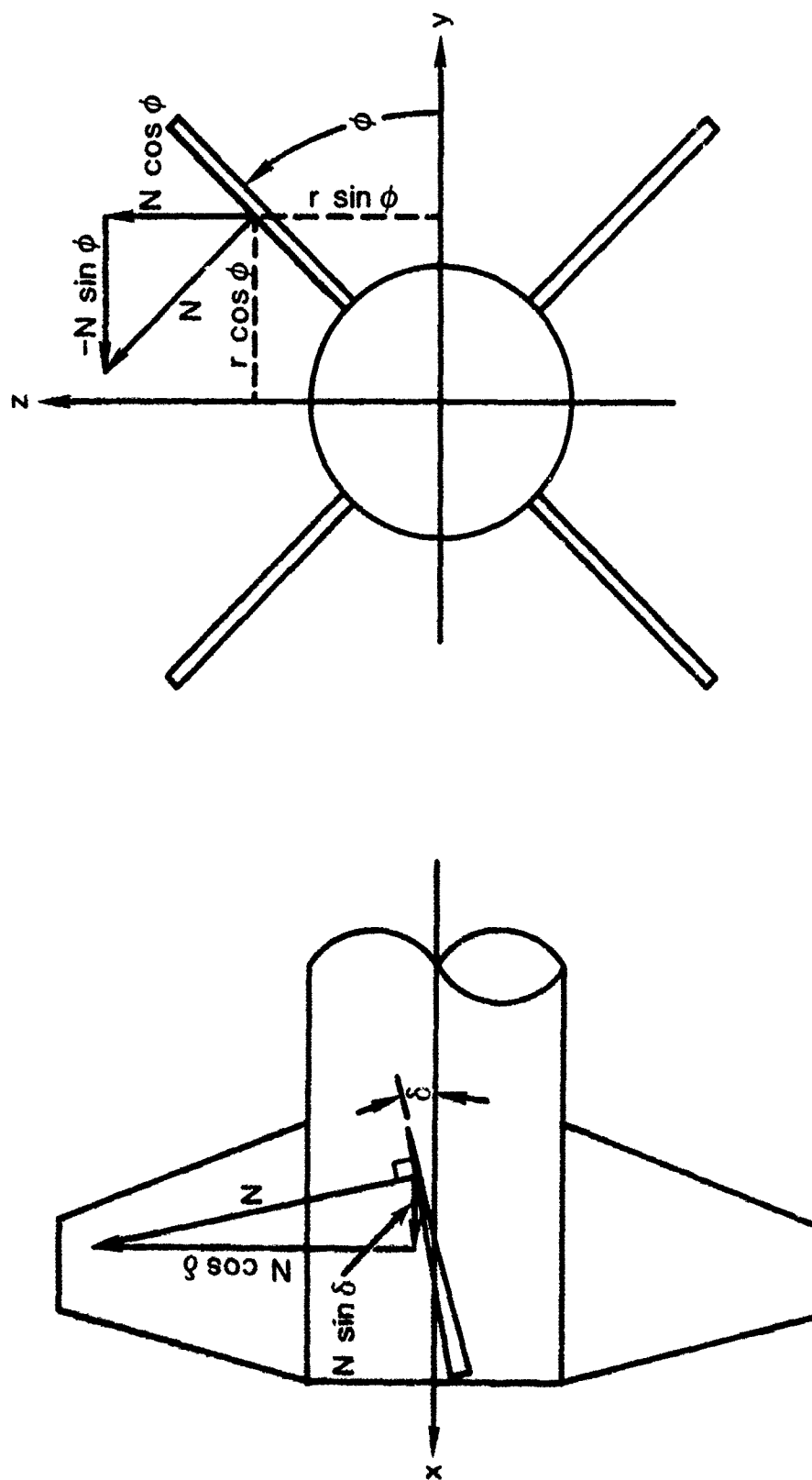


Figure 28. Components of the Fin Normal Force

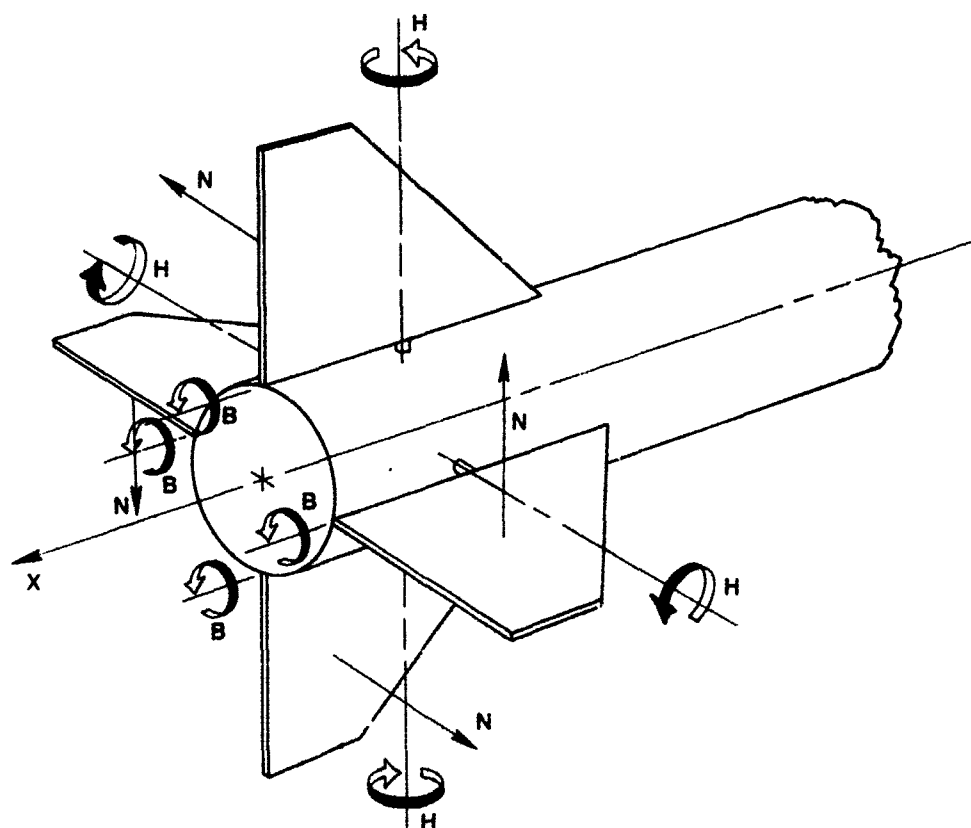
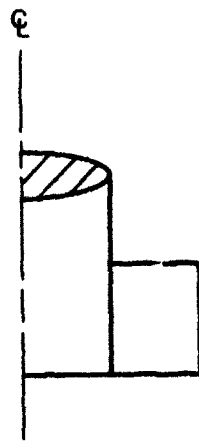


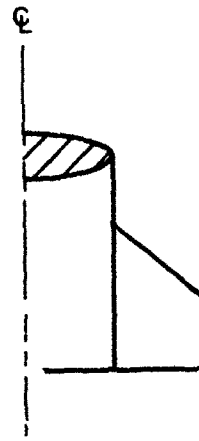
Figure 29. Sign Convention for Panel Normal Force, Hinge Moment, and Root Bending Moment



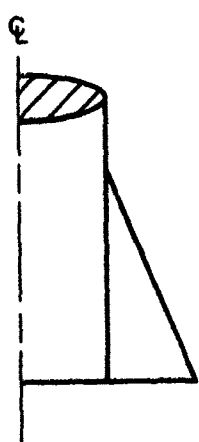
CONFIG. A



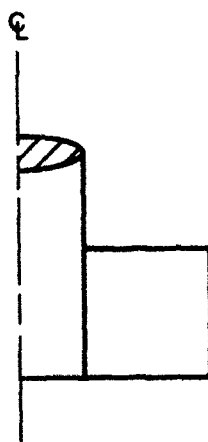
CONFIG. B



CONFIG. C



CONFIG. D



CONFIG. E



CONFIG. F

Figure 30. Fin Planforms Used for Comparison of Theory and Experiment

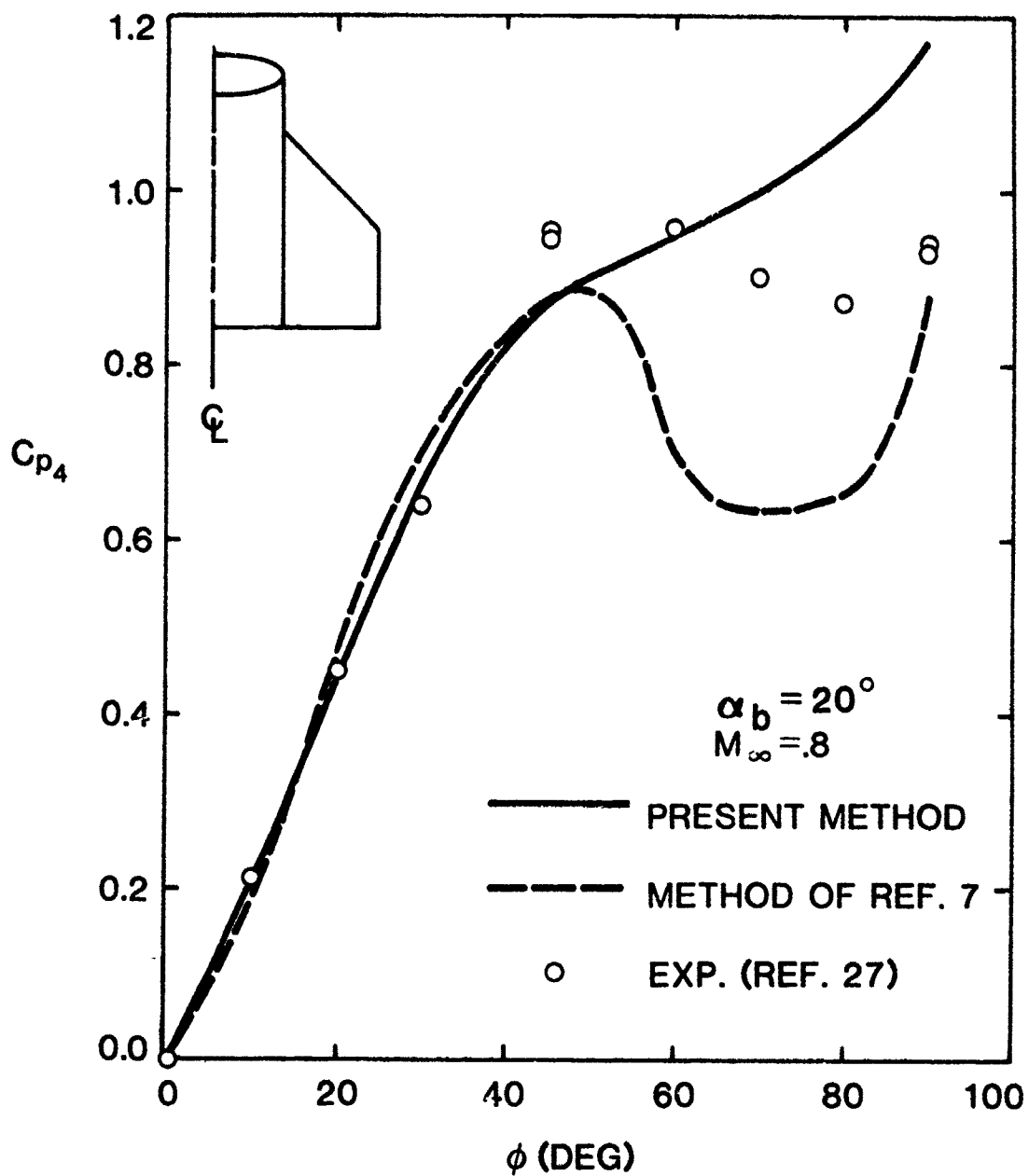


Figure 31. Windward Panel Normal Force vs Roll Angle for Configuration A ($M_\infty = .8$)

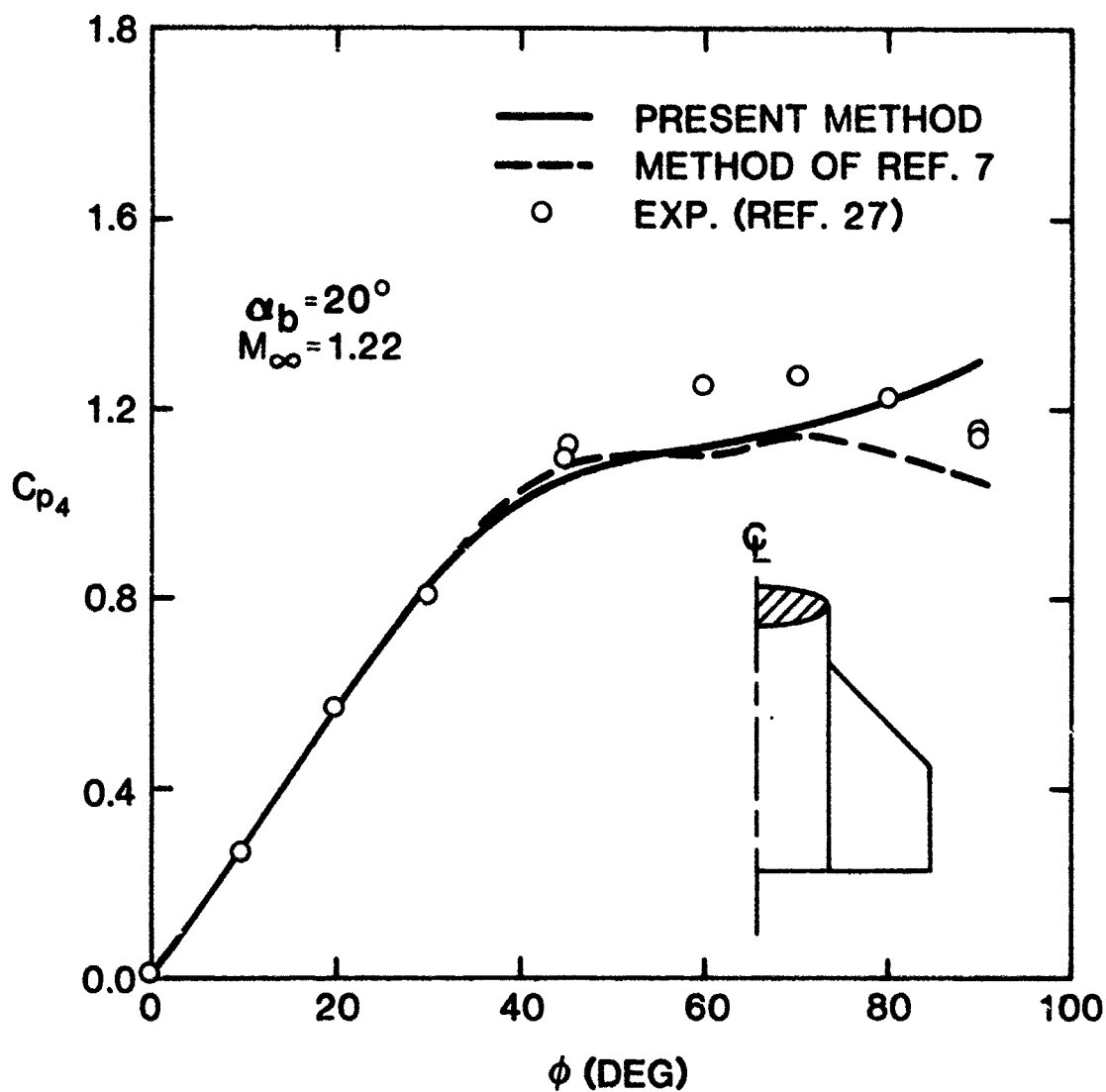


Figure 32. Windward Panel Normal Force vs Roll Angle for Configuration A ($M_\infty = 1.22$)

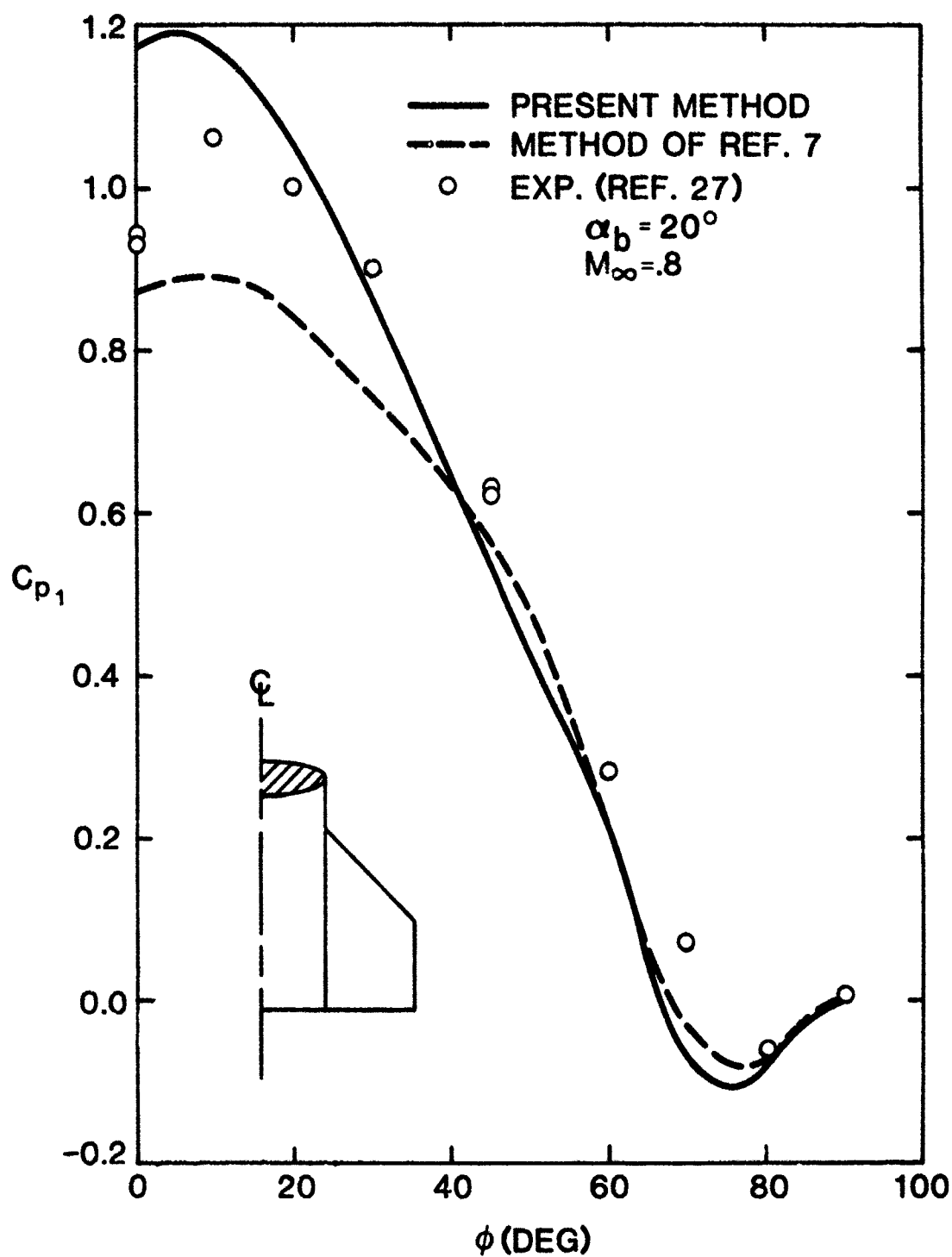


Figure 33. Leeward Panel Normal Force vs Roll Angle for Configuration A ($M_\infty = 0.8$)

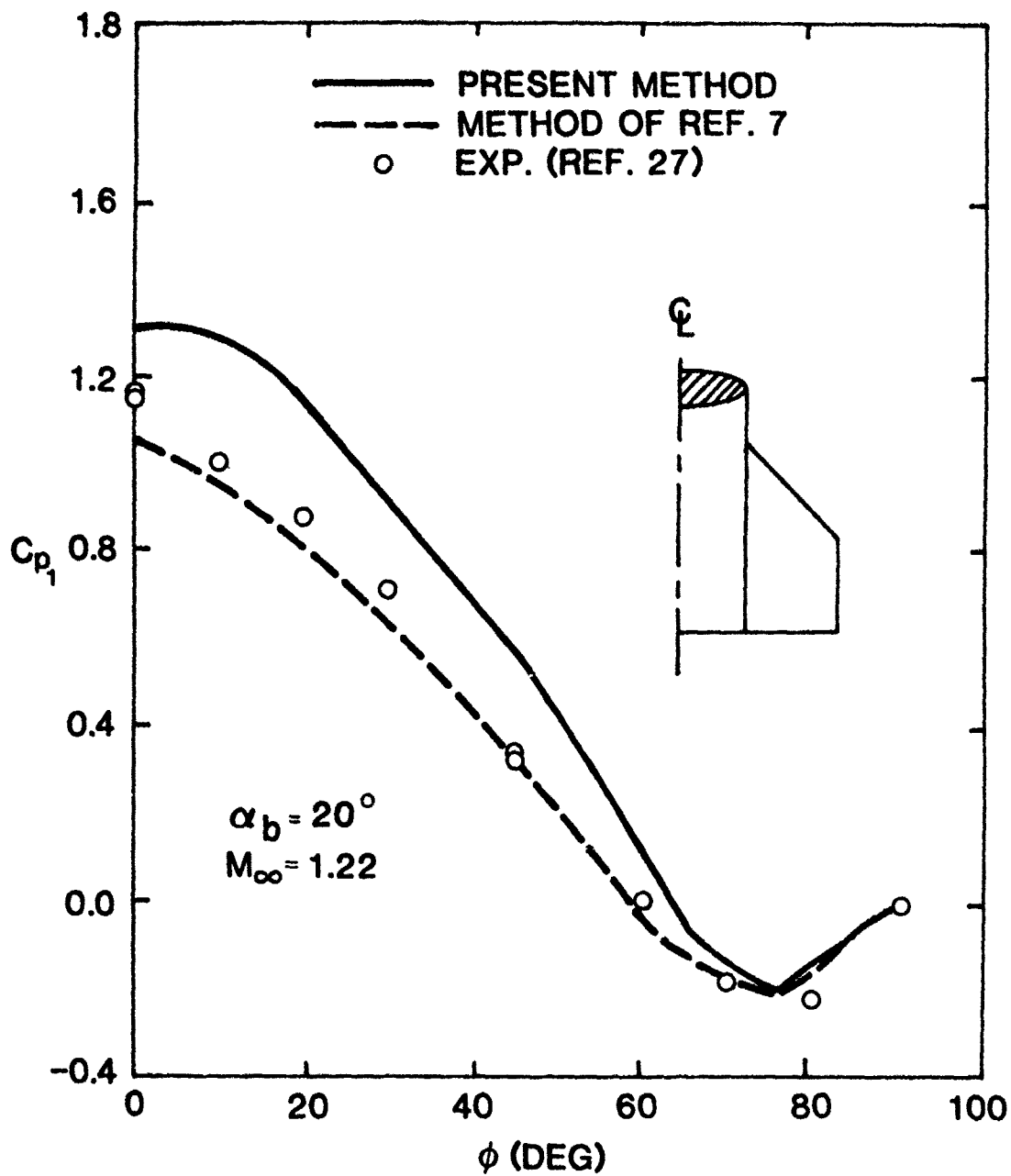


Figure 34. Leeward Panel Normal Force vs Roll Angle for Configuration A ($M_\infty = 1.22$)

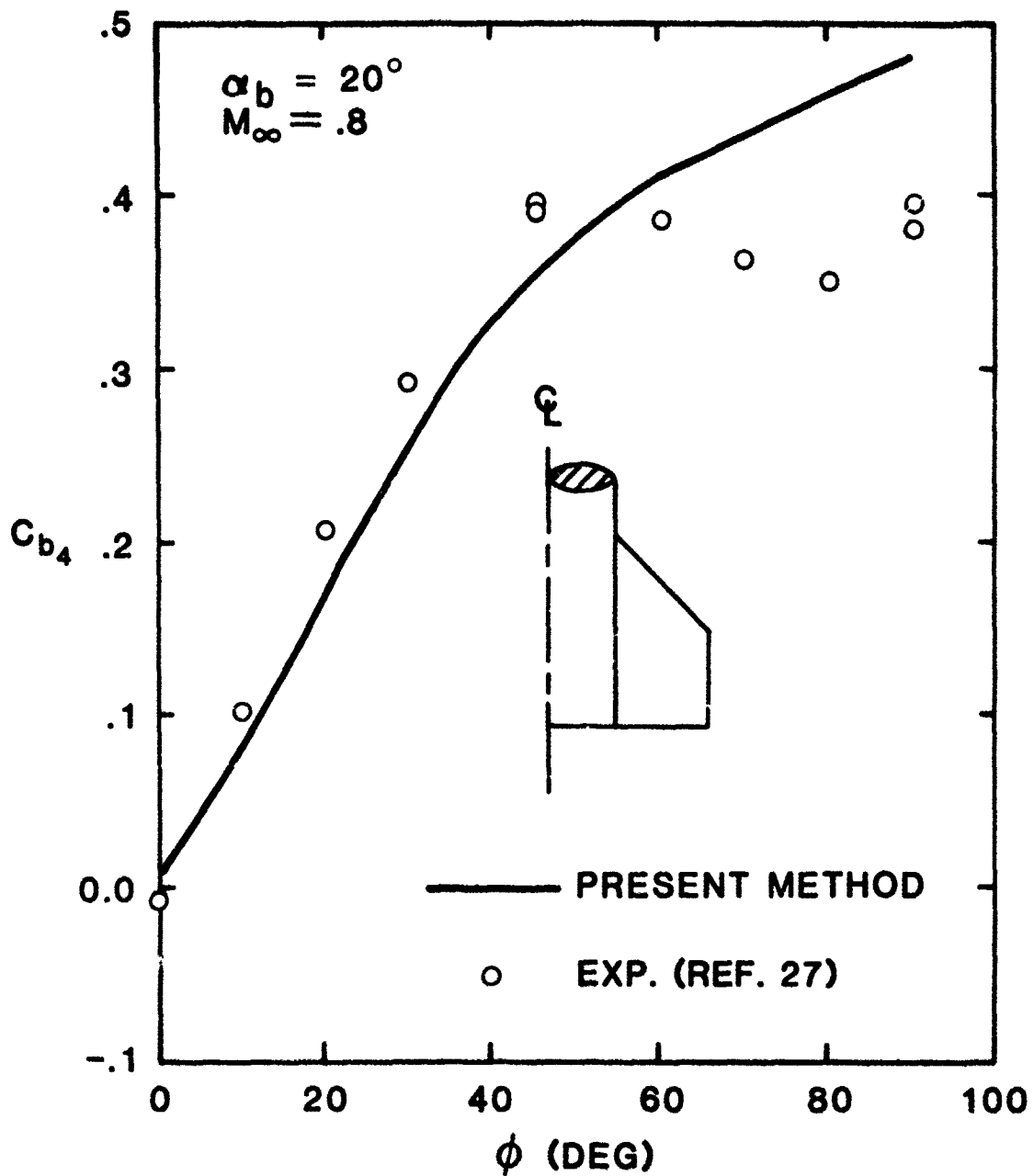


Figure 35. Windward Fin Root Bending Moment vs Roll Angle for Configuration A ($M_\infty = .8$)

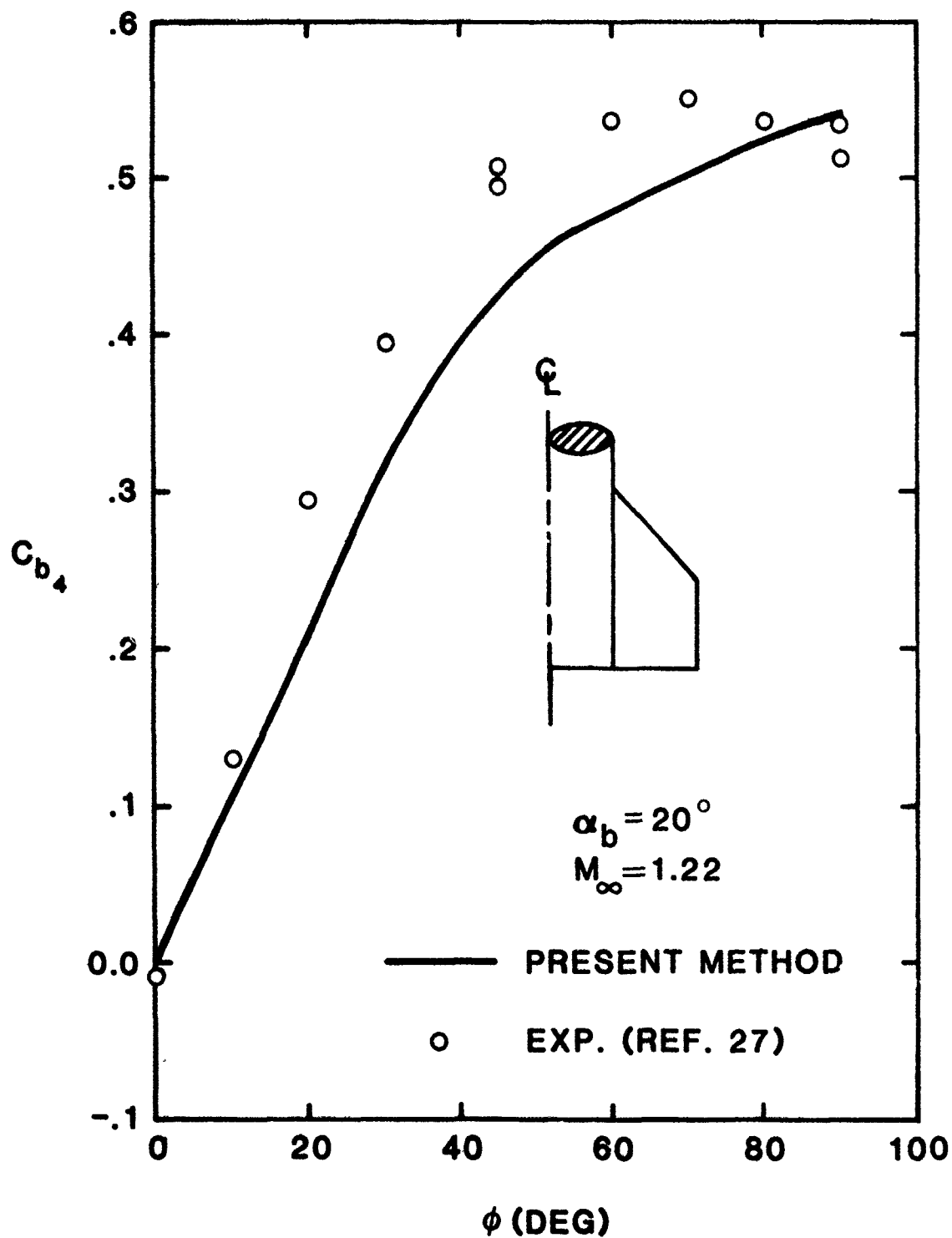


Figure 36. Windward Fin Root Bending Moment vs Roll Angle for Configuration A ($M_\infty = 1.22$)

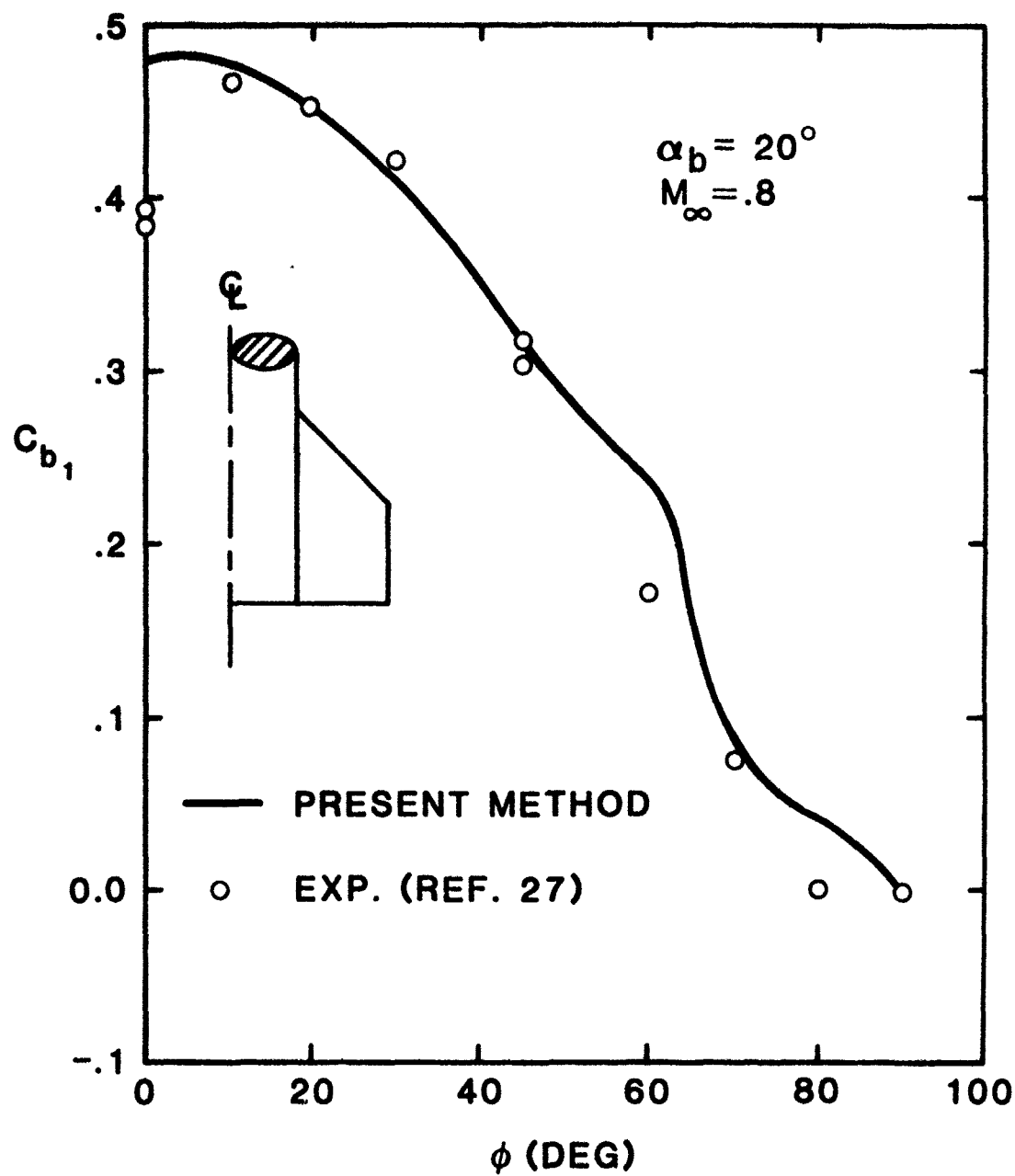


Figure 37. Leeward Fin Root Bending Moment vs Roll Angle for Configuration A ($M_\infty = .8$)

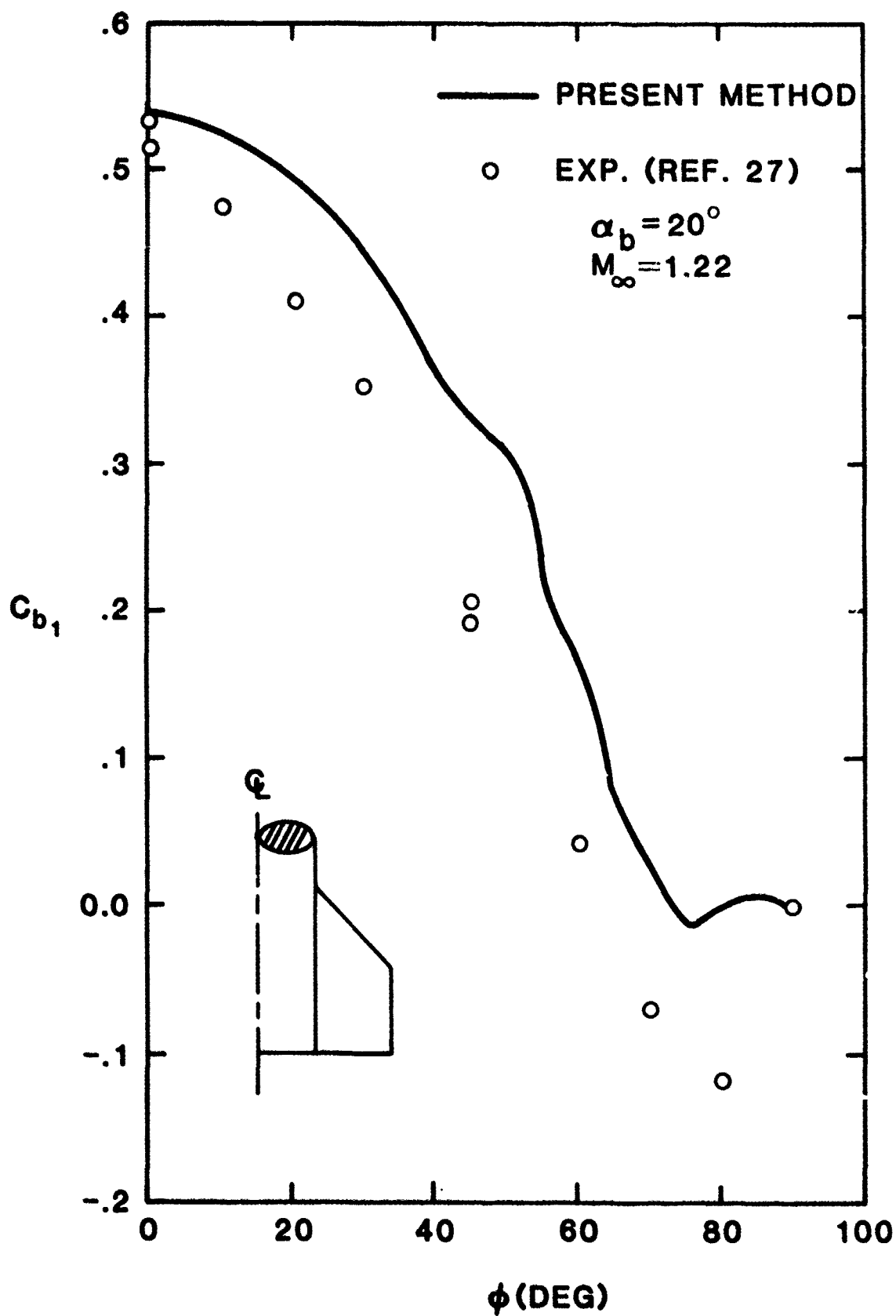
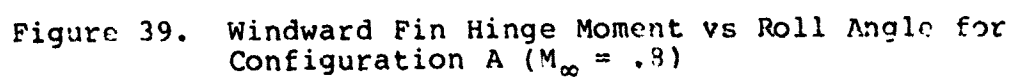


Figure 38. Leeward Fin Root Bending Moment vs Roll Angle for Configuration A ($M_\infty = 1.22$)



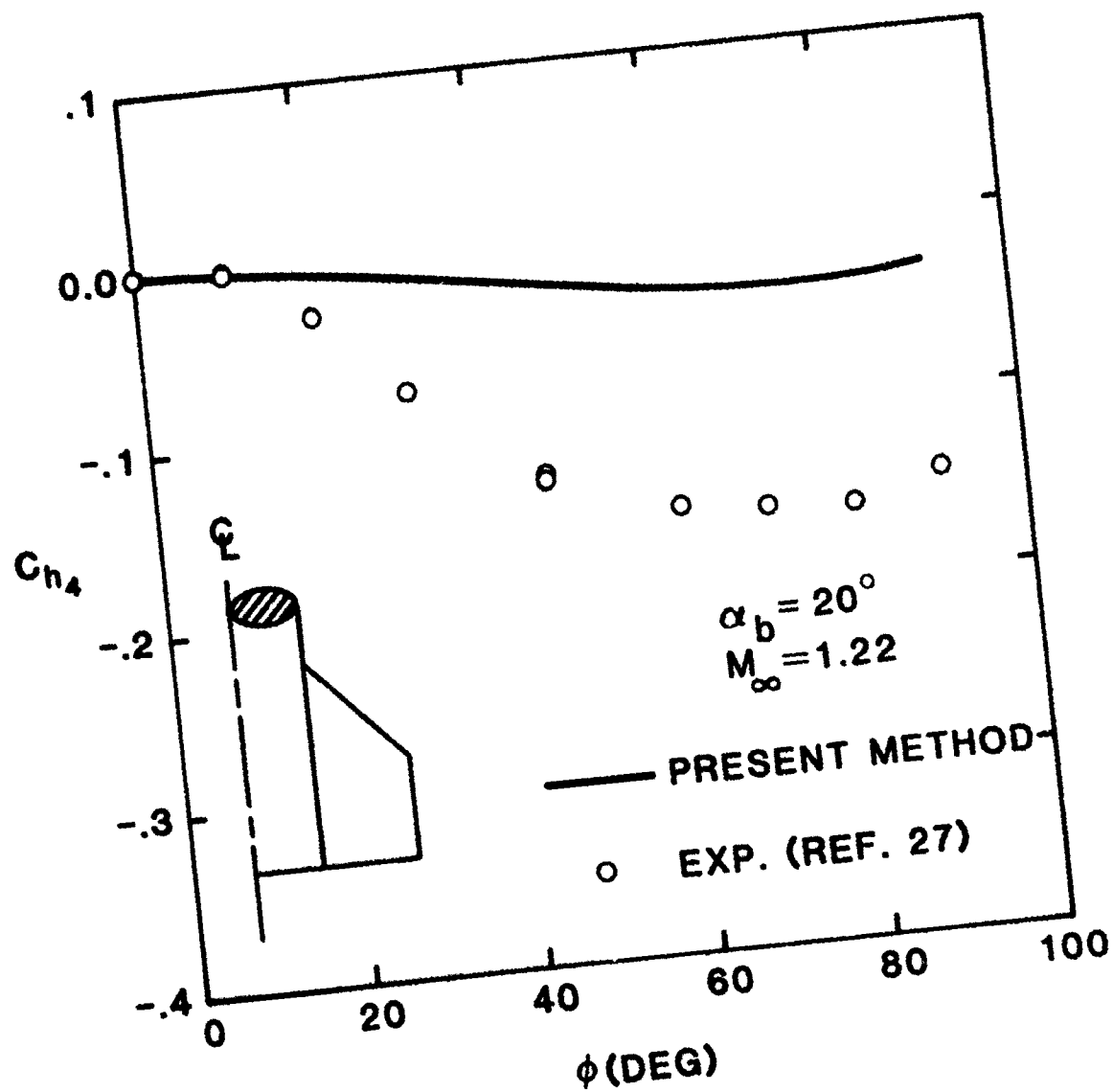


Figure 40. Windward Fin Hinge Moment vs Roll Angle for Configuration A ($M_\infty = 1.22$)

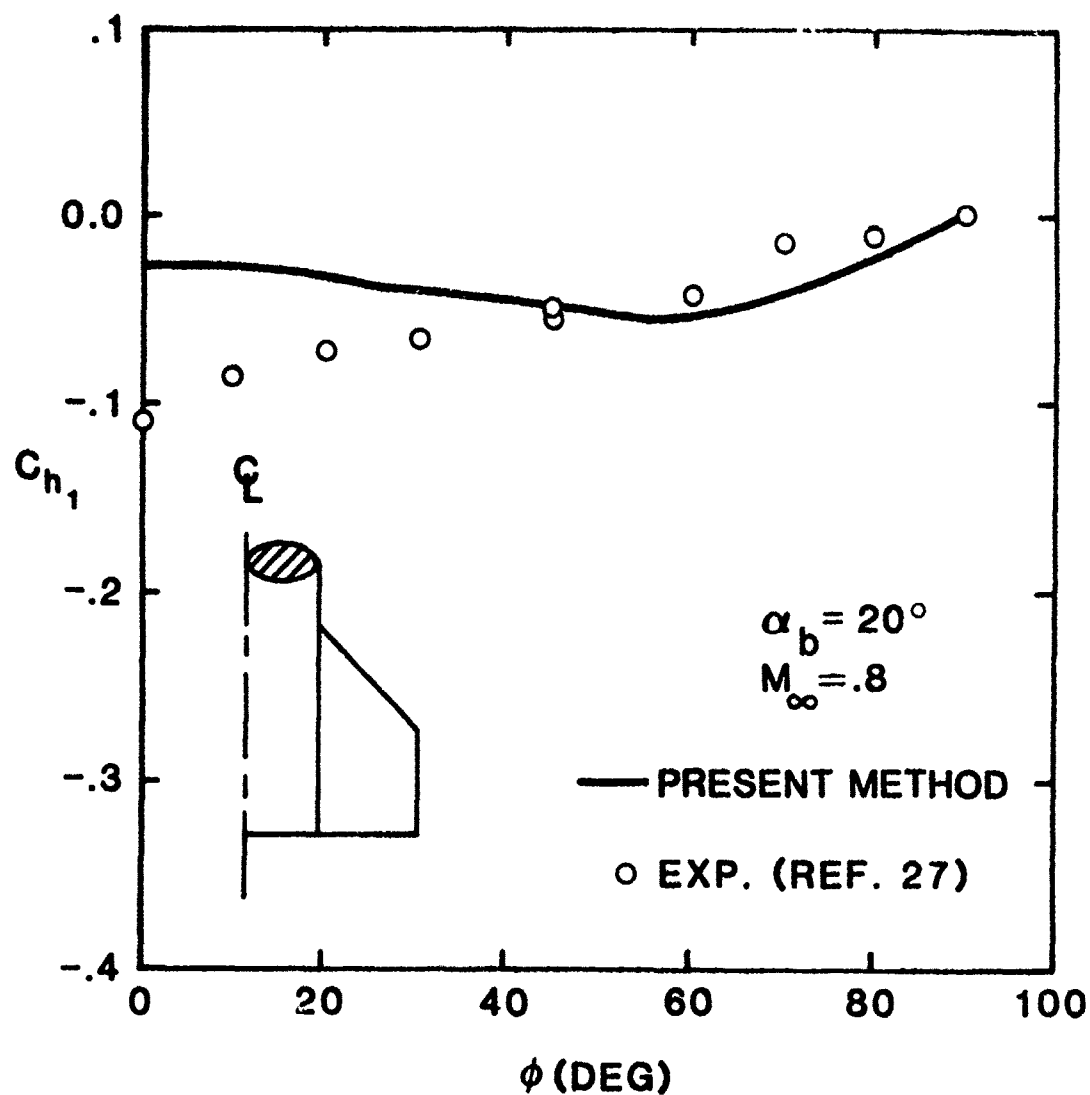


Figure 41. Leeward Fin Hinge Moment vs Roll Angle for Configuration A ($M_\infty = .8$)

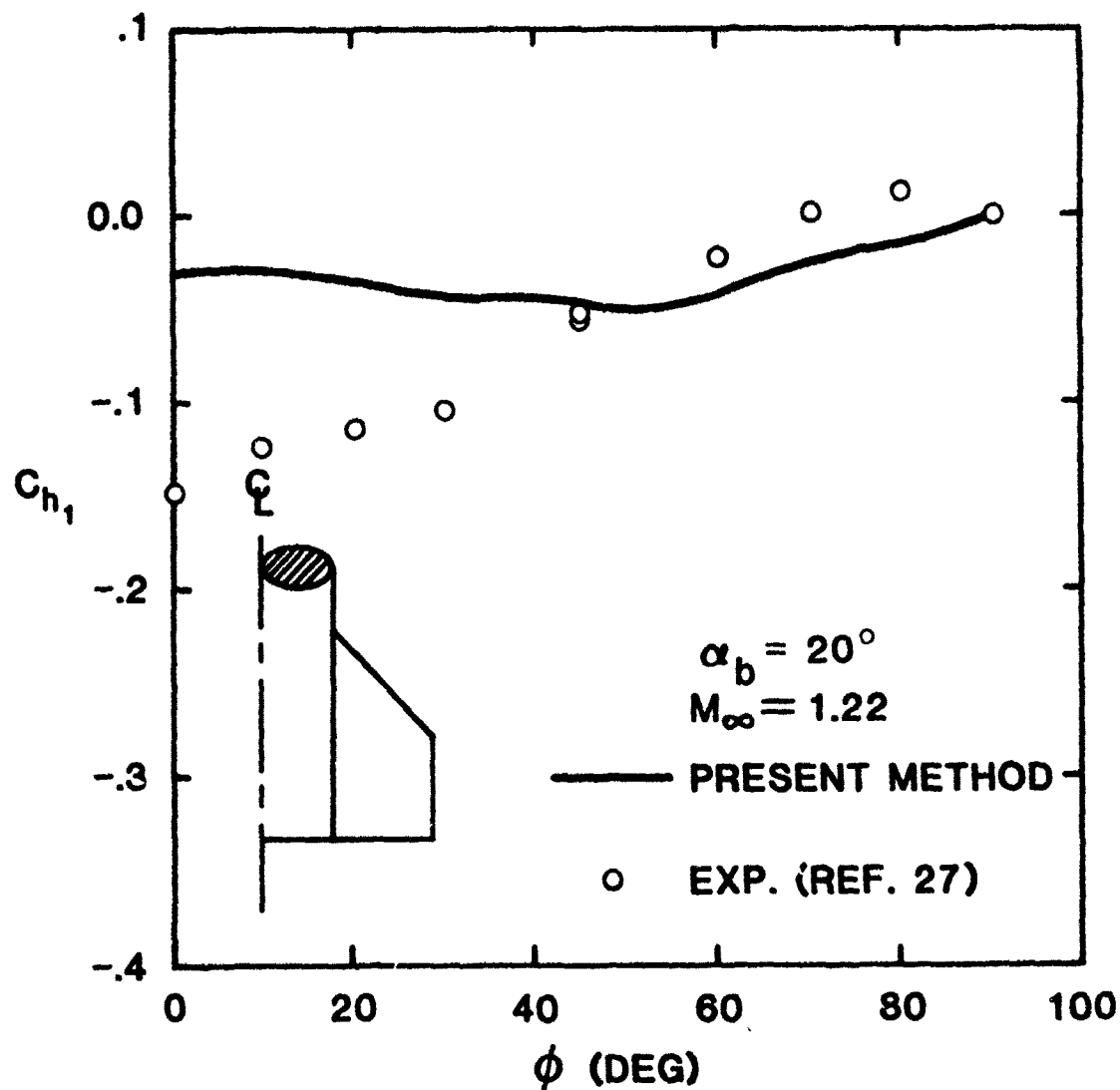


Figure 42. Leeward Fin Hinge Moment vs Roll Angle for Configuration A ($M_\infty = 1.22$)

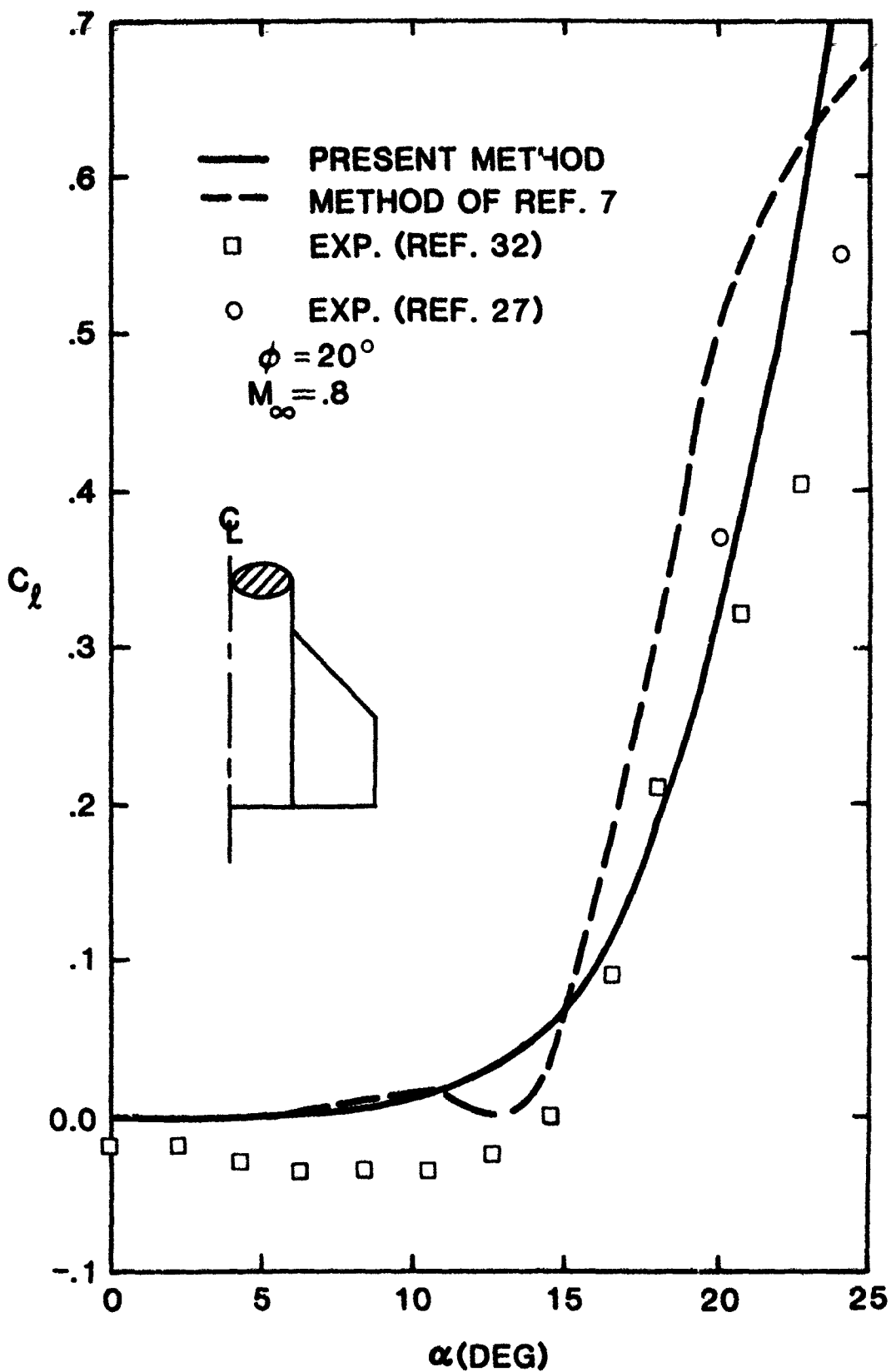


Figure 43. Induced Roll Moment vs α_b for Configuration A ($M_\infty = .8$)

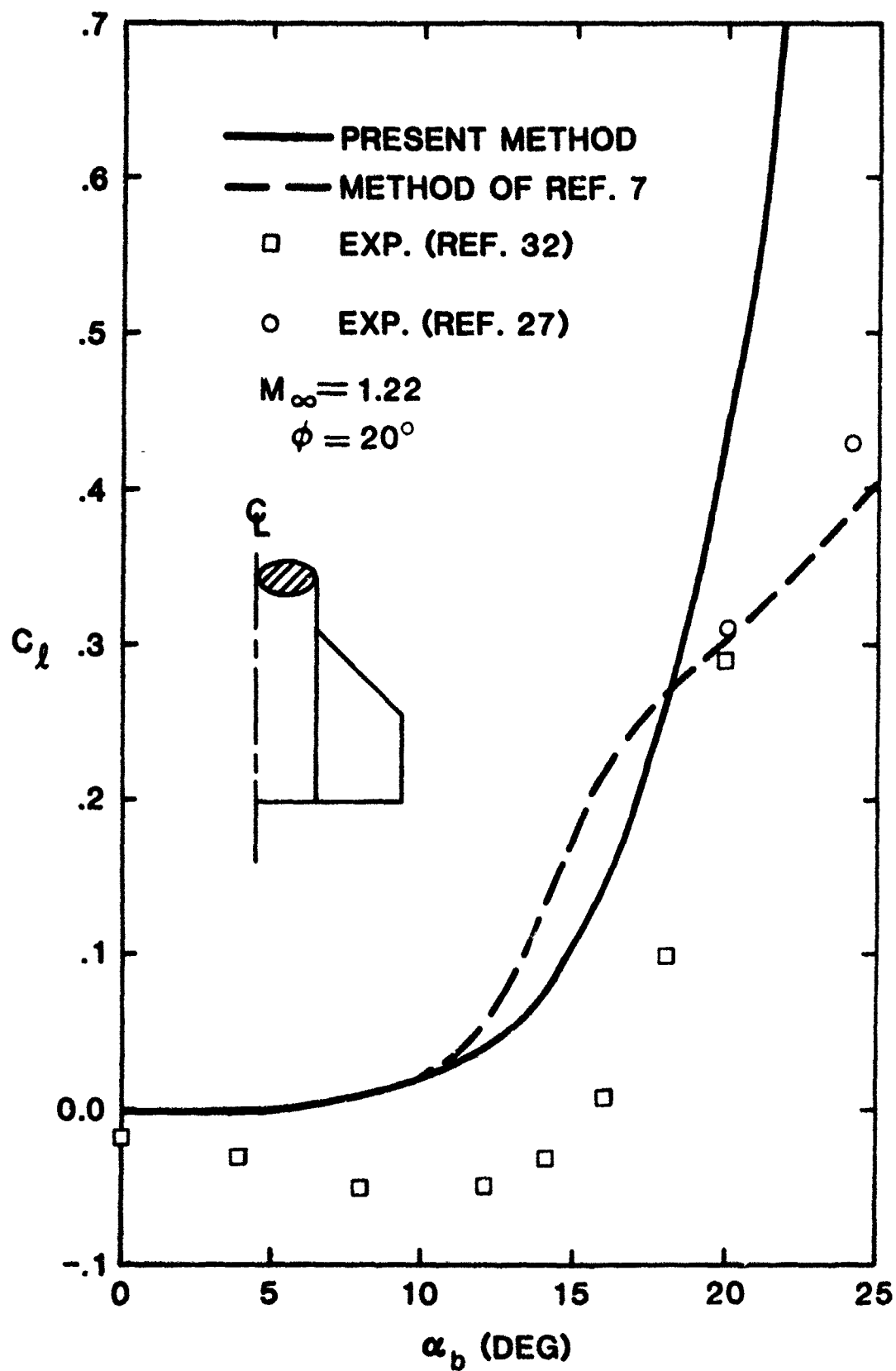


Figure 44. Induced Roll Moment vs α_b for Configuration A ($M_\infty = 1.22$)

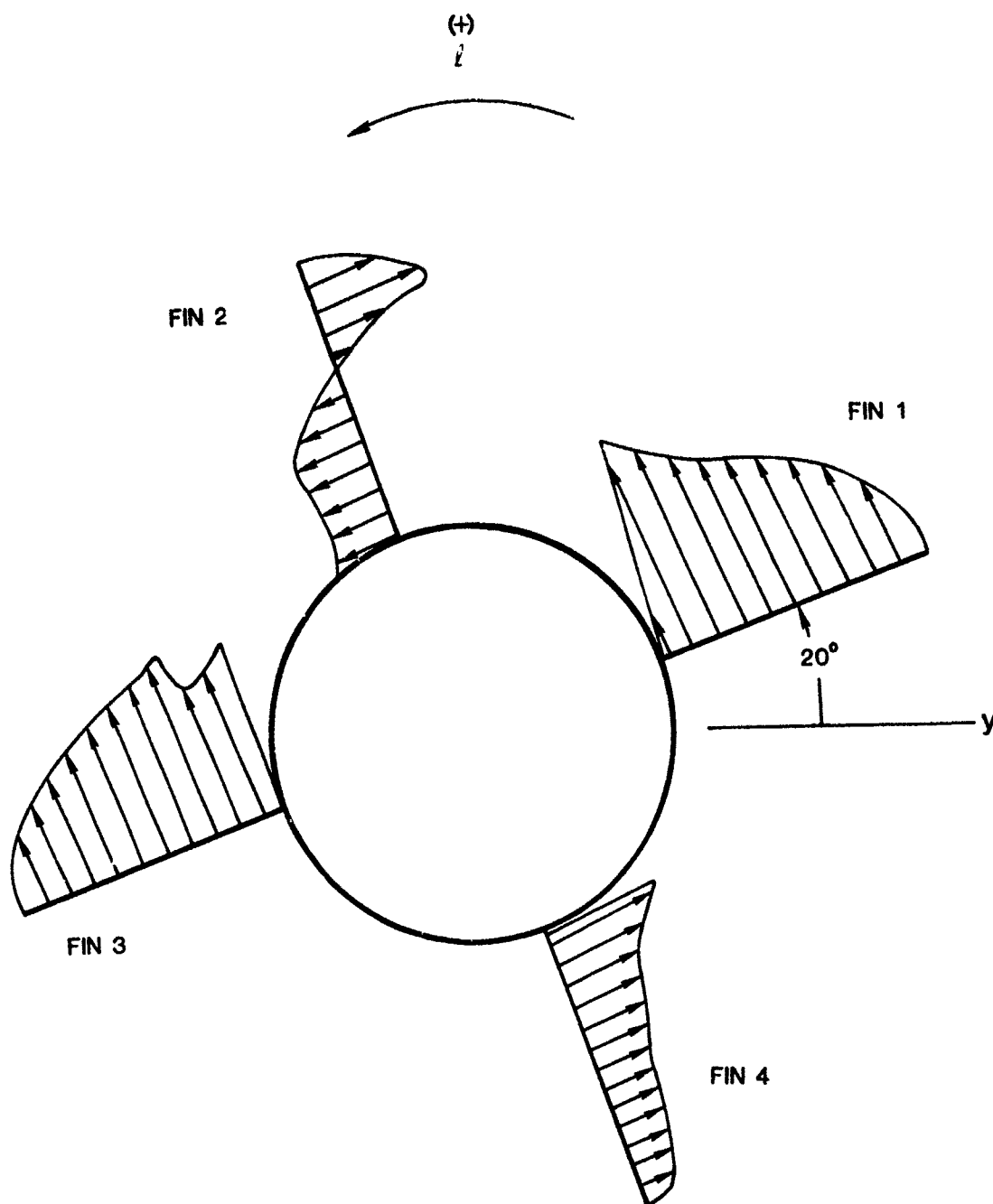


Figure 46. Spanwise Fin Loading for $\alpha_b = 20^\circ$, $\phi = 20^\circ$
Configuration A ($M_\infty = .8$)

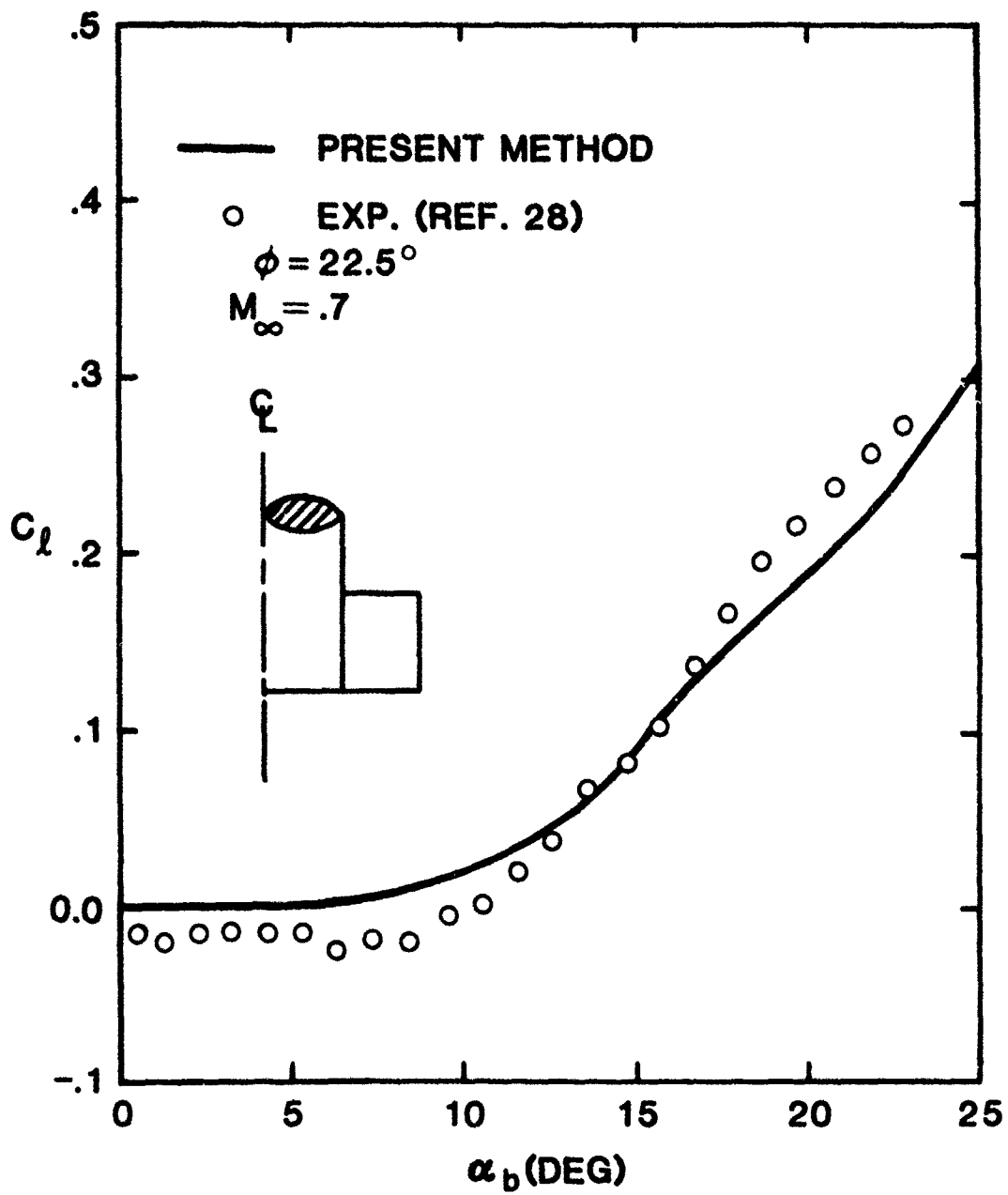


Figure 46. Induced Roll Moment vs α_b for Configuration B

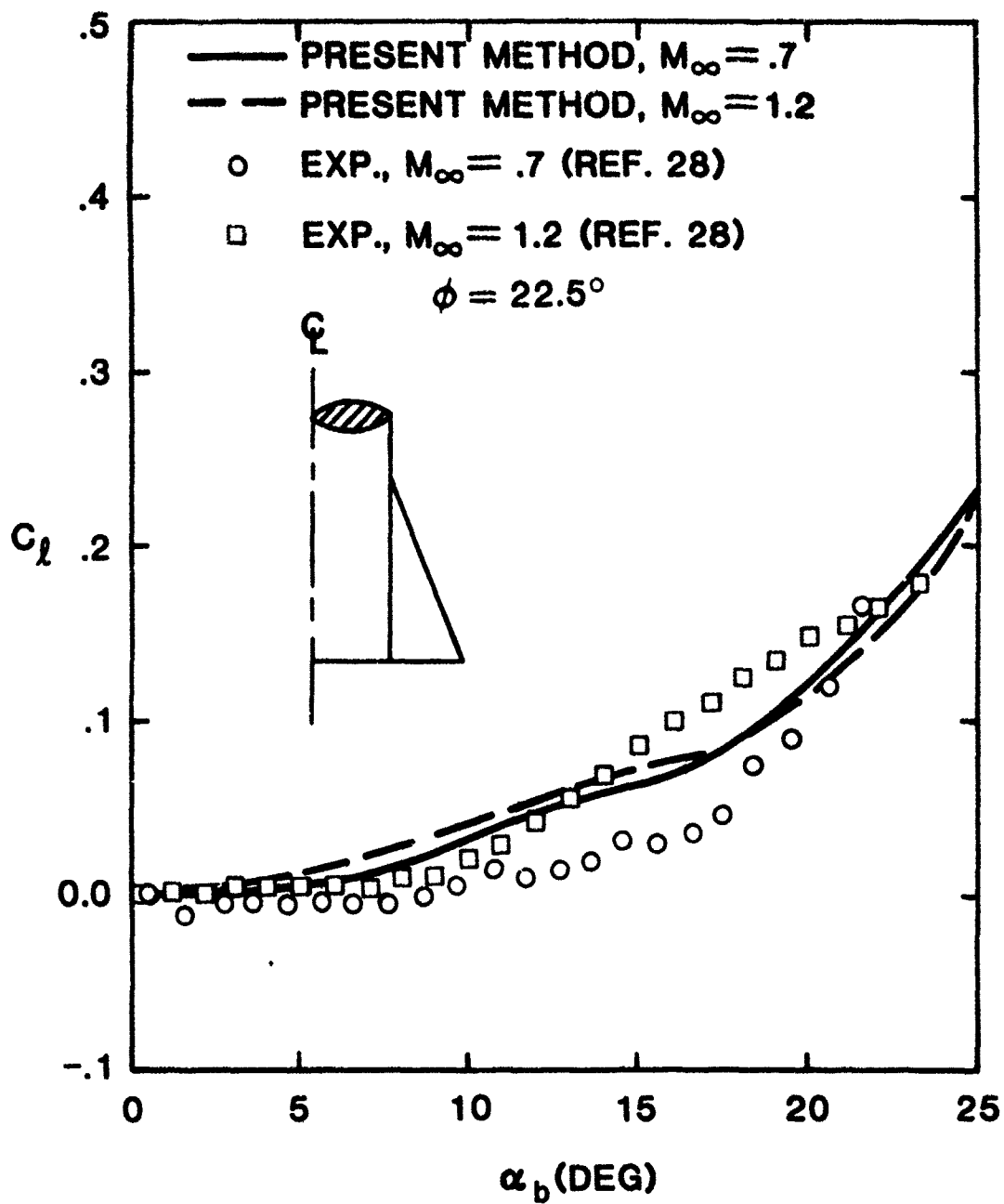


Figure 47. Induced Roll Moment vs α_b for Configuration D

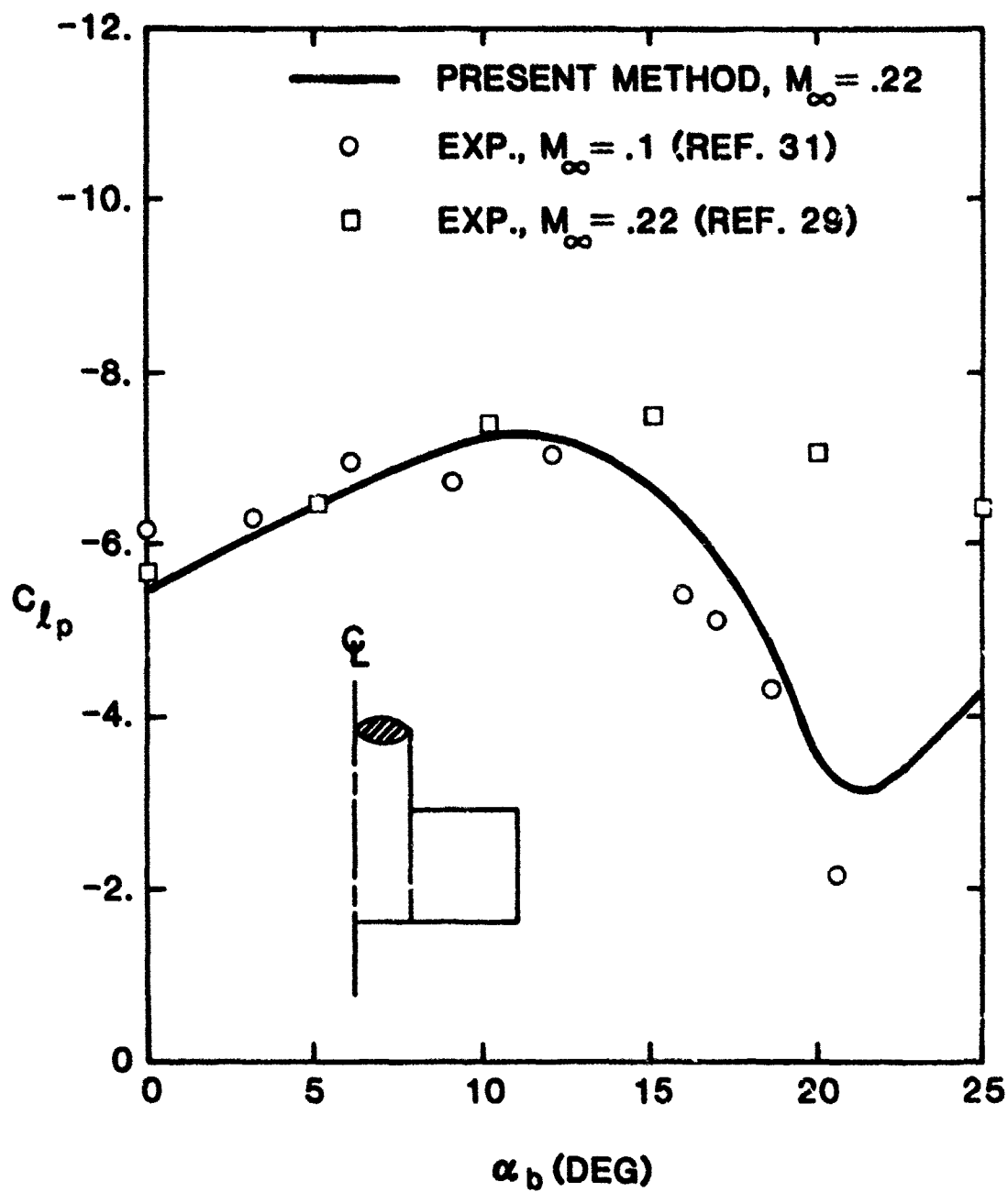


Figure 48. Roll Damping Moment vs α_b for Configuration E

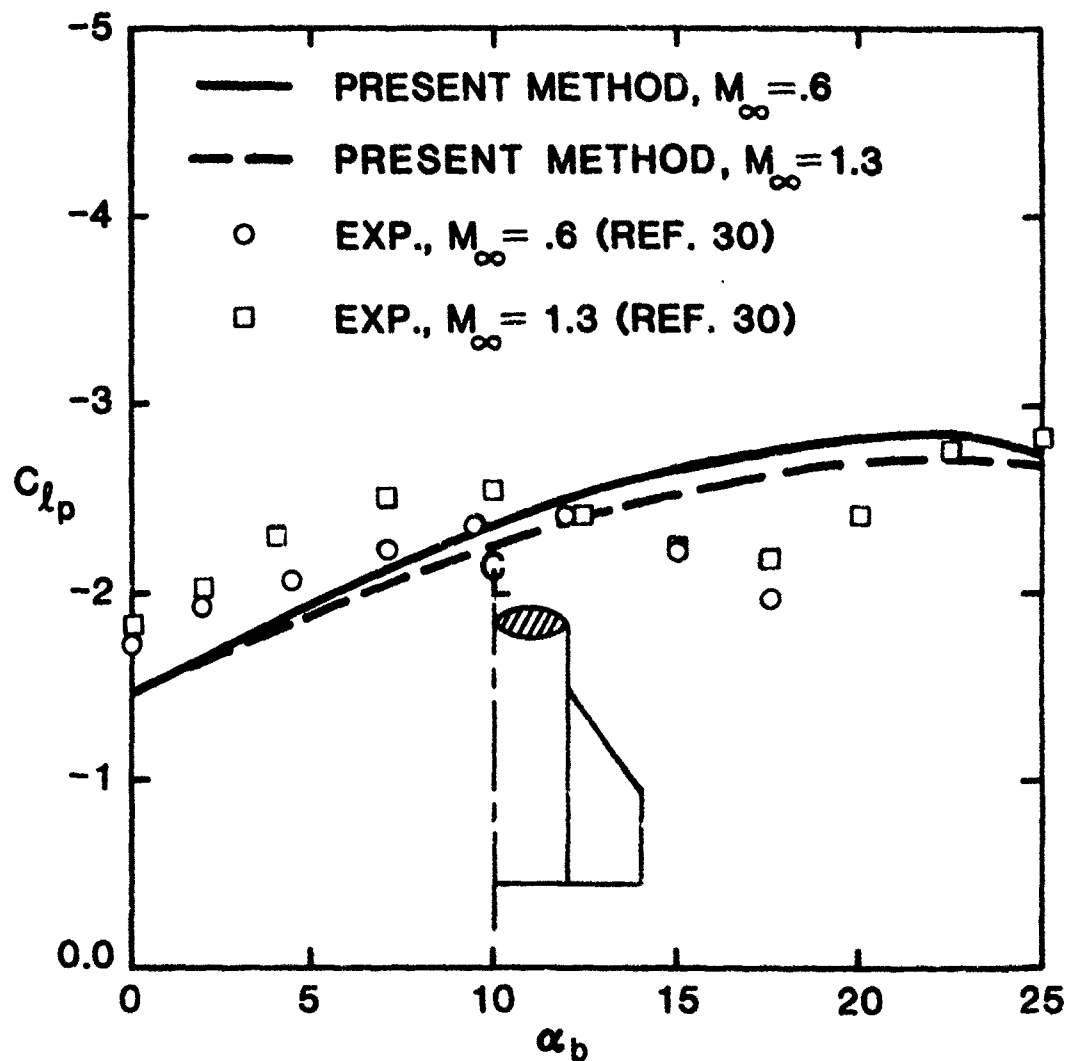


Figure 49. Roll Damping Moment vs α_b for Configuration F

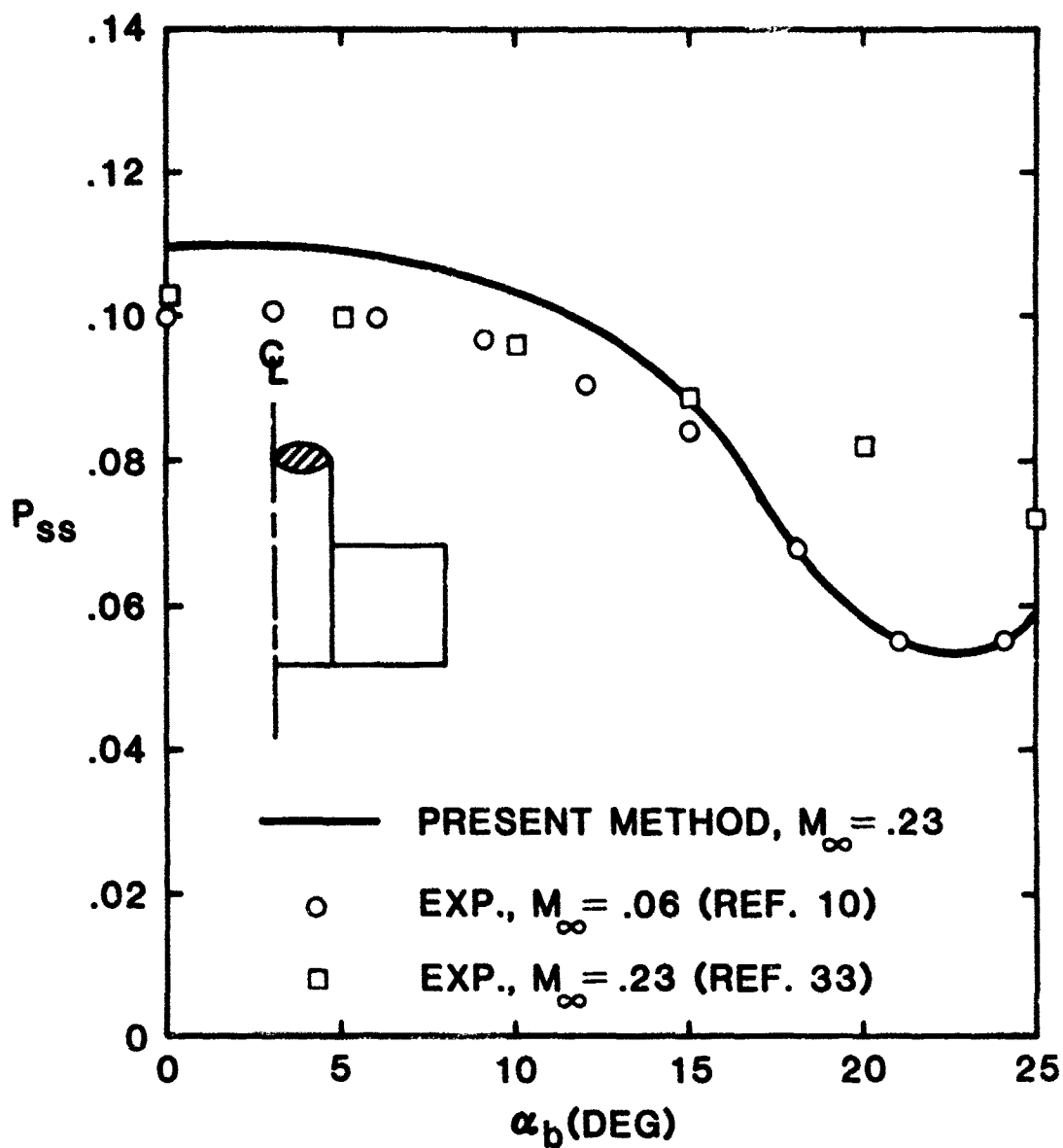


Figure 50. Steady State Roll Rate vs α_b for Configuration E (4° fin cant)

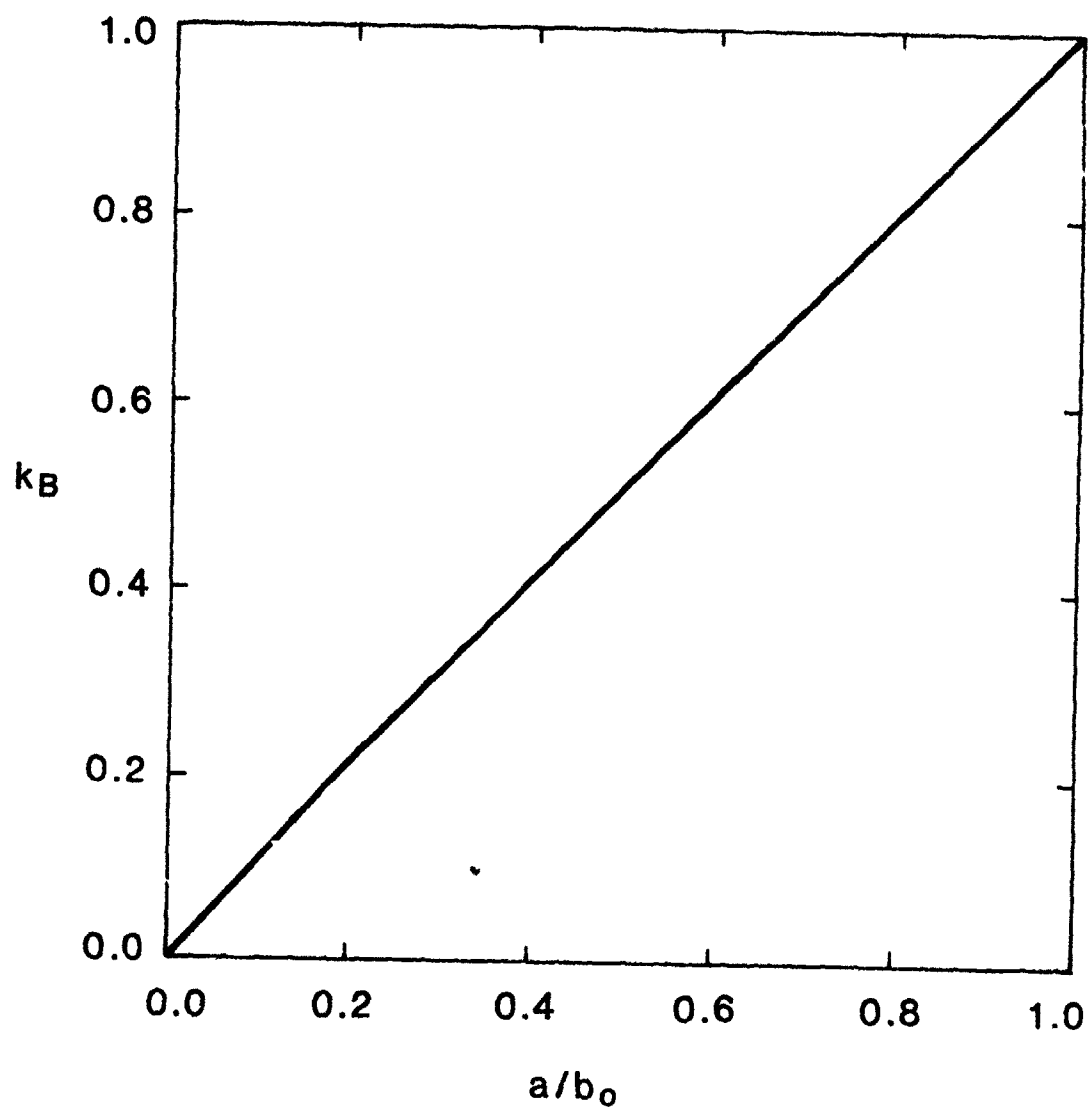


Figure 51. Interference Lift Ratio vs a/b_0 (from Ref. 24)

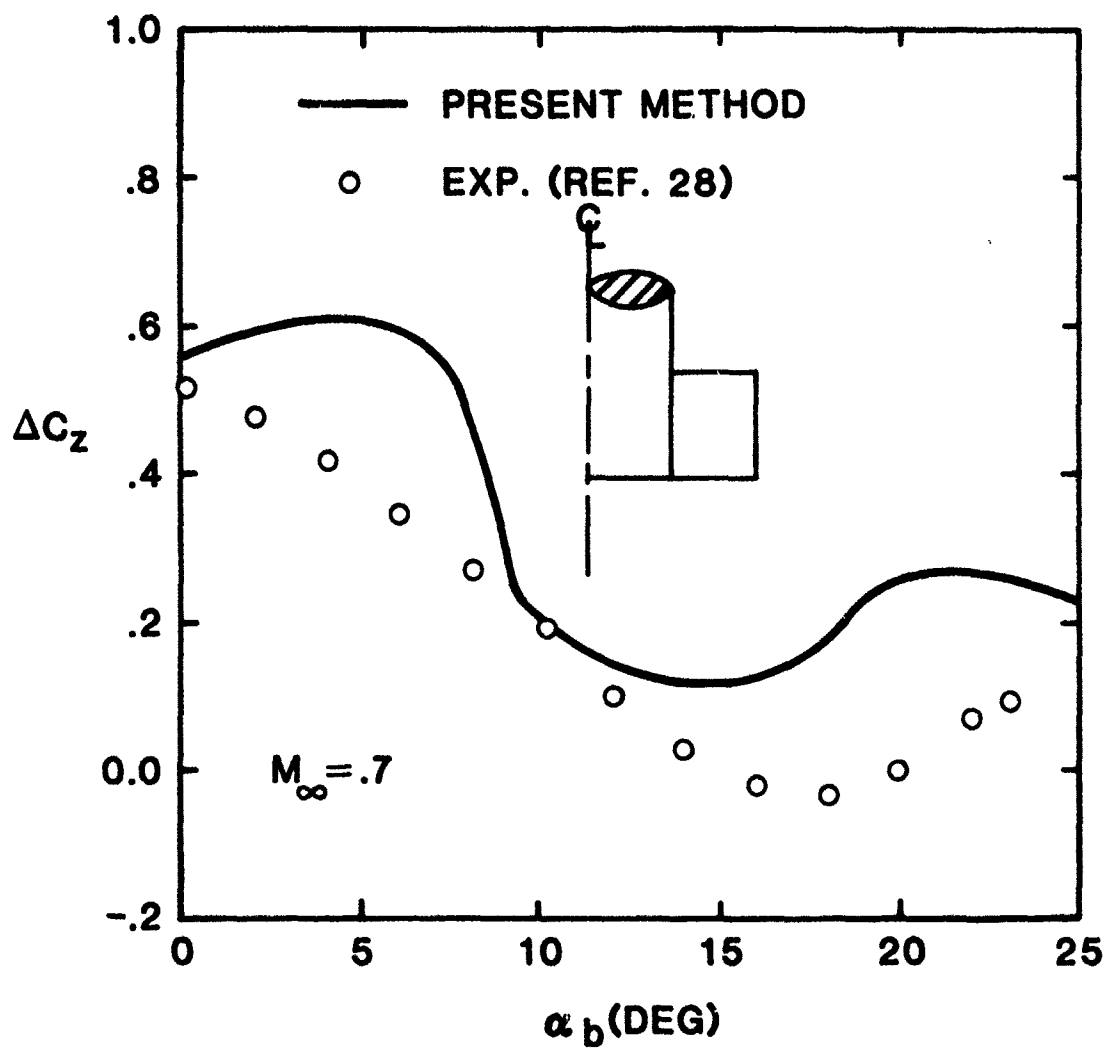


Figure 52. Pitch Control Force vs α_b for Configuration B
 ($\phi = 0^\circ$, $\delta_1 = \delta_3 = 10^\circ$, $\delta_2 = \delta_4 = 0^\circ$)

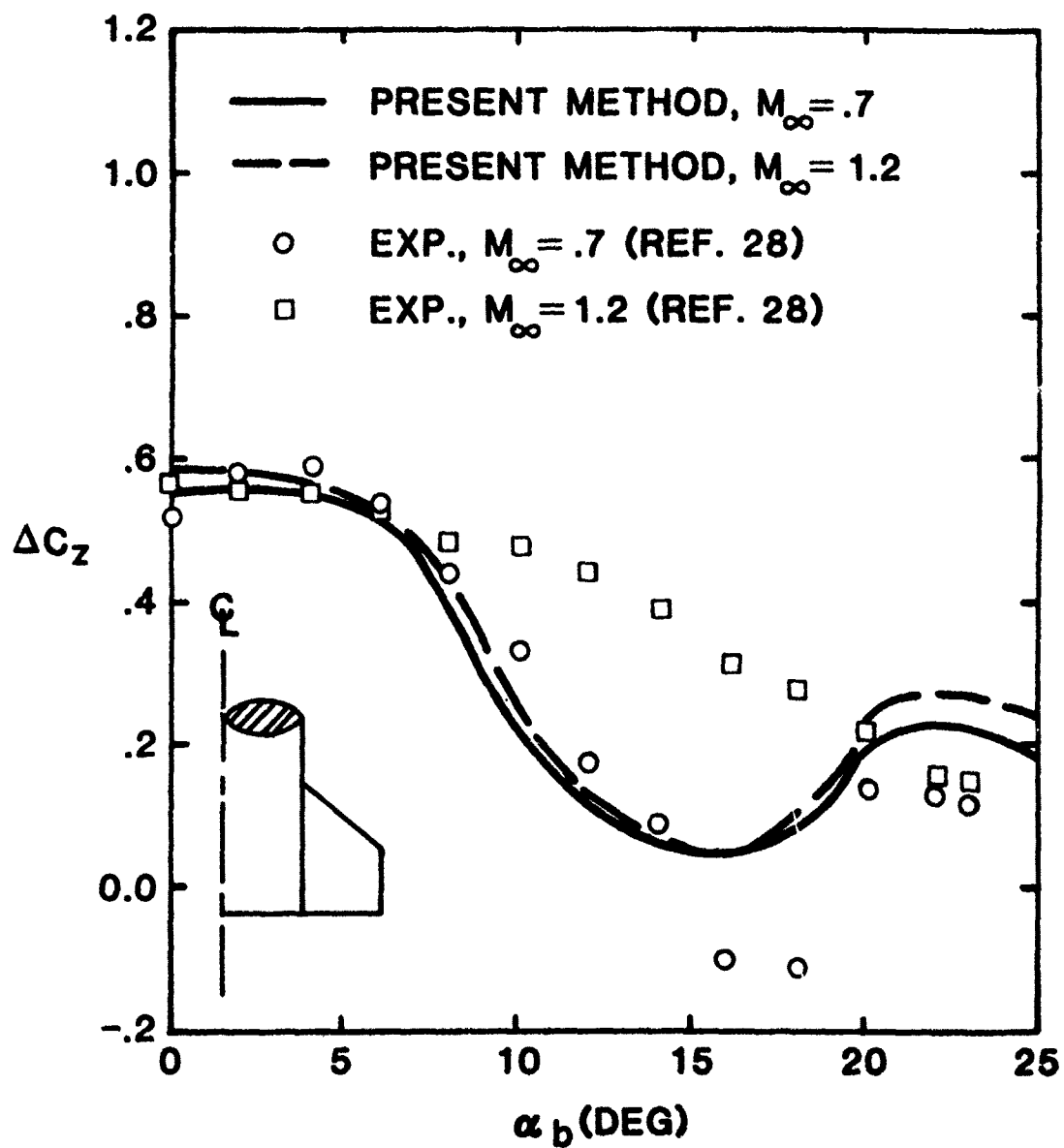


Figure 53. Pitch Control Force vs α_b for Configuration C
 ($\phi = 0^\circ$, $\delta_1 = \delta_3 = 10^\circ$, $\delta_2 = \delta_4 = 0^\circ$)

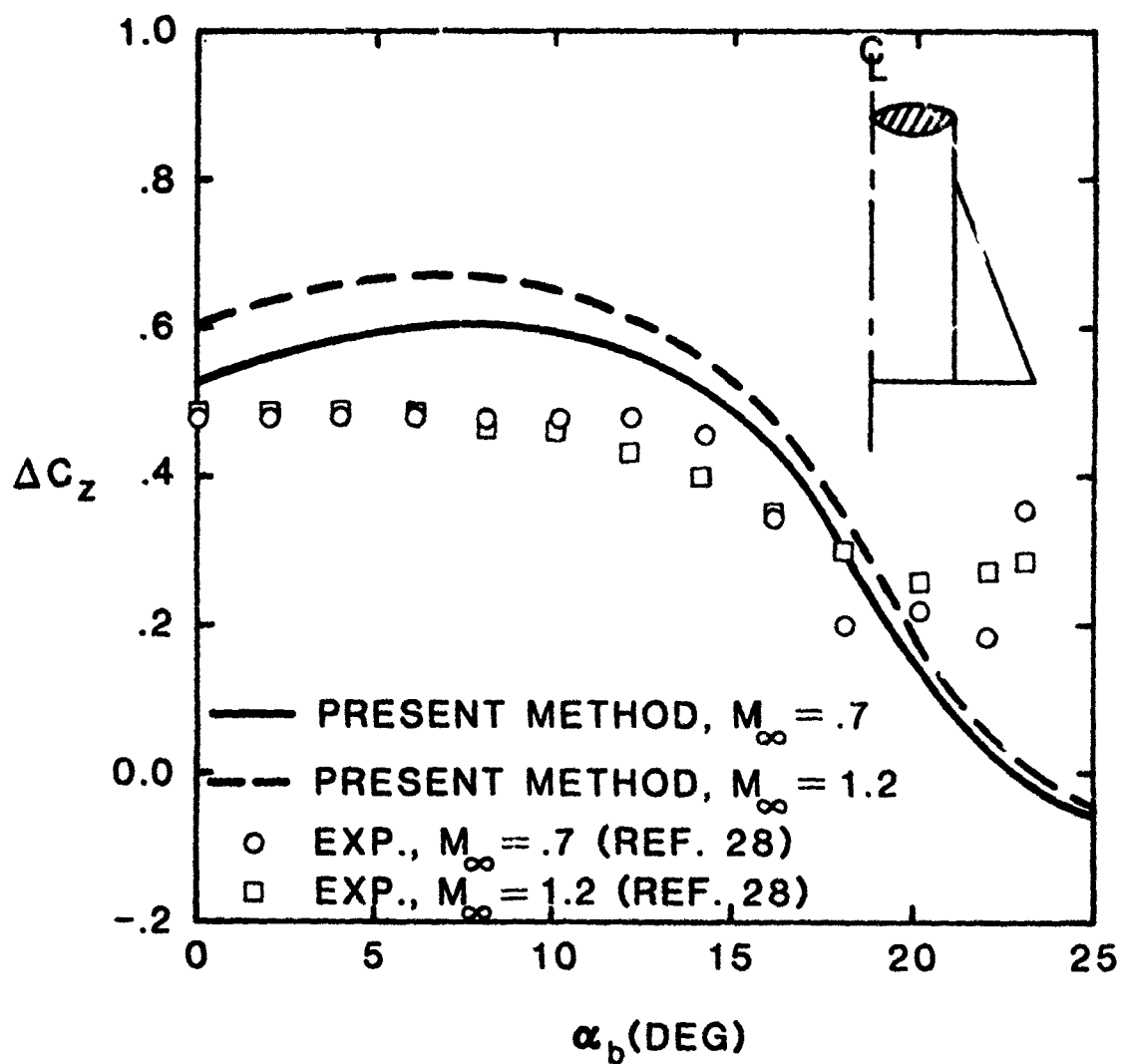


Figure 54. Pitch Control Force vs α_b for Configuration D
 ($\phi = 0^\circ$, $\delta_1 = \delta_3 = 10^\circ$, $\delta_2 = \delta_4 = 0^\circ$)

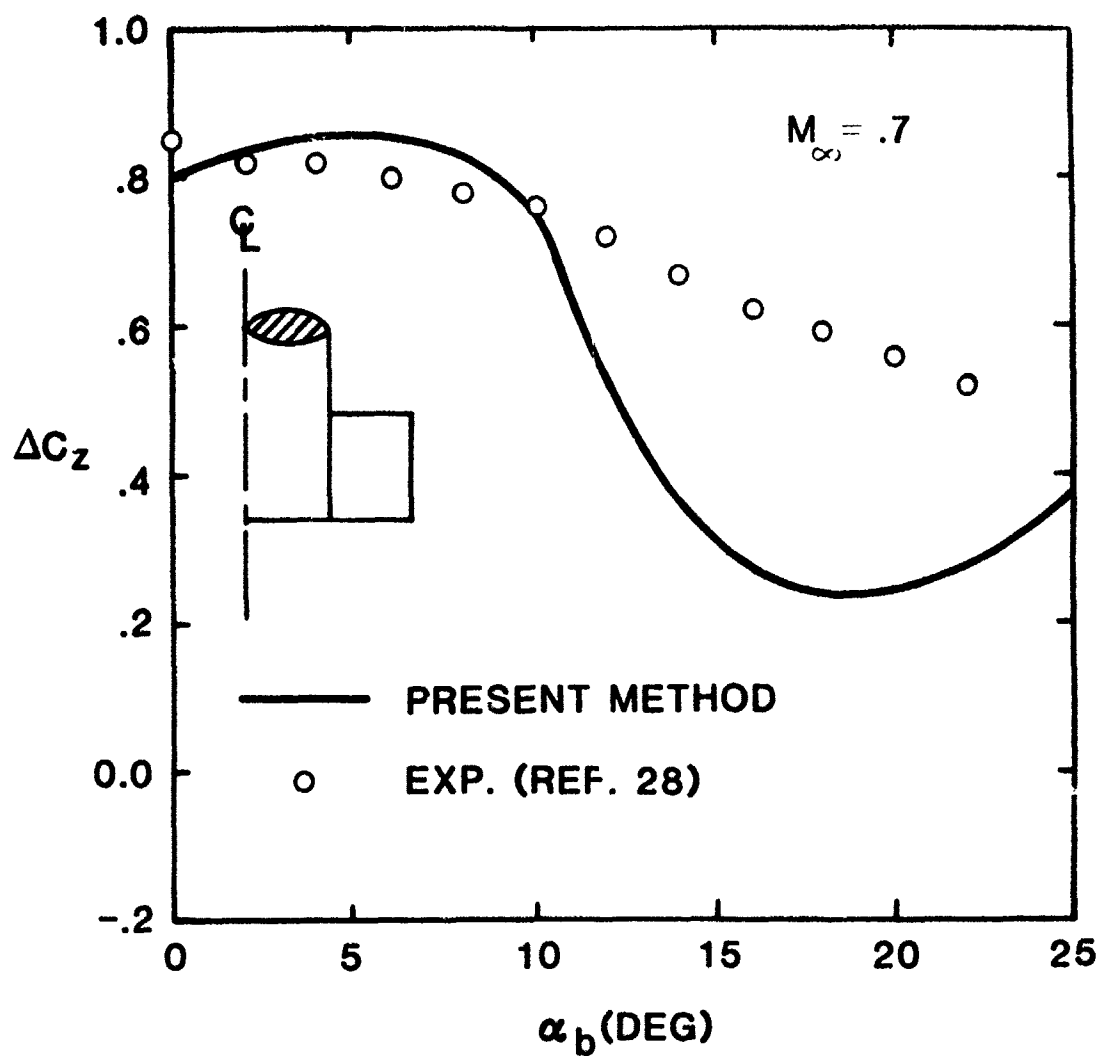


Figure 55. Pitch Control Force vs α_b for Configuration B
 ($\phi = 45^\circ$, $\delta_1 = \delta_2 = \delta_3 = \delta_4 = 10^\circ$)

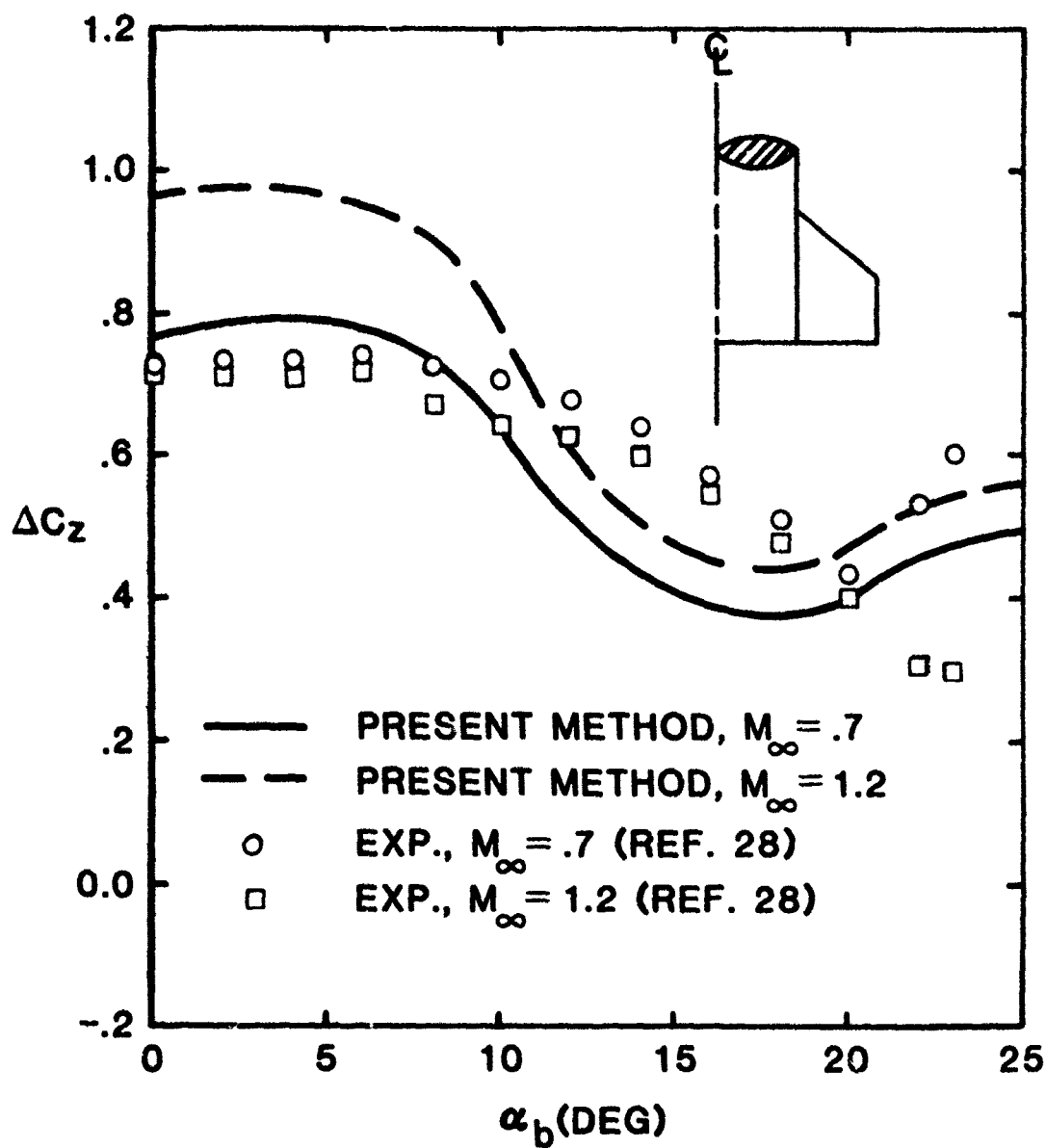


Figure 56. Pitch Control Force vs α_b for Configuration C ($\phi = 45^\circ$, $\delta_1 = \delta_2 = \delta_3 = \delta_4 = 10^\circ$)

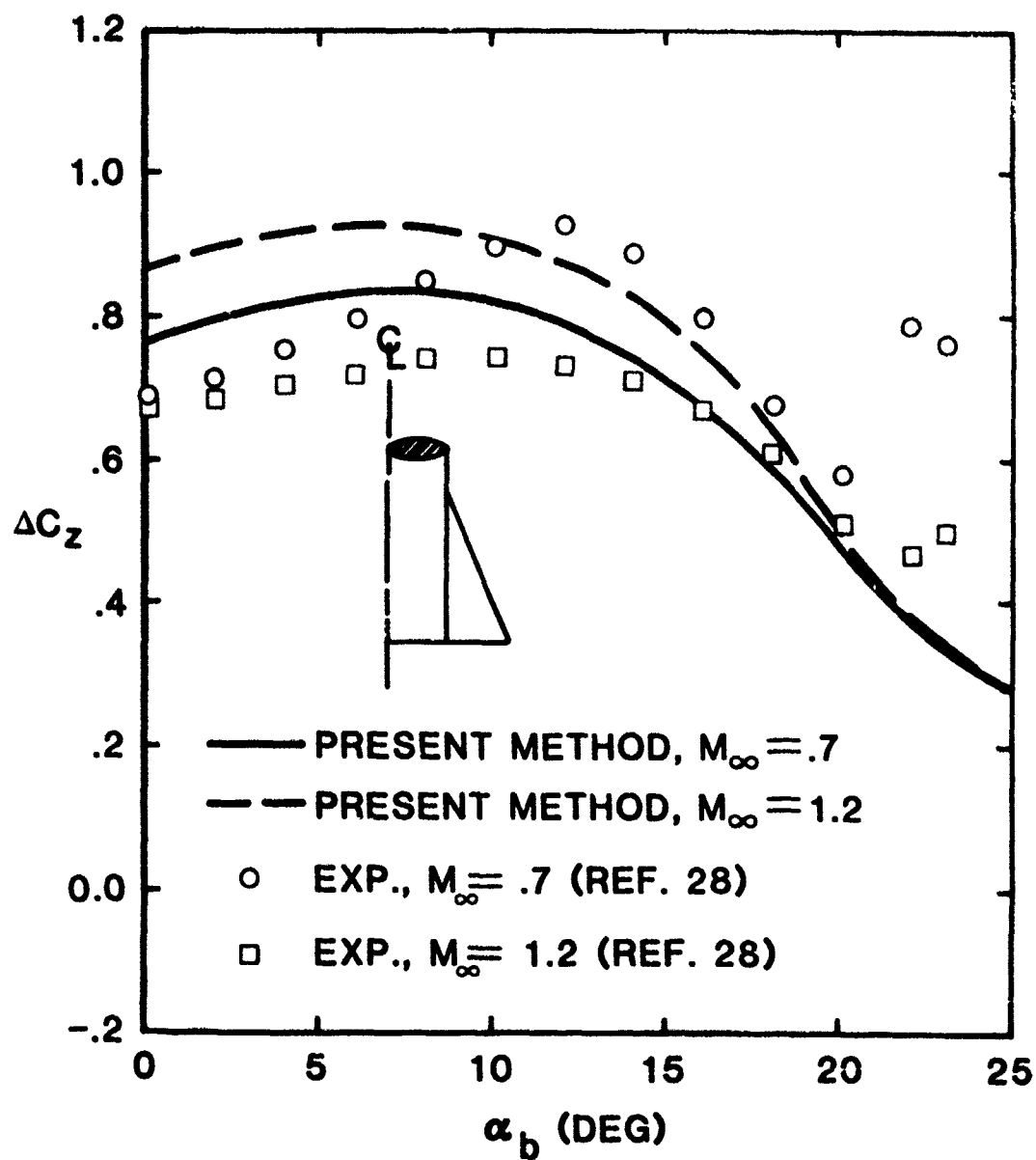


Figure 57. Pitch Control Force vs α_b for Configuration D ($\phi = 45^\circ$, $\delta_1 = \delta_2 = \delta_3 = \delta_4 = 10^\circ$)

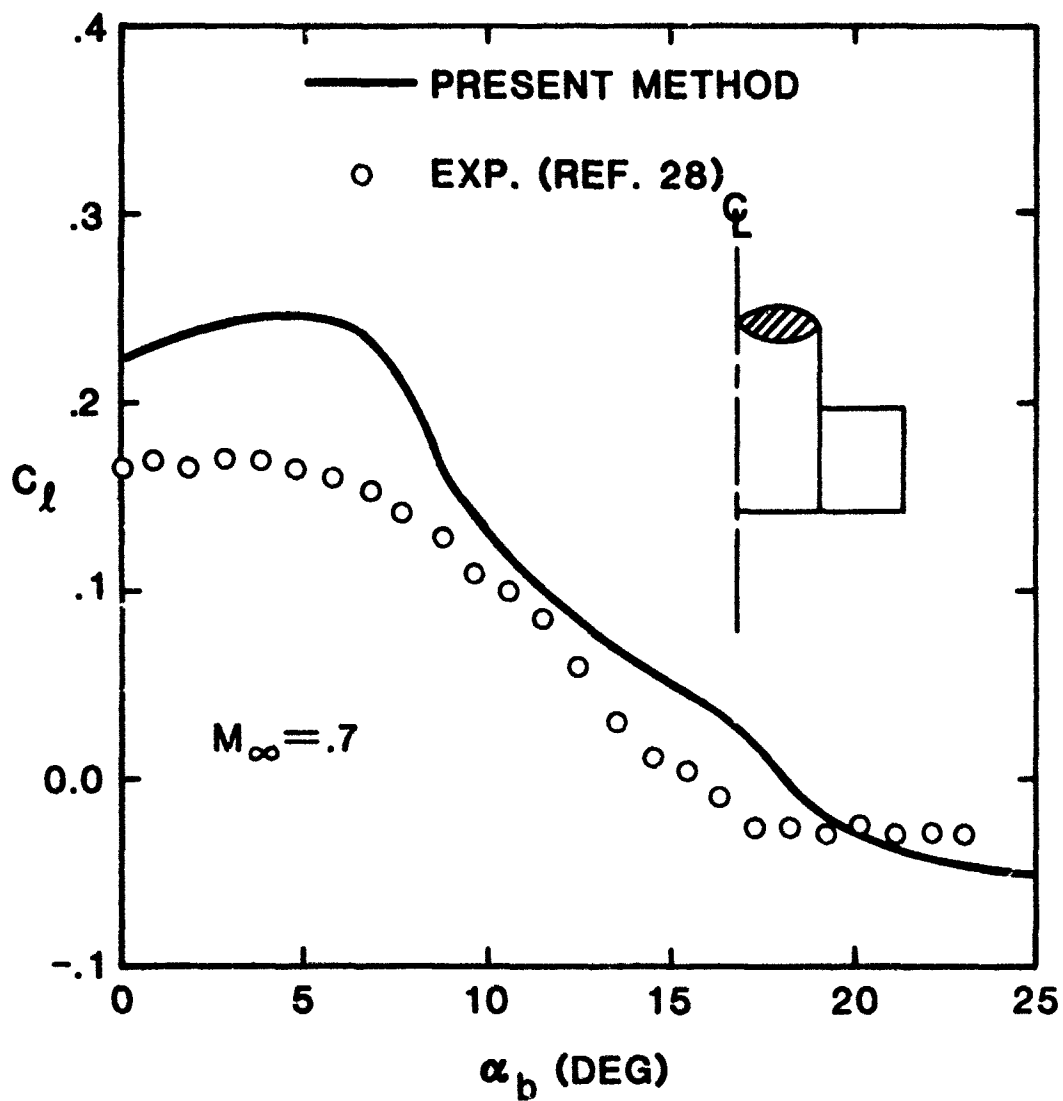


Figure 58. Roll Control Moment vs α_b for Configuration B
 ($\phi = 0^\circ$, $\delta_1 = -\delta_3 = 10^\circ$, $\delta_2 = \delta_4 = 0^\circ$)

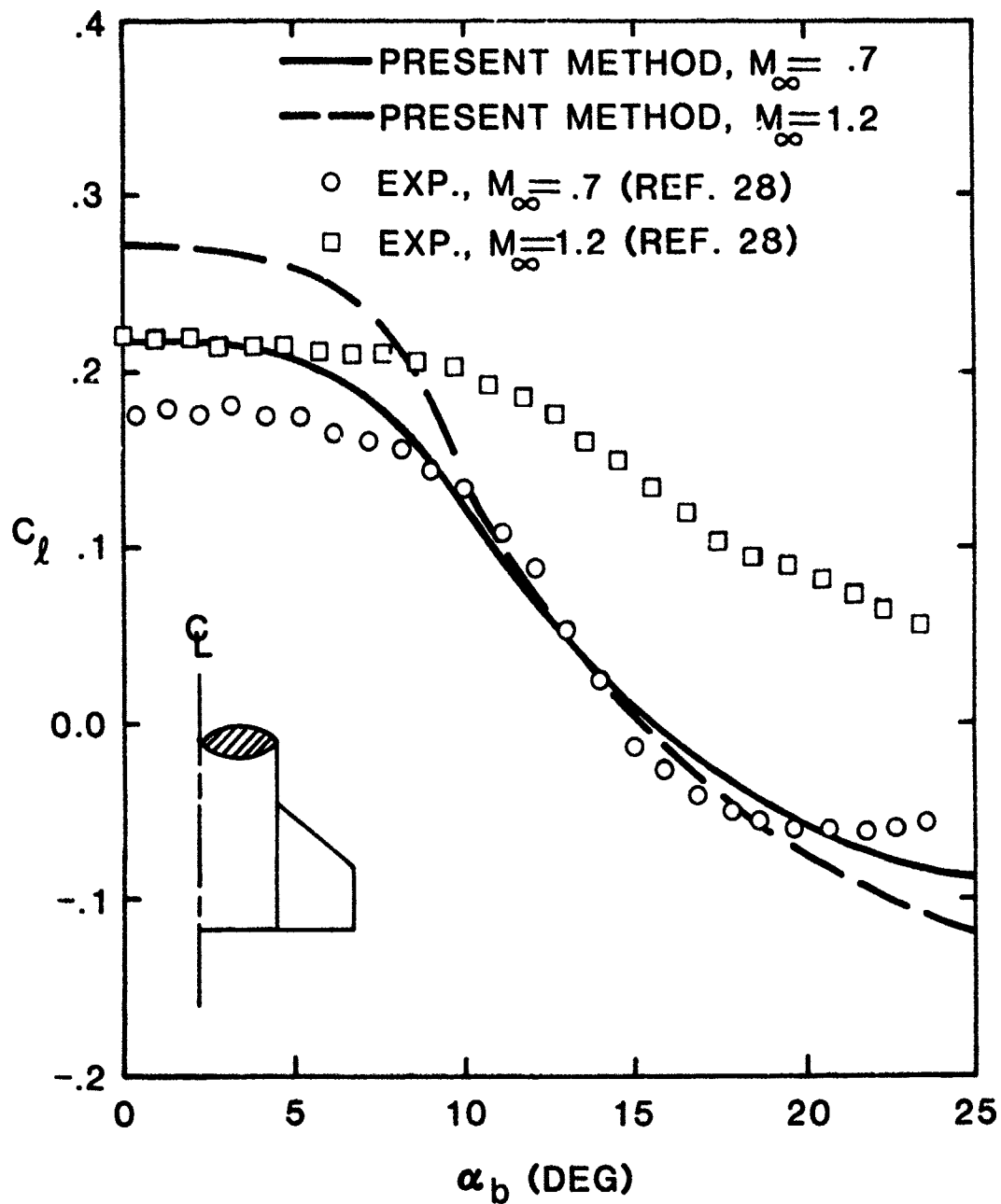


Figure 59. Roll Control Moment vs α_b for Configuration C
 ($\phi = 0^\circ$, $\delta_1 = -\delta_3 = 10^\circ$, $\delta_2 = \delta_4 = 0^\circ$)

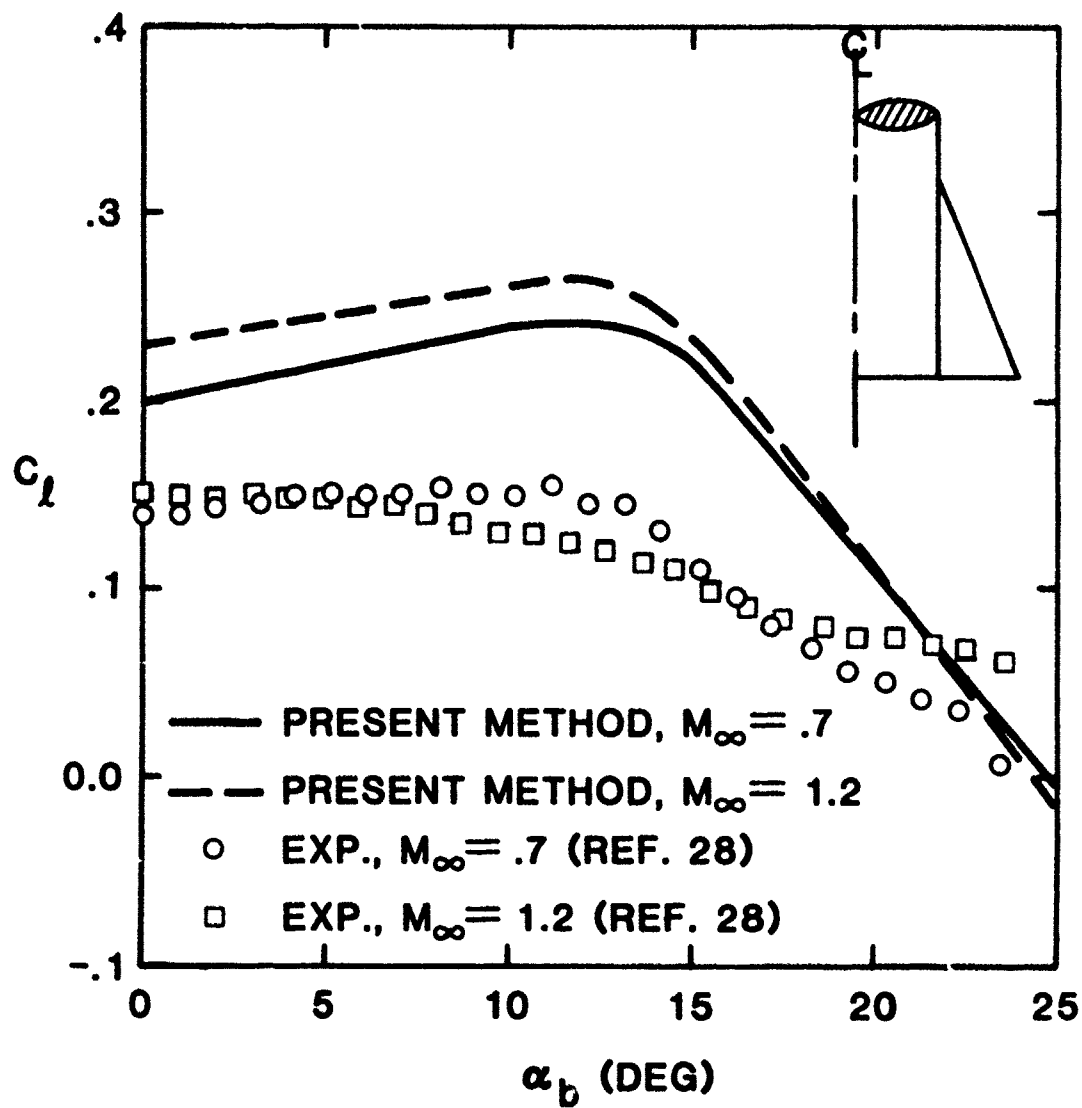


Figure 60. Roll Control Moment vs α_b for Configuration D
 $(\phi = 0^\circ, \delta_1 = -\delta_3 = 10^\circ, \delta_2 = \delta_4 = 0^\circ)$

INITIAL DISTRIBUTION

HQ USAF/SAMI	1	LOCKHEED MSL AND SPACE/DR LARS	1
AFIS/INOT	1	ERICSSON	1
HQ AFSC/DLW	1	NASA LANGLEY RES CTR/DR SAWYER	1
ASD/ENFEA	1	SANDIA NAT LAB/DR OBERKAMPF	13
AFWL/NTSA	2	DEFENSE & SPACE SYS R1/1022	
AUL/LSE 71-249	2	TRW, INC/DR SHIVANANDA	1
DTIC-DDA-2	2	UNIV OF OKLAHOMA, SCHOOL OF	
HQ USAFE/DOQ	1	AEROSPACE, MECH AND NUCLEAR	
HQ PACAF/OA	1	ENGR/DR JISCHKE	1
HQ PACAF/DOOQ	2	NORTHROP CORP/DR HUNT	1
COMIPAC/PT-2	1	UNIV OF NOTRE DAME/DR NELSON	1
REDSTONE SCI INFO CTR	2		
NAV RESEARCH LAB CODE 2627	1		
NAV SYS CMD AIR VEHICLE DIV	1		
NAV SYS CMD TECH LIB	1		
NAV SURFACE WPN CTR CODE X211	1		
NAV AIR TEST CTR	1		
USNC CODE 3431	1		
SANDIA NATIONAL LAB	1		
RAND CORP	1		
BATTELLE COLUMBUS LAB	1		
AD/SES	2		
AFATL/DLODL	2		
NAV WPNS EVAL FAC CODE 80	1		
USNWC CODE 3163	1		
AFATL/DLY	1		
ASD/ENESS	1		
AD/SD8E	1		
AFATL/DLB	1		
AFATL/DLJC	1		
AFATL/DLMA	1		
AD/XRC	1		
AD/YME	1		
AFATL/DL DL	1		
AFATL/DL	1		
HQ TAC/DRA	1		
HQ TAC/INAT	1		
ASD/XRP	1		
OO-ALC/MMWMC	1		
USA TRADOC ATAA-SL	1		
AFATL/DLODR	1		
NEAR INC/DR J.N. NIELSEN	2		
NAV SURF WPNS CTR/DR YANTA	1		
LOCKHEED MSL & SPACE COMPANY			
J.P. REDDING	1		
NAV SURF WPNS CTR/DR WARDLAW	1		
UNIV OF TENN/PROF WU	1		
NAV SURF WPNS CTR/DR MORRISON	1		
NASA AMES RES CTR/MR KEENER	1		